POLITECNICO DI TORINO

Department of Mechanical and Aerospace Engineering (DIMEAS)

Master's Degree Thesis
in Biomedical Engineering

Composite scaffolds with porosity over multiple length scale for skin regeneration

Supervisors

Gianni Ciofani

Elisa Mele

Giada Graziana Genchi

Candidate

Viola Sgarminato

April 2018

Ai miei genitori

"Occorre volerlo.
Amando il cammino quanto la meta"

Paolo Cortese (Il prof. di Analisi Matematica 1)

Table of Contents

Abstract

This thesis project involves the production of composite scaffolds with porosity over multiple length scales for skin regeneration. The aim of the project is to develop wound dressings for the treatment of chronic wounds, such as pressure ulcers, diabetic foot ulcers and vascular ulcers. Chronic wounds represent a large problem in the world and affect 37 million patients globally. The function of the scaffolds developed during the project is to promote the wound healing process by electrically stimulating skin cells. To this aim hierarchical scaffolds of polycaprolactone (PCL) and piezoelectric barium titanate ($BaTiO_3$) nanoparticles were fabricated using 3D-bioprinting and the electrospinning technique. The manufacturing and the surface characterization of the nanocomposite scaffolds were performed at the Materials Engineering Department of Loughborough University (UK). Then, the biological characterization and the evaluation of piezoelectric response were implemented at the Italian Institute of Technology (IIT) in Pontedera (Italy).

The first chapter of this thesis focuses on the skin, by describing its structure and function and by reporting the main types of wounds with particular attention for the physiological wound healing process. The electrical response of the skin was also delineated by reporting literature examples that demonstrate the beneficial effects of electric fields in the wound healing process.

The second chapter consists of an overview of the main tissue engineering strategies used for promoting wound healing, by focusing on commercial available, traditional, modern and advanced dressings. The fundamental characteristics that a dressing should have were also illustrated.

The introduction concludes with the third chapter that describes the two methods used in this work: electrospinning and 3D-bioplotting. The instruments and working principles of these techniques were explained and their main applications in wound healing were described.

The experimental section includes the explanation of the methods used for fabricating the nanofibers in polycaprolactone (PCL) and poly(lactic acid) (PLA). In this chapter the preparation of polymeric solutions and the electrospinning process were illustrated. The various tests that were performed to optimize the fabricating conditions were also reported.

The fifth chapter focuses on the fabrication of piezoelectric and non-piezoelectric PCL scaffolds by describing the process and the equipment used in 3D-bioplotting technique. This section concludes with the explanation of method that was developed to produce the hierarchical composite scaffolds.

The last chapter of the experimental part involves the characterization of nanofibrous mats and 3D-printed scaffolds. The surface characterization of substrates was performed by using optical microscopy, scanning electron microscopy (SEM) and scanning and transmission electron microscopy (STEM). In this chapter the *in vitro* study performed to evaluate the cell proliferative capability and the cellular response to the piezoelectric substrates are also described. Assays to analyse the cellular proliferation and the cytocompatibility of substrates were performed and fluorescence microscopy was used. The confocal microscopy was also employed to obtain three-dimensional images of the dressings and calcium imaging data.

In the "Results" section the data obtained for the fabrication and characterization of nanofibrous mats, piezoelectric and non-piezoelectric scaffolds, and composites are analysed. The cytocompatibility of developed substrates is demonstrated by the evaluation of the fluorescence images and the comparison among values of absorbance measured through the WST-1 and alamarBlue assays.

The thesis concludes with a discussion on the performed study and an evaluation about the future perspectives.

Introduction

1 The Skin

The human body is covered by a flexible and resistant layer of skin which represents a protective barrier from the surrounding environment and plays a vital role against the entry of xenobiotics into the organism. Furthermore, it maintains homeostasis by regulating the transport of water and small metabolites out of the body. The thickness of the skin ranges from 0.5 to 2 mm in the eyelids and joint flexures, and it reaches 4 mm in callus areas (palms and soles) (Wood & Bladon, 1985; Anastasi, et al., 2006). Human skin is the largest organ of the tegumentary apparatus and constitutes approximately one-eighth of the weight of a standard individual (Table 1.1).

Table 1.1 - *Weight of the various tissues of a 65 kg human male (Wood & Bladon, 1985).*

Tissue	kg weight
Skeletal Muscle	30.0
Internal organs	7.3
Bone	9.0
Skin and subcutaneous tissue	7.8
Adipose tissue	4.0
Blood	5.5
Connective tissue	1.0
Tissue fluids	0.4

1.1 Skin Structure

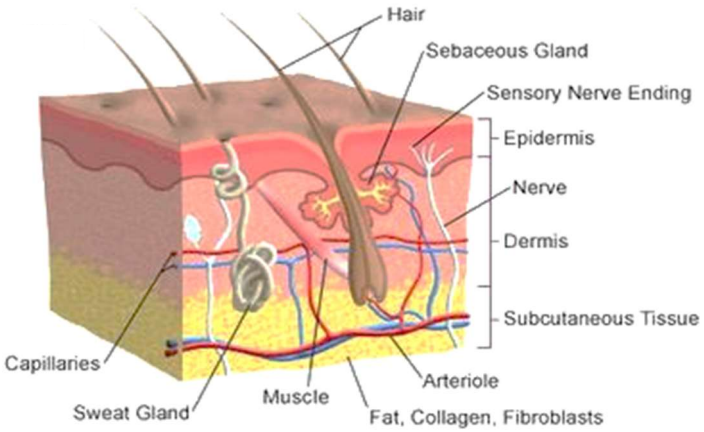

Figure 1.1 – *Skin Structure: Epidermis, Dermis and Hypodermis (Dawson & N., 2014).*

The skin has a highly complex, hierarchical, and stratified structure. As shown schematically in Figure 1.1, it is divided into three layers: the epidermis, dermis and subcutaneous tissue (hypodermis).

The *epidermis* is the most superficial layer of the skin and it is essential to provide a protective barrier against bacteria and harmful toxins, to control thermoregulation and to produce vitamin D (Proksch, et al., 2008). It is a highly cellular and avascular tissue with a thickness of 0.01-0.06 mm in most areas but tending to increase on the back and on callus area (Wood & Bladon, 1985). Epidermis derives from the embryonic ectoderm and produces cutaneous appendages like the sweat and sebaceous glands, which are responsible for producing sweat and the lubricant substance sebum, respectively. This layer also forms nails and follicles that develop the hair matrix. Epidermis is composed by keratinocytes (responsible to produce keratin), melanocytes (important for pigmentation of the skin), Langerhans cells and Merkel cell. Keratinocytes are the most numerous cells of epidermis. During their life cycle, they give rise to several states that constitute five epidermal layers: *stratum basale* (basal layer), *stratum spinosum* (spinous layer), *stratum granulosum* (granular layer), *stratum lucidum* and *stratum corneum* (horny layer of dead cells) (Anastasi, et al., 2006; McGrath, et al., 2004) (Figure 1.2).

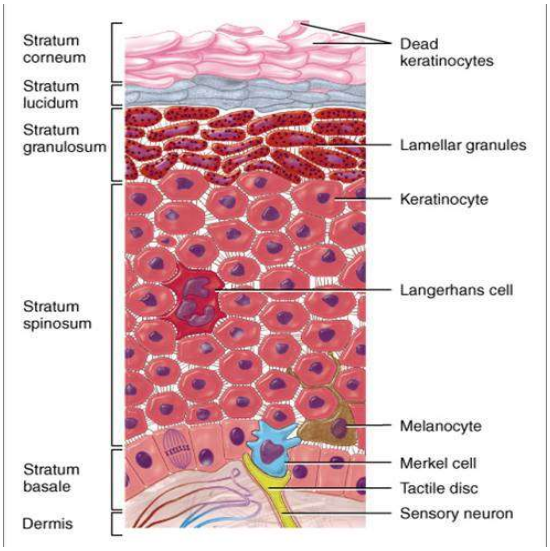

Figure 1.2 *– Epidermis layers. They correspond to the same cells (keratinocytes) at different times of their life cycle (Volker, 2017).*

Dermis is the largest layer forming the bulk of the skin; it arises from embryonic mesoderm and its thickness is in the range of 2-4 mm (Wood & Bladon, 1985). This layer is constituted by a dense, richly vascularized and innervated connective tissue. It provides stress and strain resistance, elasticity and tensile strength through an extracellular matrix (ECM) composed of glycosaminoglycans (GAGs), elastin and collagen (Breitkreutz, et al., 2009). In contrast to the epidermis the dermis contains few cells, mainly mast cells, macrophages, lymphocytes and fibroblasts. These are important for the synthesis of ECM enzymes and proteins and they also activate the wound healing cascade by protease and collagenases (Boughton & Mclennan, 2013).

Hypodermis is the innermost layer and it is composed of loose connective tissue. Its thickness ranges between 0.5 and 2 cm: lower thickness where the skin is in direct contact with bone or cartilage (such as the cranial vault, nose, earpiece) and larger one in other areas (buttocks, palm of hands or feet plant) (Anastasi, et al., 2006). The adipose tissue of this layer provides thermoregulation and mechanical protection and represents an energy reserve.

1.2 Skin Wounds

A wound represents a destruction or a damage to the physiological structure and function of tissues. It can be limited to the epidermis resulting in a disruption of skin's integrity or it can reach the subcutaneous tissue, harming other structures like muscles, tendons, vessels, nerves, parenchymal organs and bone (Velnar, et al., 2009). A simple wound does not involve significant tissue loss and other associated complications; while a complex wound implicates tissue devitalization, infection, ischaemia (flap necrosis), haematoma or compartment syndrome (Kumar & Leaper, 2007). The direct consequence of a wound is a violation of the natural defence barrier and the invasion of micro-organisms that cause infections. There are many factors that determine the presence of wounds; they can have an accidental or intentional aetiology or can be the consequence of a disease process (Singh, et al., 2017). There are many criteria to classify wounds including time. Indeed, time is an important variable in wound repair because of the dynamicity of wound healing process (Robson & Steed, 2001). In particular, wounds can be categorized as acute and chronic on the basis of the healing time frame. An acute wound heals within a predictable time period and becomes chronic wounds followed by a lack of healing within 6 weeks.

1.2.1 Acute Wounds

Acute wounds are usually caused by a trauma or inflammation and usually heal within 6 weeks. They can be classified with reference to their aethiology, morphology, contamination and complexity (Table 1.2).

***Table 1.2** – Wound classification systems for acute wounds (Kumar & Leaper, 2007).*

Aetiological	Morphological	Contamination	Complexity
Surgical	Abrasion	Clean	Simple
Penetrating trauma	Incision	Implant	Complex
Stab	Superficial	Non-implant	Open fracture
Projectile injury	Deep	Clean-contaminated	Laparostomy
Bite/envenomation	Degloving injury	Contaminated	Complicated
Blunt trauma	Ulceration	Dirty-infected	Wound infection
Avulsion/traction	Superficial		Gas gangrene
Crush injury	Laceration		Flap necrosis
Burns			
Thermal			
Electrical			
Irradiation			
Frost-bite			

More generally acute wounds are divided into surgical and accidental wounds. The level of contamination allows distinguishing surgical wounds into clean, clean-contaminated, contaminated and dirty.

Clean wounds are characterized by noninflamed and noninfected tissue without damages to a visceral organ; they have an infection risk of 1-2%. Clean-contaminated wounds show noninflamed and noninfected tissue with a controlled entry into a visceral organ; depending on the organ system the infection risk may exceed 10%.

Contaminated wounds are associated with inflamed and purulent areas and with gross spillage of enteric contents. These wounds have 60% incidence of Surgical Site Infections (SSI).

The conclusive category of surgical wounds includes dirty wounds, distinguished by devitalized or grossly infected tissue and by involved visceral organs or wounds that contain a foreign body.
These wounds have a large incidence of SSI (greater than 60%) because of the bacterial presence and the grade of contamination (Reichman & Greenberg, 2009).
Acute accidental wounds are caused by a traumatic loss of tissue and it is possible to divide them on the basis of the mechanism of injury and/or the nature of tissue trauma. The principal classes include abrasions, lacerations and incisions (Singer, et al., 1997).

1.2.2 Chronic Wounds

Chronic skin wounds represent a large problem in the world affecting 37 million patients globally and approximately 6 million in the United States (Agren, 2016). They are a relevant economic burden to society and a significant morbidity to the individual. In US alone the annual costs for associated treatments are around $25 billion and in the UK, chronic wounds represent the loss of an estimated 2 million working days per year (Parani, et al., 2016; Boughton & Mclennan, 2013) As opposed to acute wounds, chronic wounds healing is incomplete after 6 weeks and it is susceptible to infection, tissue hypoxia, necrosis, exudate, excess levels of inflammatory cytokines, a less mitogenic activity and elevated protease activity (Vanwijck, 2001). Chronic wounds are characterized by a non-healing state, due to the continuous inflammation which causes a cascade of tissue responses and an increased collagen deposition with a consequent formation of significant and fibrotic scar. Because of this inflammatory state functional and anatomical recovery is prevented and these wounds are frequently subject to relapse (Degreef, 1998). Chronic wounds are mainly due to co-existing pathologies such as diabetes mellitus, peripheral arterial disease, venous insufficiency and they are aggravated by tobacco smoking, low serum albumin, advanced age, immobility, malnutrition and other inflammatory conditions (Whelan, et al., 2014; Amir, et al., 2012).
Chronic wounds comprehend pressure ulcers, diabetic foot ulcers and vascular ulcers (including venous and arterial ulcers).

Pressure ulcers represent the most common type of chronic wounds and, according to the National Pressure Advisory Panel, they consist in a localized injury to the epidermis and/or subcutaneous tissue (Sen, 2009).

They are also known as bed sores, pressure sores and decubitus ulcers and they are caused by excess pressure or pressure in combination with shear and friction forces (Moor & Cowman, 2008). Most vulnerable patients are the elderly, stroke victims, patients with diabetes, dementia, those in wheelchairs, bedridden, or suffering from impaired mobility or sensation (Sen, 2009). These subjects usually present pressure ulcers on sacrum and heels but also in close proximity to bony prominences such as the ischium, greater trochanters, elbows, knees and posterior scalp.

The pathology can be classified into four stages (Table 1.3).

Table 1.3 *– Stages of pressure ulcers (Tew, 2014).*

Stage	Description
Stage I	Erythematous, non-blanchable intact skin, usually over bony prominences
Stage II	Shallow open ulcer with partial-thickness loss of dermis
Stage III	Full thickness issue loss and subcutaneous fat exposure
Stage IV	Full-thickness issue loss with exposed periosteum bone, tendon, or muscle

Diabetic ulcers are lesions of difficult spontaneous healing that may affect skin, subcutaneous and bone tissues, in relation to their gravity. The most common anatomical location is in the foot, involving apex regions of the fingers, the joints of fingers, the metatarsal heads (the plantar region), the heel, the ankle and the leg. Diabetic foot ulcers are caused by the glycosylation of haemoglobin and erythrocyte membranes: the first provokes a decreased oxygenation in tissues while the second results in an increased blood viscosity, decreased erythrocyte deformation and in a reduction of flow.

Diabetic patients also develop peripheral neuropathies that cause paraesthesia at the distal extremities of the lower limbs (Agren, 2016). It is estimated that up to 25% of all diabetics will develop a diabetic foot ulcer (Lippert-Gruner, 2003).

This pathology often evolves into an infection that can lead to the development of septic necrosis and to the consequent amputation.

Vascular ulcers generally can be classified as arterial or venous ulcers. Location, appearance, bleeding and associated pain of vascular ulcers are different and permit to distinguish arterial or venous ulcers. Arterial (or ischemic) ulceration arises from either progressive atherosclerosis or arterial embolization, that cause ischemia of the skin and loss of tissue (Figure 1.3).

***Figure1.3** – Vascular Ulcers. Arterial ulcer with typical features (Gabriel, 2016).*

Venous (or stasis) ulceration is caused by a venous hypertension. Studies demonstrate that the pathology can be due by an increased stasis which lead to the develop of a fibrinous pericapillary cuff impeding the delivery of oxygen and other nutrients or growth factors to the affected tissue. The loss of oxygen implies a maturing of necrosis and ulceration. Another hypothesis asserts that the increase of pressure in veins and the activation of leukocytes damage the endothelium leading to injury and ulceration (Gabriel, 2016).

1.3 The Physiological Wound Healing Process

The process of normal wound repair is a dynamic and complex mechanism by which the integrity of dermal and epidermal is restored after an injury occurs. More precisely, a physical disruption of the skin layers triggers a cascade of cellular and extracellular pathways resulting in the activation of a series of interrelated and overlapping events (Boughton & Mclennan, 2013; Qing, 2017).

This response leads to the wound healing and can be divided into four distinct phases: haemostasis and inflammation, proliferation, maturation and remodelling, and wound contraction (Tejiram, et al., 2016).

1.3.1 Haemostasis and Inflammation

The rupture of vessels due to the injury is immediately followed by the response of body to prevent bleeding and promote haemostasis. Cytoplasmic calcium levels increase and cause the contraction of smooth muscle in damaged vessels that leads to a decrease of blood flow. Exsanguination is also prevented through the activation of the coagulation cascade and the formation of a clot. This process occurs through three key mechanisms: intrinsic pathway of the clotting cascade, extrinsic pathway of the clotting cascade and platelet activation (Singh, et al., 2017). The first mechanism is responsible of the activation of factor X, which converts prothrombin to thrombin and consequently fibrinogen to fibrin resulting in the formation of a fibrin plug. Extrinsic pathway causes the activation of factor VII and thrombin while the third mechanism is responsible of formation of a platelet plug. The activation of thrombin, thromboxane and adenosine diphosphate (ADP) causes a change in the morphology of the platelets and the following secretion of cytokines and growth factors from their α-granules (Tejiram, et al., 2016; Zarbock, et al., 2007). Platelets adhere to the subendothelial collagen which is exposed because of the injury and they form a plug, temporarily arresting bleeding. The formed clot provides a scaffold for migrating cells like neutrophils, monocytes fibroblasts and endothelial cells (Figure 1.4).

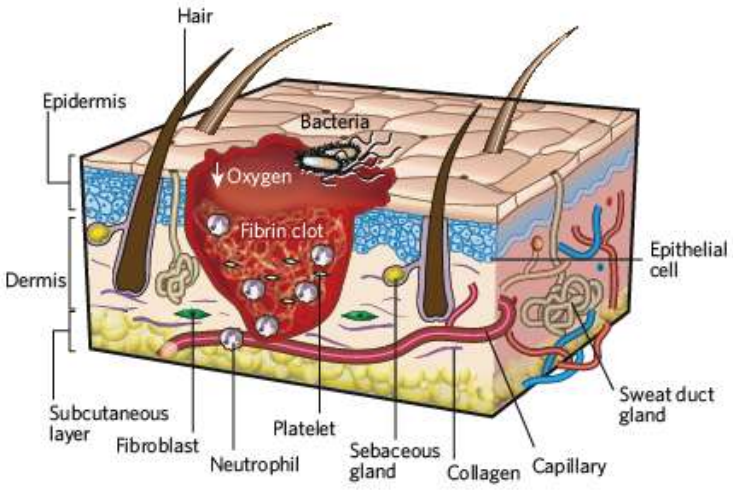

Figure 1.4 *– Haemostasis phase. Formation of a platelet plug, followed by a fibrin matrix which serves as scaffold for infiltrating cells (Gurtner, et al., 2008)*

Inflammation follows haemostasis and consists of a local release of cytokines and growth factors, an increased vascular permeability and the activation of infiltrating cells. Neutrophils are the first cells infiltrating the wound within an hour of injury and their number peak at 24-48 h. The migration of neutrophils is mediated by various factors such as interleukin (IL)-1 activation and transforming growth factor (TGF)-β signaling which causes the passage of the neutrophils mediated by a chemical gradient toward the wound; this process is termed chemotaxis (Broughton, et al., 2006).

The main role of neutrophils is phagocytosis of bacteria and tissue debris; when they have completed their function, they either undergo apoptosis or are phagocytosed by macrophages (Singh, et al., 2017; Simpson & Ross, 1972). Macrophages derive from monocytes and reach peak concentration at 48-72 hours after injury. Their role is fundamental to trigger the wound healing cascade and their activation is also important for debridement, matrix synthesis and angiogenesis. Macrophages are attracted to the wound by chemical messengers released from platelets; once activated they release cytokines that implicate angiogenesis, fibroplasia (Polverini, 1977) and nitric oxide (NO) synthesis, which is important for collagen formation. After 72 hours lymphocytes develop in the wound and produce an extracellular matrix scaffold that provides a support for collagen remodelling (Peterson, et al., 1987).

As some studies show, inflammatory phase is crucial for the correct evolution of the healing process. A reduced or increased inflammatory response leads to the failure of healing process (Koh & DiPietro, 2013; Sindrilaru, 2011; Zamboni, 2006; Khanna, 2010; Acosta, 2008).

1.3.2 Proliferation

This stage develops about 2-10 days after injury, when the haemostasis has been concluded and the wound is debris free. It includes angiogenesis, fibroblast migration and epithelialization (Singh, et al., 2017). Angiogenesis is triggered by growth factors released from platelets, such as TGF-β, platelet derived growth factor (PDGF), fibroblast growth factor 2 (FGF2) and cytokines. The low oxygen tension in the wound environment stimulates the release of the vascular endothelial growth factors (VEGFs) which, in combination with other chemical messengers, lead to the neovascularization and the regeneration of damage blood vessels (Remensnyder & Majno, 1968). New capillary buds sprout from blood vessels neighbouring to the wound and extend into the wound area to form a rich vascular network of capillaries (Ausprunk & Folkman, 1977).

The growth factors released from haemostasis clot also stimulate the migration of fibroblasts that reach peak number around the seventh day after the injury (Ross & Benditt, 1961). PDGF, FGF2 and epidermal growth factors (EGFs) also induce the proliferation of fibroblasts with a rapid expansion in the wound site (Clark, 1988). These cells produce extracellular matrix proteins, such as hyaluronan, fibronectins, proteoglycans and mostly collagen, responsible for tissue reconstruction by forming the bulk of the mature scar (Werner, et al., 2007). The levels of collagen increase rapidly for three weeks and they continue to gradually rise for three months after wounding (Madden & Peacock Jr, 1968). Epithelization occurs on the surface and begins within a few hours of injury, differently from the synthesis of collagen that involve the deeper layers of the wound. Keratinocytes migrate from the edges of the wounds under the eschar, filling the wound; they continue to move over one another until the defect is covered (Figure 1.5).

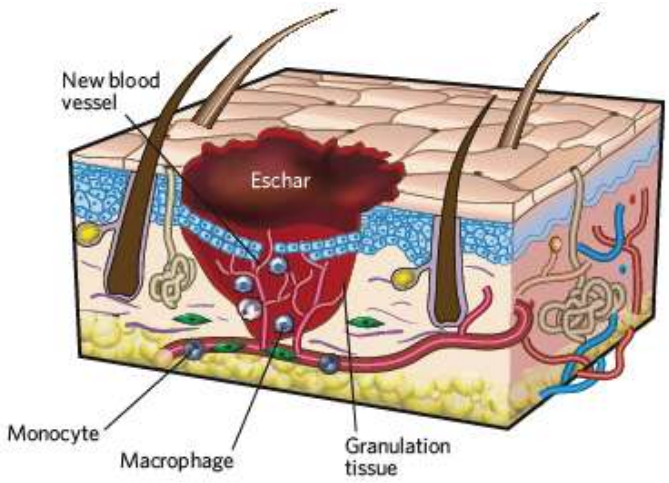

Figure 1.5 *– Proliferation phase. New blood vessels populate the wound and epithelial cells migrate under the scab (Gurtner, et al., 2008).*

Once the defect has been filled, changes in cytokine concentration cause epithelial cells switching from a motile phenotype to a mitotic one, becoming more columnar in shape (De Donatis, et al., 2010). At the end of this stage the layering of the epithelium is re-established and it is keratinized (Johnson & McMinn, 1960).

1.3.3 Maturation and Remodelling

This phase begins 2-3 weeks after injury and can take up to 2 years; it consists in the restoration of the physiological epithelium and maturation of the scar tissue.

In the early stages of wound healing the wound matrix is predominantly composed of fibrin and fibronectin, while towards the end of the process the synthesis of collagen III increases. The synthesis of this fibrous protein increases for at least 4-5 weeks after wound occurs (Diegelmann, et al., 1975; Madden & Peacock Jr, 1968) and each cell is responsible for its production. Fibroblasts produce also fibronectin, glycosaminoglycans and other matrix constituents (Kurkinen, 1980). Over 6-12 months the extracellular matrix at the wound is remodelled and type III collagen is mainly replaced by type I collagen which is typical of an intact dermis tissue (Gurtner, et al., 2008; Lovvorn, 1999). In fact, physiological tissue is composed of collagen I (80-90%) and III (10-20%). The organisation of collagen fibers changes as well during wound healing; they are initially deposited in a random way but thereafter fibers are organized by cross-linking into aligned bundles oriented along the lines of stress in the healing wound (Figure 1.6) (Tejiram, et al., 2016). The correct correlation between fiber thickness and orientation with stress lines is demonstrated by the elevated scar tensile strength (Doillon, 1985). However, diameter of collagen fibers in wounded tissue is thinner than that of fibers in nonwounded skin; this is caused by increased hydroxylation and glycosylation of lysine residues (Forrest, 1983). Furthermore, the orientation of fibers in scar tissue remains different from that in the intact dermis and the strength is less than the strength of unwounded skin. After 3 months the scar shows only 80% of the strength of physiological tissue and it does not increase further (Levenson, 1965).

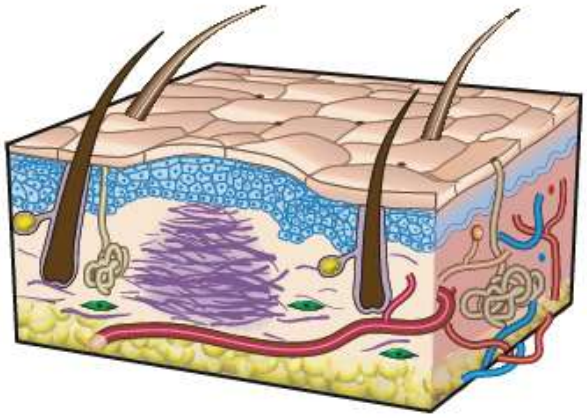

***Figure 1.6** – Maturation and remodelling. Disorganized collagen fibers have been produced by fibroblasts (Gurtner, et al., 2008).*

1.3.4 Wound contraction

Wound starts to contract around 7 days after injury, by approaching its edges together. This process is mediated by myofibroblasts which are subjected to contraction because of the presence of α-smooth muscle actin in thick bundles called stress fibers. Interactions between actin and myosin pull the cell cytoskeletons together and lead to a decrease of area of wound (Schmitt-Graff, 1994; Singh, et al., 2017).

Rate of contraction is generally around 0.75 mm per day and it depends on many factors such as wound shape; linear wounds contract faster than circular wounds.

The cells most involved in these phases and their main functions are listed in Table 1.4.

Table 1.4 - *Summary of the main types of cells involved in wound healing process.*

Cell type	Time of action	Function
Platelets	Seconds	➢ Clot formation ➢ Activation of coagulation pathways ➢ Release inflammatory mediators (PDGF, TGF-β, FGF, EGF)
Neutrophils	1-24 h	➢ Phagocytosis of bacteria ➢ Wounds debridement ➢ Increase vascular permeability
Keratinocytes	8 h	➢ Stimulate neighbouring keratinocytes to migrate ➢ Neovascularization
Macrophages	48-72 h	➢ Trigger the wound healing cascade ➢ Debridement ➢ Matrix synthesis ➢ Angiogenesis
Lymphocytes	72-120 h	➢ Produce an extracellular matrix scaffold
Fibroblasts	120 h	➢ Synthesis of granulation tissue ➢ Collagen synthesis ➢ Produce components of extracellular matrix

1.4 Electrical Fields in Wound Healing

Electrical fields are generated from a current flow, which is the result of an electrical potential difference in a conductive medium (Messerli & Graham, 2011). In humans there are two principal electrical potentials: the trans-plasma membrane electrical potential and the trans-epithelial potential (TEP). The latter is maintained across the epithelium layer by the transport of ions; for instance, the flow of cations (Na^+) and anions (Cl^-) through the pumps in corneal epithelium provides a TEP. As shown in Figure 1.7, this directional flow leads to a positive net charge at the basal side of the epithelial membrane and a negative net charge at the apical side (Levin, et al., 2006; Candia, 2004).

The trans-epithelial potential is present in many other types of epithelia such as respiratory, urinary, gastrointestinal, bile duct systems and cerebral, breast, prostate cavities, retina and ocular lens (Friedman & Gesek, 1995; Zhao, 2008). In humans, it ranges between 10 mV and 60 mV in relation to the body district measured (Foulds & Barker, 1983).

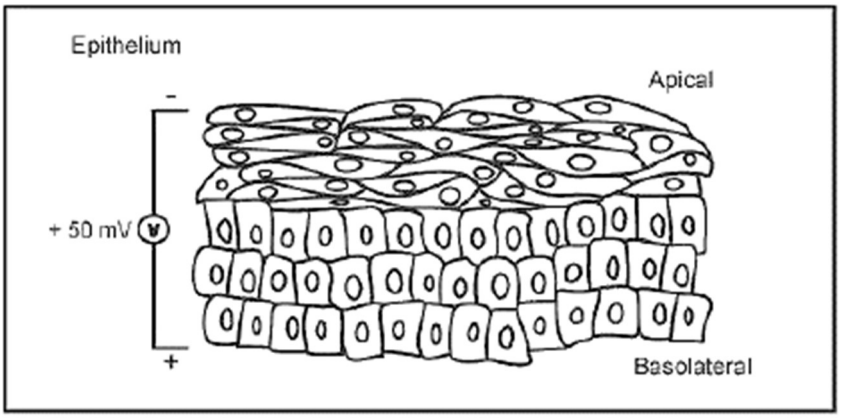

***Figure 1.7** – The trans-epithelial potential is established by the negative net charge at the apical side and by the positive net charge at the basal side (Messerli & Graham, 2011).*

When an injury occurs and the high-resistance tight junctions of epithelium are damaged, a lower resistance pathway is generated; it short-circuits the TEP which becomes negative at the site of the wound. Therefore, a potential gradient is generated between the site of injury and the surrounding nonwounded tissue. As a result, a current flow develops at the wound inducing the oriented endogenous electric fields (EFs) (Figure 1.8).

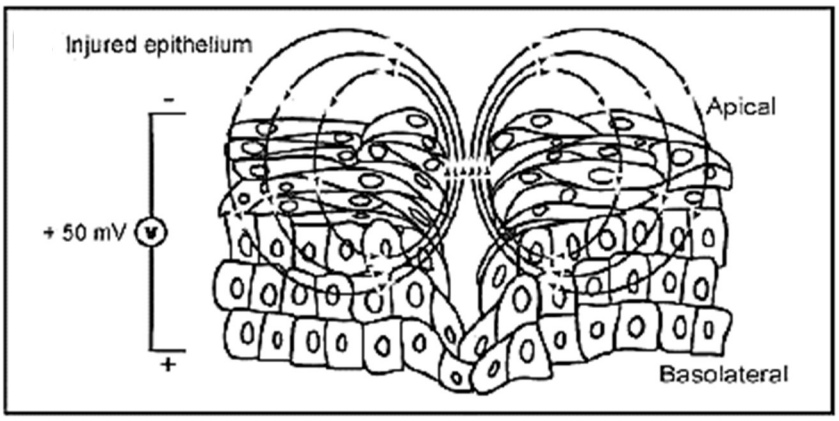

Figure 1.8 – *The arrows represent the current flow near the damaged epithelium. The wound is electrically negative with respect to the nonwounded tissue (Messerli & Graham, 2011).*

Current flow values vary between 1 and 10 μA/cm^2 with a current density up to 300 μA/cm^2 near the wound edges. These currents induce endogenous electric fields between 40 and 200 mV/mm (Messerli & Graham, 2011; Barker, et al., 1982). The cells of the surrounding tissue are then subjected to a strong and directional signal, oriented towards the site of the lesion. This force guides epithelial cells to migrate into the injury, thus promoting wound healing. The endogenous electric field is essential for the correct skin regeneration, because a defective cells migration can cause the onset of chronic wounds such as decubitus ulcers and venous stasis ulcers (Zhao, 2008; Eaglstein & Falanga, 1997).

German physiologist Emil Du-Bois Reymond, considered to be the founder of the novel electrophysiology, was the first to measure a flow of current in wounds (Zhao, 2008). Over the years several studies were conducted in order to demonstrate the effectiveness of electric fields in the wound healing process. For instance, Colin D. McCaig and coworkers developed a monolayer scratch wound model and an excised whole corneal preparation on which they applied a physiological DC EF (McCaig, 2005). They observed that the electric field was fundamental to the closure of the wound and influenced positively the wound healing process.

2 Tissue Engineering for Skin Regeneration

Various regenerative strategies have been developed to improve the healing process for chronic wounds and complicated injuries with an abnormal healing. These include the use of biomimetic scaffolds, the manipulation of the mechanical or electrical properties of the skin, the control of small molecules, the application of gene-therapy approaches and the use of cell-based strategies (including administration of epithelial stem cells) (Figure 2.1) (Gurtner, et al., 2008). These therapies can be used alone or combined to promote skin regeneration (Than, et al., 2016).

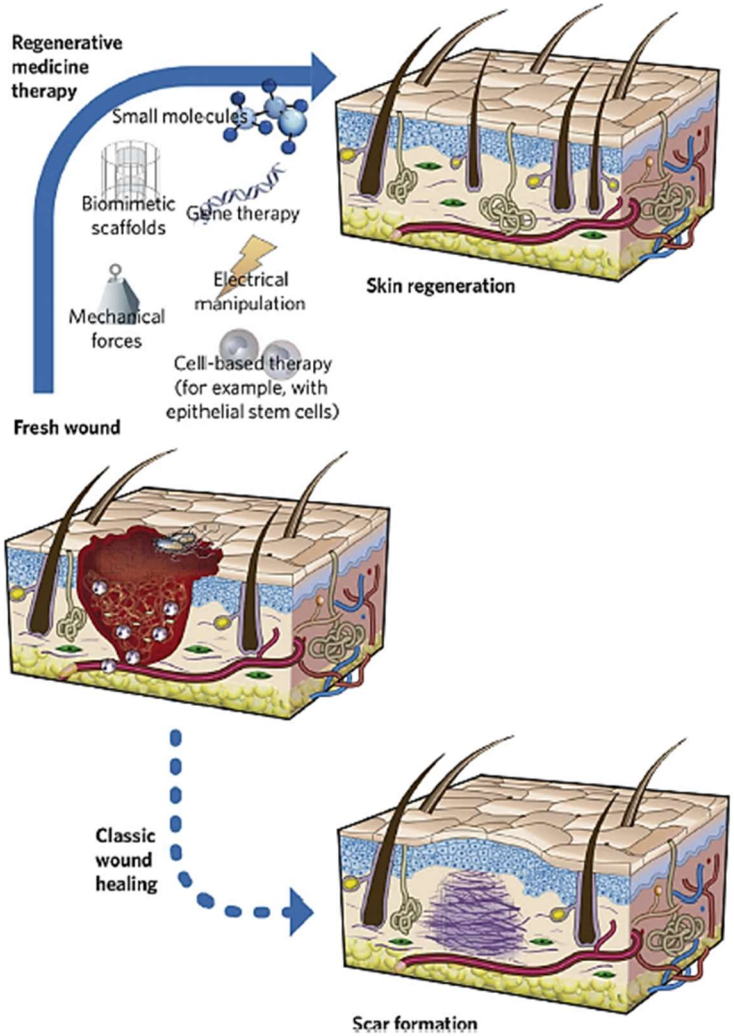

Figure 2.1 *– Regenerative therapies used in skin tissue engineering field to promote the repair of skin when the physiological wound healing process does not occur (Gurtner, et al., 2008).*

A Tissue Engineering (TE) scaffold is a three-dimensional structure or mesh that supports the spatial distribution of cells by providing them with a site for anchorage, proliferation, differentiation and secretion of extra cellular matrix (ECM) (Geetha, 2017). Scaffolds work as porous templates to support the growth of skin tissue and to ensure both the transport of nutrients and the removal of metabolic wastes (Mohanty, 2015). They can also deliver and retain cells, biochemical factors and nanoparticles. Furthermore, it is possible to optimize the scaffolds to provide precise stimuli that can induce specific cellular responses. Skin substitutes and bioactive wound dressings are scaffolds designed to promote wound closure and the restoration of skin functions.

Because the thesis focuses on the development of responsive wound dressings, here an overview about skin substitutes is given, while wound dressings are discussed in detail in the following section. Different typologies of wound dressings, including bioactive and advanced dressings, will be described, together with their main features and the materials used to fabricate them.

Skin substitute products can be defined as epidermal, dermal or dermo-epidermal (composite) according to the affected anatomical structure and they can be permanent, semi-permanent or temporary related to the duration of the cover. It is possible to realize cellular substitutes, on which cells can be seeded *in vitro* or *in vivo*, and acellular substitutes. There are two main classes of biomaterials for skin substitutes: biological materials (autologous, allogeneic and xenogeneic) and synthetic materials (biodegradable, non-biodegradable) (Nathoo, et al., 2014). Figure 2.2 shows a diagram of skin substitutes divided according to the wound type.

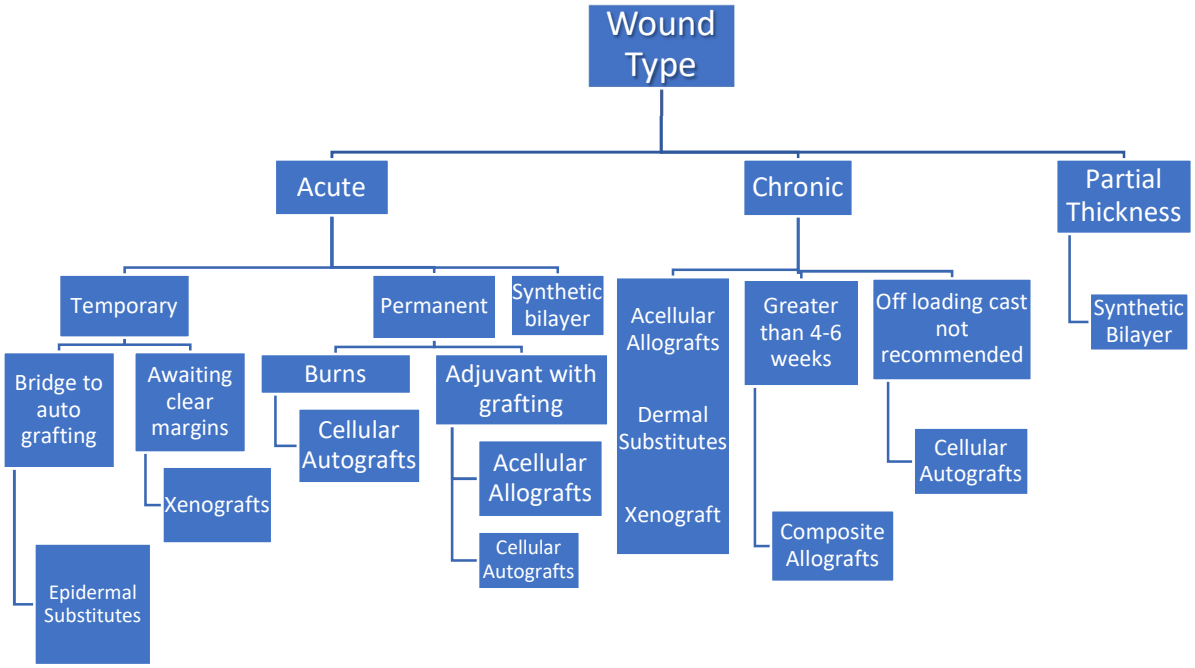

***Figure 2.2** – Relationship between skin substitutes and wound types (Nathoo, et al., 2014).*

2.1 Wound Dressings

The origin of wound dressings goes back to 1600 BC, when strips of linen soaked in oil or grease covered with plaster were used. Other examples include wool boiled in water or wine used by ancient Greeks as a bandage (Daunton , et al., 2012). Over the centuries, the dressings have been perfected following several key principles in the treatment of wounds, leading to the development of modern dressings in the 20th century. During the World Wars non-adhesive dressings and semipermeable membrane wound dressings based on cellophane were developed as alternative to the traditionally used gauzes (Thomas, 2010; Bloom, 1945). These dressings ensured a faster re-epithelialization and collagen synthesis. They also promoted angiogenesis by creating hypoxia to the wound bed and decreased wound bed pH, which leads to the control of wound infections (Dhivya, et al., 2015; Sujatha , 2012). In 1962 Winter conducted landmark study demonstrating the efficacy of moist wound healing by occlusive dressings (Gates & Holloway, 1992). During the 1990's, synthetic wound dressings were developed, such as hydrogels, hydrocolloids, alginates, synthetic foam dressings, silicone meshes, tissue adhesives, vapor-permeable adhesive films and silver/collagen containing dressings (Dhivya, et al., 2015).

2.1.1 The Ideal Wound Dressing

A wound dressing should respect a series of requirements (Dhivya, et al., 2015; Meikle, 2016; Manoukian, 2016):

- Protect the wound from colonisation by microorganism and environmental particulates
- Allow gaseous exchange of O_2, CO_2 and H_2O vapour
- Not contaminate the wound with particles of toxins
- Allow easy removal of dressing after healing
- Maintain the wound warm and moist
- Enhance epidermal migration
- Promote angiogenesis and connective tissue synthesis
- Assist in the removal of wound exudate and necrotic tissue
- Be comfortable and mouldable to the wound
- Allow wound to be monitored easily
- Have elasticity and high mechanical strength
- Be compatible with topical therapeutic agents
- Be biocompatible (sterile, non-toxic and non-allergic)
- Be biodegradable.

The main characteristics of the ideal wound dressing are represented in Figure 2.3.

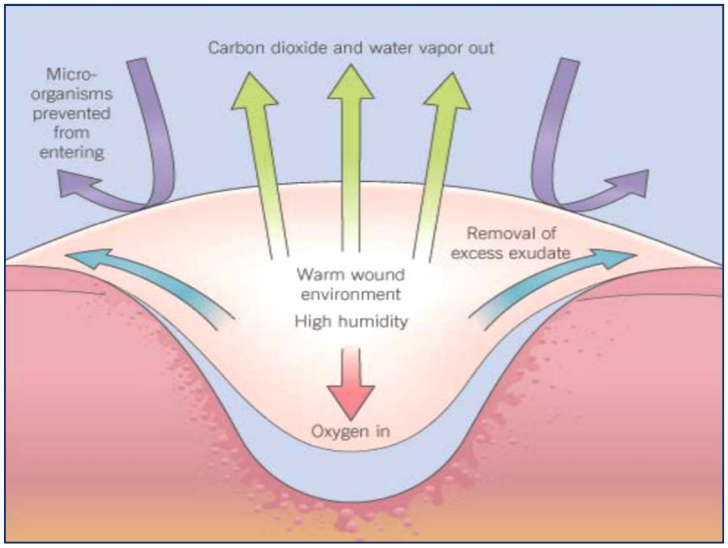

***Figure 2.3** – The principal functions that a wound dressing should perform (Bolognia , et al., 2003).*

2.1.2 Traditional Dressings

The main functions of traditional dressings are to facilitate haemostasis and protect the wound from contaminations (Sheridan & Tompkins, 1999). They include gauze, lint, plasters, bandages (natural or synthetic) and cotton wool. Gauze dressings can made of woven and non-woven fibers of cotton, rayon and polyesters and provide a barrier against external pathogens. However, this type of dressings causes the dehydration of the wound and requires frequent changing to avoid the maceration of nonwounded tissues (Dhivya, et al., 2015; Naimer & Chemla, 2000). The dried nature of gauze and the excessive wound drainage lead to adhesion phenomena that make the injury painful during the dressing removal. Bandages made of natural cotton wool and cellulose are indicated for retention of superficial wounds while synthetic bandages made of polyamide materials are suitable for chronic wounds because of their higher compression ability. Generally traditional dressings are used as primary or secondary wound dressings. The first ones are applied directly on clean and dry wounds with bland exudate levels while secondary dressings secure the primary wound dressing in place (Dhivya, et al., 2015). Some examples of traditional commercially available dressings are summarised in Table 2.1.

Table 2.1 *– Examples of traditional wound dressings in the world market (Aramwit, 2016; Sezer & Cevher, 2011).*

Dressing material	Brand name
Absorbent cotton pad	Telfa® "Ouchless" nonhaderent dressing
Absorbent cotton fibers impregnated with polyhexamethylene biguanide	Telfa AMD®
Highly absorbent cotton wool pad	Gamgee® pad
Highly absorbent rayon/cellulose blend sandwiched with a layer of antoshear high-density polyethylene	Exu-Dry® dressing
Paraffin gauze dressing	Jelonet®, Adaptic®
Paraffin gauze dressing containing 0.5% chlorhexidine acetate	Bactigras®
Petrolatum gauze containing 3% bismuth tribromophenate	Xeroform®
Scarlet red dressing	Scarlet Red®

Traditional dressings are generally highly permeable and non-occlusive and they can be defined as passive (Dhivya, et al., 2015). The low cost is the major advantage of this category, but the several disadvantages led to the development of modern dressings.

2.1.3 Modern Interactive Dressings

Interactive dressings not only cover the lesion as passive dressings, but also promote the healing process by creating a moist environment and by interacting with wound site components (Dhivya, et al., 2015; Swezey, 2010). Indeed, they reduce bacterial colonization and provide protection for the epithelializing bed, decrease the exudate level, improve the water retention of the wound bed, promote the formation of the collagen matrix and remove metabolic waste (Swezey, 2010).
Interactive dressings are typically semi-occlusive or occlusive and can be defined as bioactive for their ability to trigger a response in the organism (Dhivya, et al., 2015). Examples of bioactive dressings are in the forms of semipermeable films, hydrogels, hydrocolloids, hydrofibers, foams, alginate dressings and antimicrobial dressings (Vowden & Vowden, 2017). Figure 2.4 shows the algorithm to select the appropriate wound dressing.

Semipermeable films are made of polyurethane coated with an acrylic adhesive and can be use as primary or secondary dressings. The semi-occlusive nature of these dressings allows to keep the wound bed moist and leads to the autolytic debridement of the necrotic wounds. Films dressings are very flexible and highly elastic. They are suitable for epithelializing, superficial and shallow wounds with low exudate levels (Dhivya, et al., 2015; Vowden & Vowden, 2017).

Hydrogels dressings are made of insoluble hydrophilic materials, such as poly(methacrylate) and polyvinyl pyrrolidine. Generally, hydrogel dressings can be in three different forms: amorphous gel, impregnated-gauze and sheet hydrogel. The high water load of hydrogels (70-90 %) allows maintaining the environment moist and clean, and promotes the autolytic debridement of the necrotic wounds. They are indicated for wounds with moderate exudate levels and particularly for pressure ulcers, necrotic wounds, skin tears, surgical wounds and burns (Vowden & Vowden, 2017).

The main disadvantages of these products are the low mechanical resistance and the excessive accumulation of exudate, which leads to the wound maceration (Martin, et al., 2002).

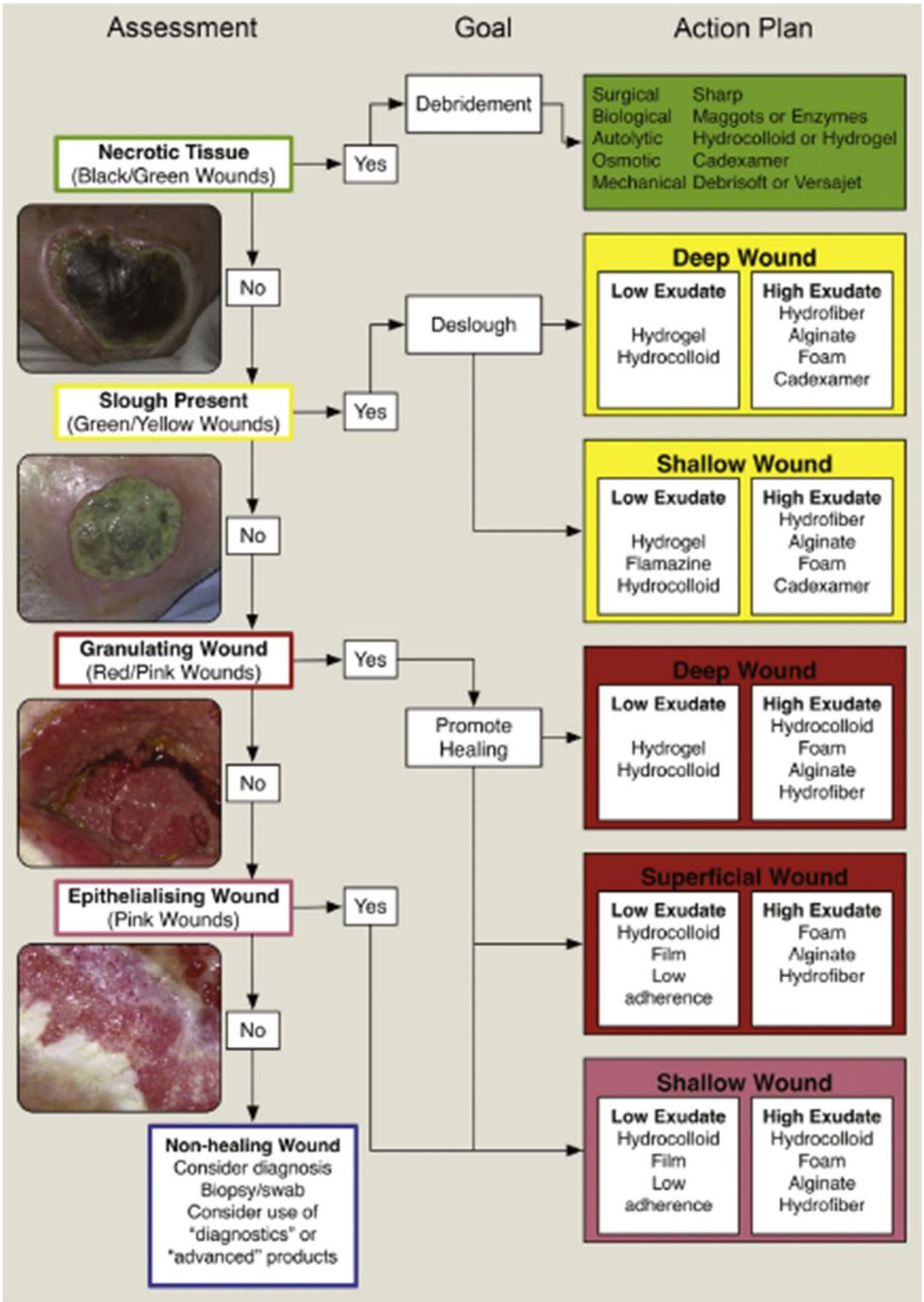

Figure 2.4 - *Selection process based on wound depth, exudate levels and wound bed characteristics, for available modern dressings (Vowden & Vowden, 2017).*

Hydrocolloids are the most common interactive dressings and consist of two layers: an inner colloidal layer and an outer water-impermeable layer. They are made of absorptive materials, such as carboxymethylcellulose, pectin or gelatine, in combination with elastomers and adhesive (Boateng, et al., 2008). An important aspect of these dressings is their capability to form gels in contact with wound exudate, by providing a moist environment that protects the granulation tissue. Furthermore, hydrocolloids decrease the pH of the wound surface and create an acidic environment that inhibits bacteria growth (Vowden & Vowden, 2017). This type of dressings is indicated for partial- or full-thickness acute and chronic wounds. However, they are not suitable for highly exudate levels or infected wounds, and they are more appropriate as secondary dressings.

Hydrofiber dressings are hydrocolloids with higher absorbent properties and made of sodium carboxymethyl cellulose. These dressings can absorb up to 25 times their own weight before degradation.

Foam dressings are either hydrophilic or hydrophobic materials and they are semipermeable. They are made of polyurethane and silicone that make the foam conformable to the wound shape. Adhesive and non-adhesive foam dressings exist. This category is indicated for chronic wounds and for wounds with high exudate levels. Foam dressings are typically used as primary dressings to absorb high volumes of wound exudate. The main disadvantage of foam dressings is that they are not suitable for low exudate levels, dry wounds and dry scars (Marcia & Castro, 2002).

Alginate dressings contain sodium and calcium salts with mannuronic and guluronic acid units. Alginate is derived from brown seaweed and can form non-woven sheets and ropes. These dressings have a high absorption capability due to the hydrophilic gel formation that decreases the exudate levels and reduces the number of bacterial colonies. Furthermore, in contact with the wounded tissue, ions contained in the alginate are exchanged with blood by generating a defensive film. Alginate dressings are indicated for moderate to heavy exudate wounds and they are not suitable for low drainage, dry and deep wounds (Dhivya, et al., 2015; Vowden & Vowden, 2017).

Antimicrobial dressings act by preventing infections and by facilitating tissue regeneration. These dressings incorporate antimicrobial agents such as products iodine-based (cadexomer iodine and povidone iodine), silver-based (silver sulfadiazine and ionic silver-impregnated dressings) and products with antiseptic agents (polyhexamine) Honey is another agent that can be incorporated into these dressings and acts as a debriding agent (Vowden & Vowden, 2017). Antimicrobial dressings are indicated for necrotic and infected wounds, such as diabetic foot ulcers. Generally, they are used for short periods and when strictly necessary in order to avoid side effects such as skin irritation and staining (Dhivya, et al., 2015).

Some examples of modern interactive commercially available dressings are summarised in Table 2.2.

Table 2.2 - *Examples of modern wound dressings in the world market (Dhivya, et al., 2015; Basu, et al., 2017).*

Dressing material	**Brand name**
Semipermeable films: polyurethane coated with an acrylic adhesive (chitosan, gelatine, cellulose)	Opsite™, Tegaderm™, Biooclusive™
Hydrogels dressings: polymers, sheet dressings, impregnated gauze and water-based gels (hyaluronic acid)	2nd Skin®, Intrasite™, Nu-gel™, Aquaform™
Hydrocolloids: sheets or thin films	Granuflex™, Comfeel™, Tegasorb™
Foam dressings: hydrophobic and hydrophilic materials	Lyofoam™, Allevyn™ and Tielle™
Alginate dressings: sodium alginate, calcium alginate, polysaccharide	Sorbsan™, Kaltostat™, Algisite™
Antimicrobial dressing	Cutisorb™

2.1.4 Advanced Dressings: Responsive and Biomimetic

In recent years advanced dressings have been developed to provide an optimum environment for skin growth and regeneration. These include responsive dressings that can be sensitive to several factors, such as temperature, pH, enzymes, mechanical deformation, electrical or magnetic field. Responsive materials respond in various ways to external stimuli, like altering colour or transparency, becoming conductive or permeable to water or changing shape (Aguilar & San Roman, 2014). For instance, thermo-responsive dressings are used to adhesion control by exploiting the hydration-dehydration transition in response to temperature change. Indeed, removing the wound dressing is a critical part of healing process as it can cause pain and the onset of secondary injuries (Deng , et al., 2017). Chen et al. developed a chitosan wound dressing with temperature-responsive characteristics that allows to obtain easily stripped off property. They used poly(N-isopropylacrylamide) (PNIPAAm), a polymer which exhibits a lower critical solution temperature (LCST) and remarkable hydration–dehydration changes in response to relatively small changes in temperature (Chen, et al., 2012). pH is another parameter that can be exploited in wound care because it both reflects and influences numerous fundamental physiological and biochemical processes involved in wound healing. In their work, Liu et al. produced a novel smart hydrogel-based wound patch incorporating modified pH indicator dyes to monitor the state of healing process. When pH increased, the colour of the hydrogel patches ungo a transition from yellow (pH 5,6 and 7) to orange (7.4 and 8), and finally to red (pH 9). This range indicates the presence of chronic and infected wounds that show alkaline condition (Liu, et al., 2017).

The work of this thesis focuses on dressings that respond to mechanical stimulation. They are made of piezoelectric materials that can generate electric fields (EFs) even under small mechanical deformations and can mimic the endogenous electric fields normally existing in wounded skin (see paragraph 1.4) (Wang & Song, 2006).

Bhang et al. developed a bidirectionally grown zinc oxide nanorod (BDG ZnO NR)-based piezoelectric patch (PZP) and evaluated its therapeutic efficacy for wound healing. These dermal patches have been applied on the wounds of animal models and piezoelectric potentials have been induced by the animal motion. *In vivo* and *in vitro* data demonstrated the beneficial effects of these dressings on cellular activities by enhancing cellular metabolism, migration and protein synthesis (Bhang, et al., 2017).

Biomimetic dressings from another class of advanced dressings. They mimic the extracellular matrix (ECM) by providing structural support and physical environment for cells to attach, grow, migrate and respond to signals (Chan & Leong, 2008). The purpose of these scaffolds is that to emulate the architectural, biological and mechanical features of ECM (Table 2.3).

Table 2.3 - *Comparison between the characteristics of the ECM in the native tissue and those of the biomimetic dressings (Chan & Leong, 2008).*

Functions of ECM in native tissues	**Analogous functions of scaffolds**	**Architectural, biological, and mechanical features of scaffolds**
Provides structural support for cells to reside	Provides structural support for exogenously applied cells to attach, grow, migrate and differentiate	Biomaterials with binding sites for cells; porous structure with interconnectivity for cell migration and for nutrients diffusion; temporary resistance to biodegradation upon implantation
Contributes to the mechanical properties of tissues	Provides the shape and mechanical stability to the tissue defect	Biomaterials with sufficient mechanical properties filling up the void space of the defect and simulating that of the native tissue
Provides bioactive cues for cells to respond to their microenvironment	Interacts with cells actively to facilitate activities such as proliferation and differentiation	Biological cues such as cell-adhesive binding sites; physical cues such as surface topography
Acts as the reservoirs of growth factors and potentiates their actions	Serves as delivery vehicle and reservoir for exogenously applied growth-stimulating factors	Microstructures and other matrix factors retaining bioactive agents in scaffold
Provides a flexible physical environment to allow remodelling in response to tissue dynamic processes such as wound healing	Provides a void volume for vascularization and new tissue formation during remodelling	Porous microstructures for nutrients and metabolites diffusion; matrix design with controllable degradation mechanisms and rates; biomaterials and their degraded products with acceptable tissue compatibility

Biomimetic wound dressings include nanofibers obtained with electrospinning technique, which will be explained in chapter 3. Electrospun nanofibers have diameters in the range of nanometres to micrometres. They possess a large specific surface area, a high aspect ratio, a high porosity, a controllable small pore size and the ability to resemble the extracellular matrix' architecture. The application of nanofibers for wound healing will be discuss in paragraph 3.1.3.

3 Micro- and Nanofabrication Approaches for Porous Scaffolds

The technologies used for the fabrication of porous scaffolds for tissue engineering are different and can be divided into two categories. The first includes the conventional techniques that allow to obtain biodegradable, biocompatible and biomimetic structures, with less control over their internal architecture. The second category, instead, includes unconventional rapid prototyping techniques that provide highly interconnected porous and reproducible structures (Loh & Choong, 2013).

All methods are listed in Figure 3.1. In this project electrospinning and 3D-printing have been used to create three dimensional and porous scaffolds for wound healing.

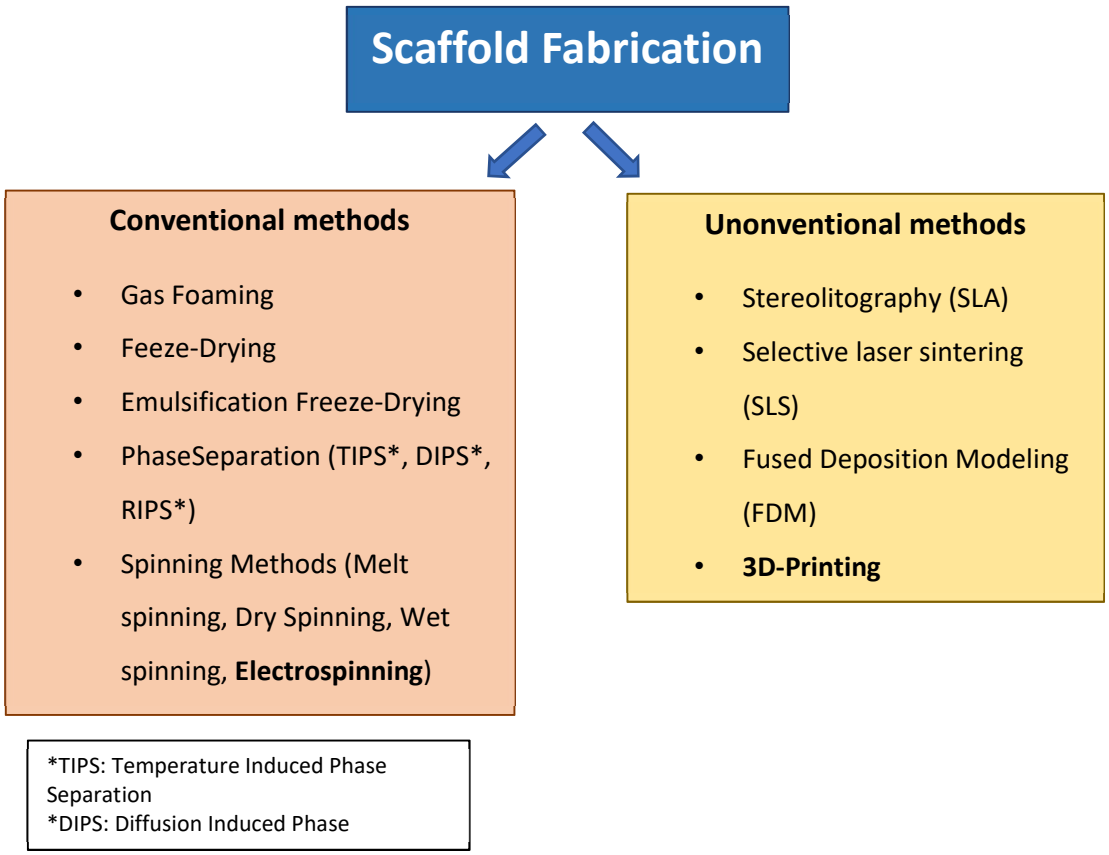

Figure 3.1 - *Summary scheme of three-dimensional scaffold manufacturing methods.*

3.1 Electrospinning

The electrospinning technique was introduced for the first time in the 1930s to make nonwoven products for industrial or domestic use. Only in the latest twenty years it has been adopted in the field of nanoscience and nanotechnology and it has become an effective and versatile method to create polymer nanofibers (Geetha, 2017; Thenmozhi, et al., 2017).

3.1.1 Apparatus and Process

The basic equipment consists mainly of four parts (Figure 3.2) (Geetha, 2017):

- syringe connected to a pump and containing the polymer solution of interest;
- needle spinneret linked to the syringe with variable size and geometry;
- high-voltage DC (Direct Current) power supply (from 1 to 40 kV);
- metal ground collector with variable morphology (typically flat plate or rotating drum).

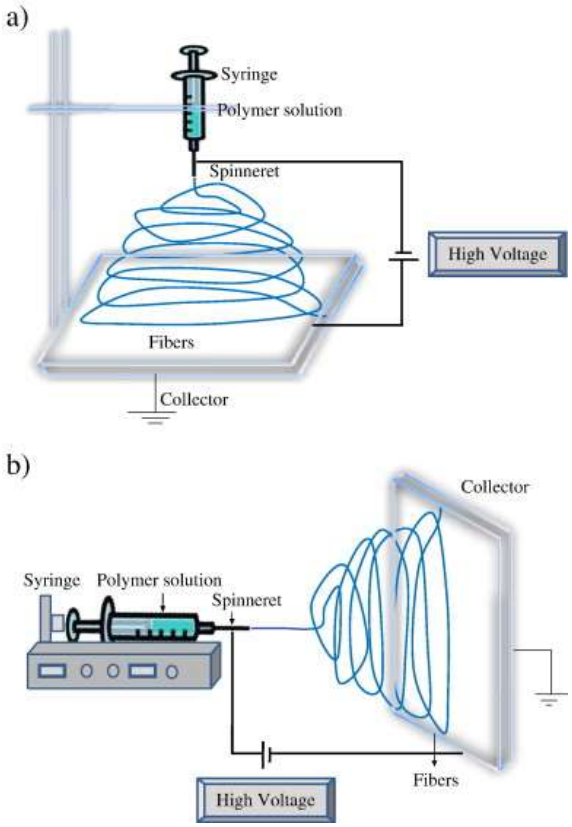

***Figure 3.2** – Electrospinning apparatus. Typical vertical (a) and horizontal (b) set up (Bhardwaj & Kundu, 2010).*

Electrostatic force is the key principle of this technique. The syringe pump drives the polymer solution contained into the syringe through a metallic needle that is connected to an electrode. A second electrode is connected to the collector. Between the two electrodes a high potential difference (up to 40 kV) is created and it is used to extrude polymer filaments that are which attracted to the collector (Thenmozhi, et al., 2017). In order to electrospin fibers, the electric field generated must be higher than the surface tension of the polymer solution. When the voltage is not applied, the solution forms a hemispherical drop on the tip of the needle and its shape depends on the solution surface tension. When, instead, a potential difference is imposed, the needle tip becomes charged and transfers the charge to the fluid surface. The hemispherical drop begins to deform under the effect of the repulsion force between the tip of the needle and the polymer solution (Rogina, 2014). By increasing the voltage, the pendant droplet is converted into a conical shape (Taylor cone) and the equilibrium of the electric forces and surface tension occurs. When the electrostatic repulsive forces overcome the surface tension of the drop a polymer solution jet is ejected from the Taylor cone and is accelerated by the electric field (Figure 3.3) (Geetha, 2017).

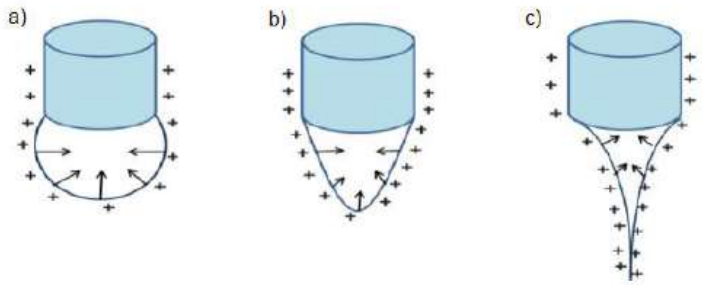

Figure 3.3 *– Effect of electric field on the polymer drop. The surface tension is higher than the electrical repulsion (a). The equilibrium between the forces occurs (b) Repulsive forces overcome the surface tension (c) (Laudenslager & Sigmund, 2012).*

The diameter of the spherical drop is of the order of hundreds of microns, while the jet has smaller sizes, around a few microns. During the elongation of the jet a redistribution of the charges inside the fluid occurs and the flow reorganizes to form a series of coils (Figure 3.4).

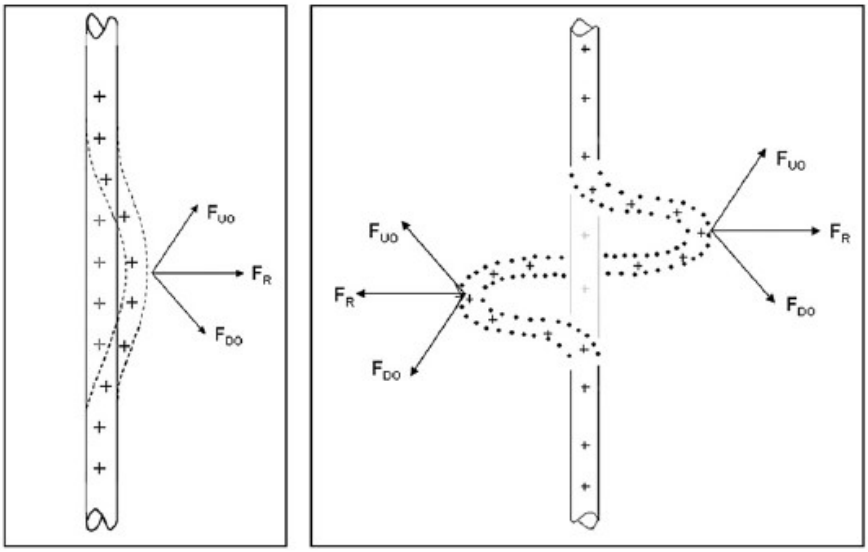

Figure 3.4 - *A perturbed segment of electrospinning jet in response to the repulsive electric forces between the uniformly distributed charges in the jet. The segment is forced by F_{DO} downward and outward and by F_{UO} upward an outward. The resultant of these forces F_R is in a radial direction with respect to the straight jet and increase exponentially in time (Reneker & Yarin, 2008).*

More precisely, the first region of electrospinning jet is the elongation flow the direction of which is parallel to the axis of the jet. After this first region a bending perturbation starts and develops into a coil that grows with a trajectory perpendicular to the jet axis (Figure 3.5) (Reneker & Yarin, 2008).

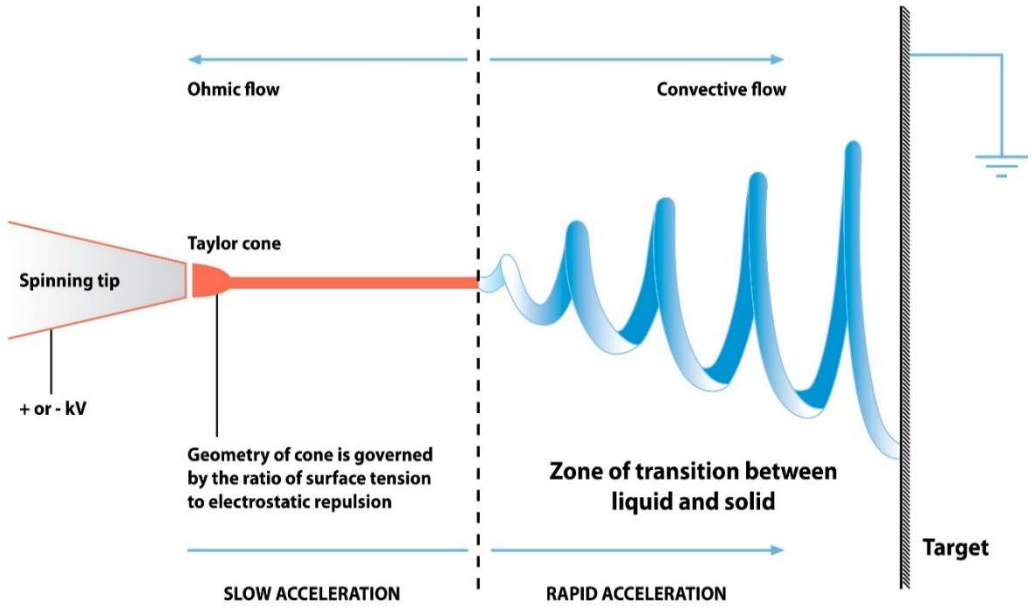

Figure 3.5 – *Diagram showing the jet trajectory. The first stretch is characterized by a laminar flow with a slow acceleration. In the second stretch, instead, the potential difference causes the insurgence of a turbulent flow and the development of coils (Gatford, 2008).*

Furthermore, the electrical field generates a coil with many turns that elongate in response to the Coulomb repulsion of the charge. During this phase the length of jet increases by large factors in a small region of space while its diameter decreases until reaching the order of nanometres. Generally, a succession of three or more smaller diameter bending instabilities occurs before the jet solidifies (Figure 3.6) (Reneker & Yarin, 2008). The flow acquires a fractal-like configuration with a complex trajectory the components of which are:

- the downward component driven by the voltage between the tip and the collector;
- the outward component driven in the first blending region by the radial electric force F_R shown in Figure 3.4 and then by the electrostatic repulsion carried by each coil.

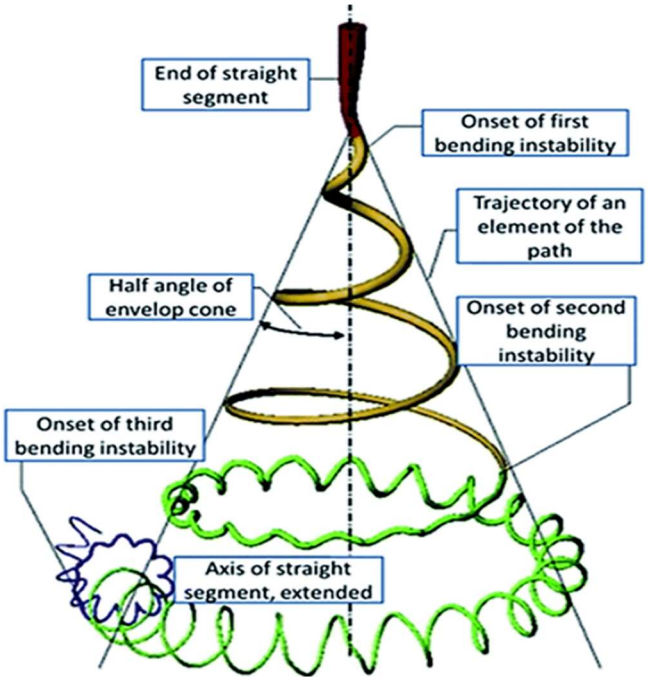

Figure 3.6 *– The typical electrospinning jet profile. The straight segment is shown in red, the first bending coil in yellow, the second one in green and the third bending coil in blue. The perimeter of each turn of coils grows monotonically (Reneker & Hou, 2004).*

By coiling the solvent evaporates and the polymer chains orient themselves and stretch. The jet solidifies on the collector by forming a solid network of nanofibers (Liu, et al., 2013; Qi & Craig, 2016; Kriegel, et al., 2008).

3.1.2 Process variables in electrospinning

The parameters that can influence the morphology and the sizes of fibers produced by electrospinning are classified as: process, systemic, solution and physical parameters (Table 3.1).

Table 3.1 *– Process variables in electrospinning (Zafar, et al., 2016).*

Process Parameters	**Systemic Parameters**	**Solution Parameters**	**Physical Parameters**
Voltage	Molecular weight	Viscosity	Humidity
Flow rate	Solvent used	Concentration	Temperature
Distance	Polymer structure	Conductivity	Air velocity
Collectors\Needles		Surface tension	

The *voltage* required to spin a solution varies from polymer to polymer. By increasing the potential difference, the electrostatic forces increase and cause an increment in charge density of the polymer solution. The result is an acceleration of the solution jet and a reduction in the volume of the drop adhered to the tip of the needle (Figure 3.7). Therefore, the fibers produced have a more elongated morphology and a reduced diameter (Sill & von Recum, 2008). An excessive increase in the voltage applied may result into the fragmentation of the jet and lead to the formation of beads. On the contrary, the application of a lower voltage allows to obtain thinner and defect free fibers (Liu, et al., 2017; Jiang, et al., 2007; Yao, et al., 2007).

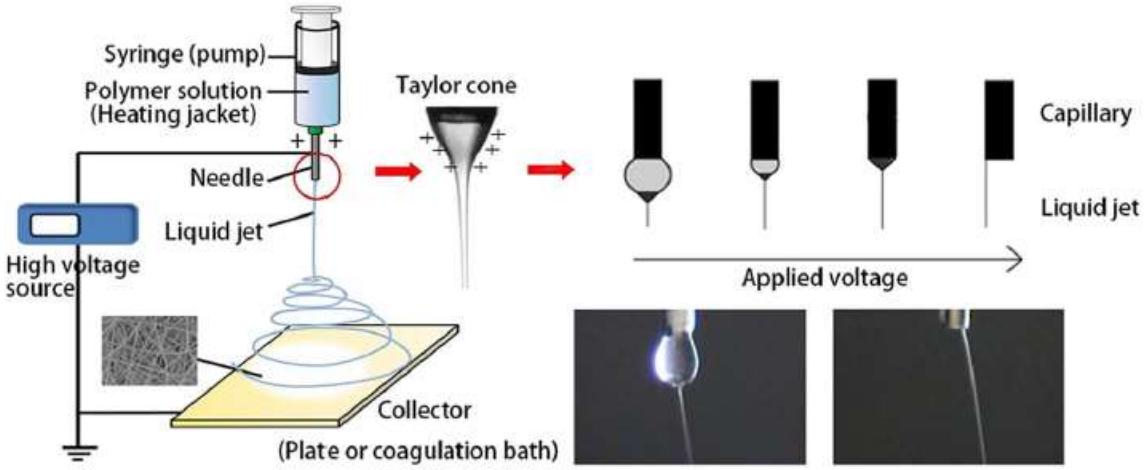

***Figure 3.7** - Schematic representation of the electrospinning apparatus. The drop size variation with increasing the applied voltage is in evidence (Sill & von Recum, 2008).*

The *flow rate* is another process parameter that influences size and morphology of fibers. An excessive increase in flow can lead to a deformation of Taylor cone with the formation of beads. Excessive flow rates can also develop ribbon-like fibers, mainly due to the lack of evaporation of the solvent and to the poor extension of the solution in the path between the needle and the metal collector (Megelski S., et al., 2002). On the other hand, an insufficient flow rate causes the drying of the droplet inside the tip (Rogina, 2014). By increasing the flow rate, the diameter of fibers increases. Indeed, the time necessary for the polymer chains to elongate and orientate themselves decreases (Liu, et al., 2017; Megelski S., et al., 2002).

The *distance* between the tip of the metal needle and the collector plays an essential role in determining the morphology of fibers. Indeed, the time of "flight", the evaporation rate of the solvent and the degree of elongation and winding of the jet depend on the distance between the tip and the collector (Matabola & Moutloali, 2013). This must guarantee the evaporation of the solvent in order to avoid the formation of ribbon and flattened fibers (Liu, et al., 2017; Sill & von Recum, 2008). Moreover, smaller diameters of fibers can be obtained with higher distances (Matabola & Moutloali, 2013). However, if the distance is excessive the jet breaks before reaching the collector and defects, such as beads, are formed (Liu, et al., 2017).

A variable component of the instrument is the *collector*, which has the role of fibers collection substrate.

The choice of the most appropriate collector depends on the desired type of fibers and their application (Thenmozhi, et al., 2017). Figure 3.8 shows three different collectors. Aluminium foils, conductive papers, conductive clothes, metal grids, pins, parallel bars, rotating rods and rotating cylinders can be used.

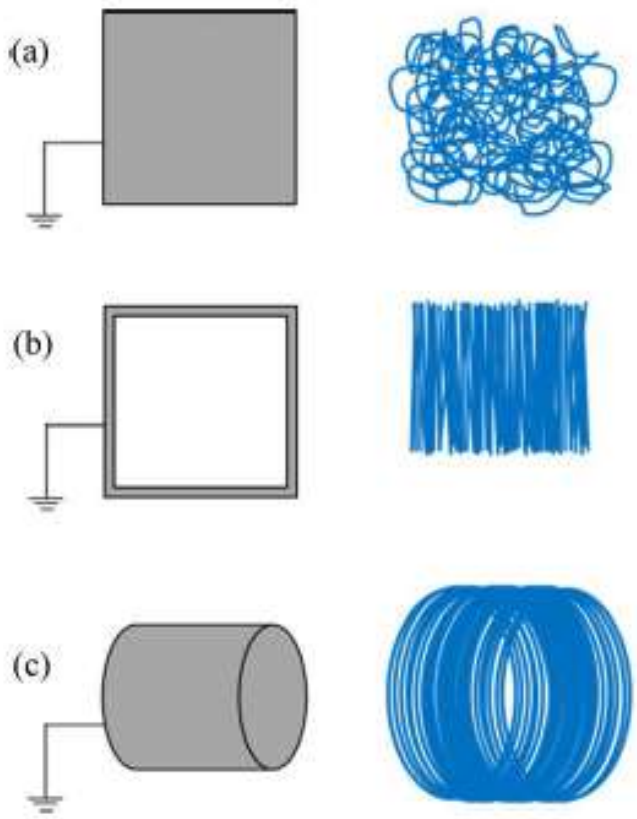

Figure 3.8 - *Schematic representation of the electrospinning collectors. Planar collector for randomly oriented fibers (a); square frame for unidirectional oriented fibers (b) and cylindrical collector for tubular oriented fibers (c) (Abrigo, et al., 2014).*

The type of *needle* used is another process parameter that influences the electrospinning process. Single or multiple nozzles or nozzles with a different number of axial units (mono-axial, co-axial and multi-axial) exist.

Molecular weight is an important systemic parameter that can modify the characteristics of fibers. Solutions of polymers with low molecular weights lead to fibers affecting by beads. On the contrary, polymers with higher molecular weights can be electrospun more easily because they are subjected to a major number of interchain interactions and entanglements that stabilize the jet. However, an increase in molecular weight causes the increment of fibers diameter (Thenmozhi, et al., 2017). It also influences viscosity, conductibility and surface tension of polymer solution (Rogina, 2014).

The choice of the *solvent* can be fundamental to obtain a good result. Solvents used for electrospinning process must be able to completely dissolve the polymers and they must be sufficiently volatile to evaporate in an appropriate time (Liu, et al., 2017).

Among the solution parameters, solution *viscosity* is the most critical variable that determines the possibility to obtain a continuous strand rather than a series of beads (Figure 3.9) (Jiang, et al., 2016). In general, a low viscosity allows to obtain smooth and homogeneous fibers, with small diameter and high mechanical resistance. However, excessively diluted solutions cause the lack of crosslinking of polymer molecules and the formation of beads (Balaji, et al., 2015).

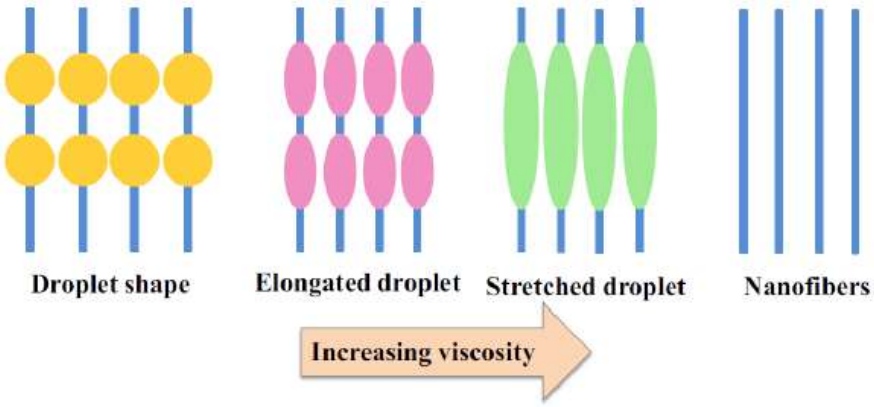

Figure 3.9 - *Relationship between viscosity increase and beads formation. Solutions with insufficient viscosity lead to the formation of spherical beads. By increasing the viscosity, elongated ellipse beads are obtained and when the optimal viscosity is reached defect free fibers are produced (Haider, et al., 2015).*

According to numerous studies, an ideal polymer *concentration* allows to generate fibers with good requirements and an optimal concentration depends on the type of used material (Haider, et al., 2015; Pillay, et al., 2013). When the concentration of the polymer solution is low, the applied electric field and the surface tension cause the fragmentation of the jet before it reaches the collector, leading to the formation of beads. On the contrary, a higher concentration of polymer increases the diameter of the fiber, allowing the formation of a continuous jet. However, an excessive concentration can hinder the ejection of jet, due to the high surface tension of the polymer (Rogina, 2014; Huang, et al., 2004; Zhu, et al., 2008).

The increase in *conductivity* of the polymer solution leads to the formation of homogeneous fibers with small diameters (Rogina, 2014). Indeed, a solution with an elevated conductivity forms a jet with a high charge resulting in a high concentration of electrostatic forces. It follows that the jet is more attracted to the collector, by extending more and producing fibers with a limited diameter (Liu, et al., 2017; Sill & von Recum, 2008). Otherwise, a low conductivity impedes the elongation of jet with consequent fragmentation of the strand and production of beads.

Surface tension is the energy required to increase the surface area of a liquid due to intermolecular forces. This solution parameter can be changed by modifying the concentration or the solvent type. By decreasing the surface tension of a solution, smooth, continuous and defect-free fibers can be obtained. Excessive surface tension can generate unstable jets and fibers with beads (Thenmozhi, et al., 2017; Yang, et al., 2004).

Temperature is a physical parameter that affects the spinning process and influences the characteristics of fibers. Environmental temperature determines the solidification time of flow and therefore the diameter of fibers. Indeed, by decreasing this parameter, the time of solidification increases, and the elongation of jet is promoted. The temperature influences also the stiffness of the polymer chains. At higher temperatures, polymer chains show more degrees of freedom and the viscosity of solution decreases by allowing the jet to form easily.

A relation between the *humidity* and the thickness of fibers exist and has been studied by (Pelipenko, et al., 2013). An extremely low humidity increases the degree of solvent evaporation and leads to the rapid increment of local polymer concentration. The polymer jet solidifies more rapidly resulting into an increment in fiber diameter. On the contrary, at high humidity conditions, solidification takes place more slowly and the jet is exposed to stretching for a longer time, with consequent formation of thin fibers. An excessive humidity causes breaking of the polymer cast into fragments, giving rise to the formation of beads (Pelipenko, et al., 2012).

3.1.3 Electrospun Nanofibers in Wound Healing

For wound dressing application, electrospinning represents a versatile technique to fabricate nanofibrous membranes that can create a moist environment around the wound area and promote healing (Liu, et al., 2017). The aim of using nanofibers is to reproduce a physiological environment for skin repair, by mimicking the extracellular matrix (ECM) structure and function (Rosic, et al., 2013). Due to the ability of fibrous mats to form an interconnected network with high porosity, electrospun fibrous webs represent effective wound dressing materials (Zahedi, et al., 2010). Indeed, the porous nature of fibers allows the drainage of the wound exudate and the gaseous exchange (Bhattarai, et al., 2004). In addition to the porosity, these fibers are characterized by sizes ranging from tens of nanometres to micrometres and by a high surface area (Zahedi, et al., 2010). The large surface area promotes intimate contact between fibers and cells and accelerates growth and differentiation of cells (Cao, et al., 2009). Furthermore, the high surface/volume ratio typical of the nanofibers allows loading considerable quantities of drugs, nanoparticles, growth factors and even cells. The structure of nanofibers guarantees also high mechanical properties and reproducibility (Liu, et al., 2017). Figure 3.10 shows a general scheme of electrospun fibers characteristics. Electrospinning technique is particularly suitable to produce wound dressings materials that can improve many aspects of wound healing (Zahedi, et al., 2010), such as haemostasis, water and exudate absorbability, moist environment control, conformability, and scar-free (Zahedi, et al., 2010; Zhang, et al., 2005). The promotion of haemostasis phase is due to the presence of small pores and high effective surface area that grant epithelial cells migration. The high surface/volume ratio allows a water absorption of 17.9-21.3% and considerable exudate absorption levels (Zhang, et al., 2005).

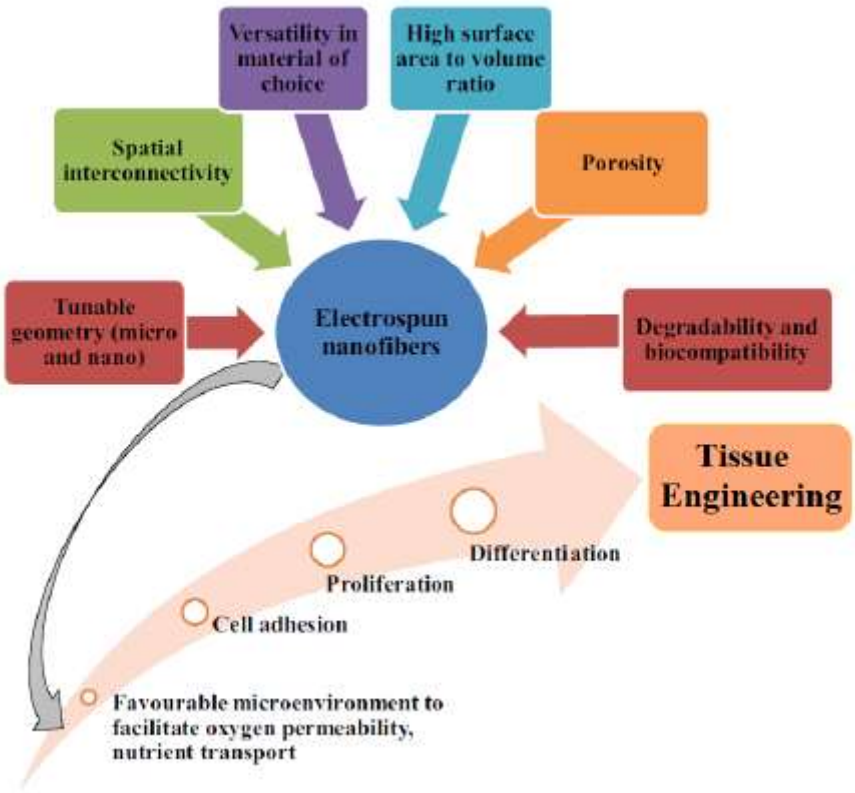

Figure 3.10 *- Characteristics of nanofibers obtained with the electrospinning technique for tissue engineering applications (Sun, et al., 2014).*

The moist environment control is granted by the porous structure of nanofiber dressings that gives the typical semi-permeability to the scaffold. This is excellent for exchange of gases and nutrients to the tissue to avoid the wound to dry up. Also, the small pore size can effectively protect the wound from microbial infections and allow a high gas permeation (Zahedi, et al., 2010). Furthermore, flexibility and resiliency of electrospun fibers make these materials able to conform to the contour of wounds. Finally, biodegradability is an additional characteristic of these scaffold that allows to obtain healing wounds without leaving scars. The adoption of nanofibers obtained with electrospinning technique for wound healing application therefore appears to be an effective therapeutic strategy.

3.2 3D-Printing

Additive manufacturing (AM) systems have been developed as advanced technologies to overcome the limitations of conventional methods such as imprecise pore size, undefined pore geometry, low levels of interconnectivity and limited mechanical properties (Do, et al., 2015). Rapid prototyping techniques can fabricate biomimetic 3D scaffolds with high precision and accuracy. They can be classified into laser-based, printing-based and nozzle/extrusion-based system. Laser-based system use photolithography to produce polymeric scaffolds while printing-based systems deposit a binder on a powder bed or directly use inkjet technology to print the structural material. Finally, nozzle-based techniques consist in the micro-extrusion/dispensation of a small-diameter polymeric filament through a nozzle having an orifice diameter in the range of hundreds of micrometres (Giannitelli, et al., 2015). 3D-Printing is a versatile technique that can fabricate scaffolds with complex shapes and with the ability to imitate the extracellular matrix (ECM) at nanoscale level, by providing a microenvironment for cell attachment, proliferation, distribution and differentiation. This technology uses a layer-by-layer process to fabricate the structure and involves a Computer-Aided Design (CAD) that is relayed to each 3D-printing system to "print" the desired scaffold structure (Do, et al., 2015).

This technique was first introduced in 1986 by Charles W. Hull. He called the method 'sterolithography' and described as a sequential print of thin layers of material that can be cured with ultraviolet light to generate a solid 3D structure (Murphy & Atala, 2014). This process was later applied in biomedical field to create resin molds for producing 3D scaffolds from biological materials. 3D-printing has been successively studied to realise the direct printing of biomaterials into 3D scaffolds that can be used for tissue regeneration with or without seeded cells (Nakamura, et al., 2010).

3.2.1 Apparatus and Process

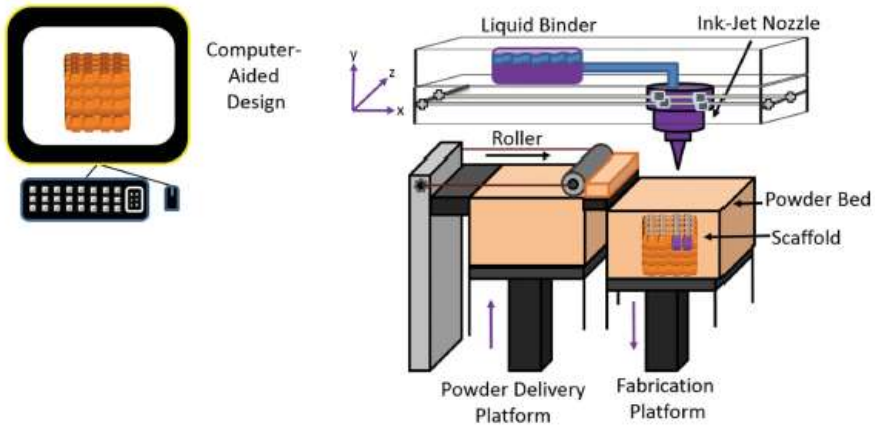

Figure 3.11 - *Schematic of a direct 3D printing set-up (Do, et al., 2015).*

The system described in Figure 3.11 represents one of the many of additive manufacturing. The apparatus showed consists of:

- a platform capable of moving up and down (90 degrees to the side to side motion);
- a liquid binder solution;
- a powder bed (plaster or resin);
- an Ink-Jet nozzle;
- a roller which deposits the powder layer;
- a powder delivery platform;
- a computer linked to the machine.

The process begins with the deposition of a powder bed that is spread onto the build platform and levelled using a roller system. The printer nozzle then extrudes the binder solution in the designated powdered areas directed by the CAD. Once the binder solution and powder are combined, the excess powder is removed (blown off). The build platform is then lowered, and a new powder layer is deposited and levelled. This procedure is then repeated until the final structure is produced.

In this thesis work a 3D-printing process has been performed by using a 3D-bioplotter. Bioplotter printing is a rapid manufacturing technique that employs a nozzle extrusion system of thermally or chemically treated materials.

As for the 3D-printing technique, the bioplotter machine is controlled by a computer. More precisely, a CAD (computer aided design) model is projected by specific software such as SolidWorks, AutoCAD or Blender. Then, the model is transferred with a .STL format to the program which commands the machine. Once all the parameters are set, the device prints the material by following the CAD model. Figure 3.12 shows a scheme of the 3D-Bioplotter apparatus (Do, et al., 2015).

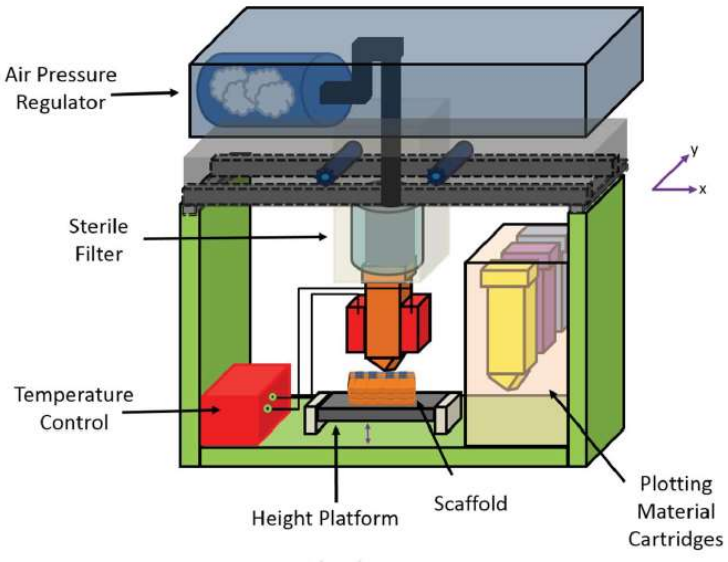

Figure 3.11 - *Schematic of a Bioplotter Printer set-up (Do, et al., 2015).*

The basic apparatus consists of:

- print heads with plotting material cartridges;
- an air pressure regulator;
- particle and sterile filters;
- a temperature control;
- a height platform.

The printer employs a pneumatic pressurized system to extrude the material from the cartridge through a needle tip.
The material is deposited layer by layer and the parameters such as print head temperature, deposition speed and extrusion pressure can be set manually by acting on the software.

This technology allows to print a wide range of materials like polymers, ceramics, metals and cell-laden hydrogels (Peltola, et al., 2008). The resolution is of the order of microns.

3.2.2 Process variables in 3D-Printing

The parameters that can influence the morphology and the sizes of scaffolds produced by 3D-Printing are classified as: material, printing platform, printing procedure and physical parameters (Table 3.2).

***Table 3.2** – Key factors affecting 3D-Printing (Waheed, et al., 2016).*

Material Parameters	**Printing platform Parameters**	**Printing procedure Parameters**	**Physical Parameters**
Viscosity Surface tension Particle size	Printing algorithms Printing procedure User interface	Printing speed Printing pressure Orientation Layer thickness Distance between tip and platform Print head temperature Needle size	Humidity Temperature

3.2.3 Hierarchical Integration of 3D-Printing and Electrospinning techniques

One of the main limitations of 3D-printing technique for tissue engineering applications is represented by its low-resolution limits, negatively affecting cell adhesion and tissue regeneration.

Indeed, the features of a scaffold such as roughness and topography, play a fundamental role in cell attachment, migration, proliferation, and differentiation, possibly due to cell–cell interactions occurring on that length scale (Giannitelli, et al., 2015; Holzapfel, et al., 2013).

However, the conventional methods, such as electrospinning technique, are characterized by imprecise control scaffold pore size, geometry, interconnectivity and low mechanical strength. Recently, some studies started to design hierarchical structures with pore sizes ranging from micro- to macro- scale, with anisotropic pore distribution and controlled geometry (Puppi, et al., 2014; Moroni, et al., 2008; Moroni, et al., 2013). These smart TE (tissue engineered) scaffolds are able to mimic the microenvironment of extracellular matrix through the nanofeatures and promote tissue ingrowth and vascularization through the micro-scale features. Vaquette et al. developed biphasic scaffolds for the regeneration of alveolar bone/periodontal ligament complex using 3D-printing and electrospinning techniques. The electrospun membrane acted as a soft support which constitutes the interface with the periodontal ligament fibroblast cells, while the 3D printed scaffold provided biomechanical stability (Vaquette, et al., 2012). Therefore, the combination of AM (additive manufacturing) with other conventional scaffolding technologies represent a promising strategy to fabricate biomimetic, multiscale and complex 3D structures.

Experimental Procedure

4 Electrospinning: Polymeric Nanofibers Production

In this work the electrospinning technique was used to produce poly(lactic acid) (PLA) and polycaprolactone (PCL) nanofibers with and without barium titanate nanoparticles (BTNPs). PLA and PCL are biodegradable, thermoplastic and aliphatic polymers that belong to the family of polyesters (Figure 4.1) (Farah, et al., 2016; Labet & Thielmans, 2009).

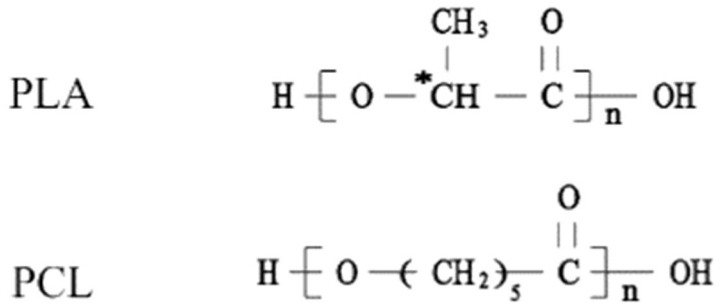

Figure 5.1 *– Chemical structures of poly(lactic acid) and polycaprolactone (Van de Velde & Kiekens, 2002).*

The main properties of these two polymers are summarised in Table 4.1.

Table 4.1 *– Physical properties of PLA and PCL (Farah, et al., 2016).*

Properties	Unit	PLA	PCL
Polymer density, ρ	g/cm^2	1.21-1.25	1.11-1.146
Tensile strength, σ	MPa	21-60	20.7-42
Tensile modulus, E	GPa	0.35-3.5	0.21-0.44
Ultimate strain, ε	%	2.5-6	300-1000
Specific tensile strength, σ^*	Nm/g	16.8-48.0	18.6-36.7
Specific tensile modulus, E^*	kNm/g	0.28-2.80	0.19-0.38
Glass transition temperature, T_g	°C	45-60	(-60)-(-65)
Melting temperature, T_m	°C	150-162	58-65

As shown in Table 4.1, PLA has higher density, tensile strength and tensile modulus than PCL that is, instead, less resistant to fatigue and more difficult to process by fiber spinning (Van de Velde & Kiekens, 2002). However, PCL shows values of elongation at break (ε) 150 times greater than those of PLA. Furthermore, the low melting point of PCL (59-64 °C) make it more thermally stable than PLA and allows to treat this material by reaching temperatures higher than melting temperature and avoiding phenomena of degradation (Hajiali, et al., 2017).

Barium Titanate ($BaTiO_3$) is a ceramic biocompatible material with piezoelectric and ferroelectric properties belonging to the family of perovskites (Burcu, 2013). The structure of cell unit depends on the temperature (Figure 4.2). Above the Curie temperature the elementary cell of $BaTiO_3$ is cubic and symmetric while below the Curie temperature it is slightly distorted and tetragonal. The stable structure is orthorhombic when the temperature is between 5 °C and -90 °C. Rhombohedral cell is stable below -90 °C (Vijatović, et al., 2008).

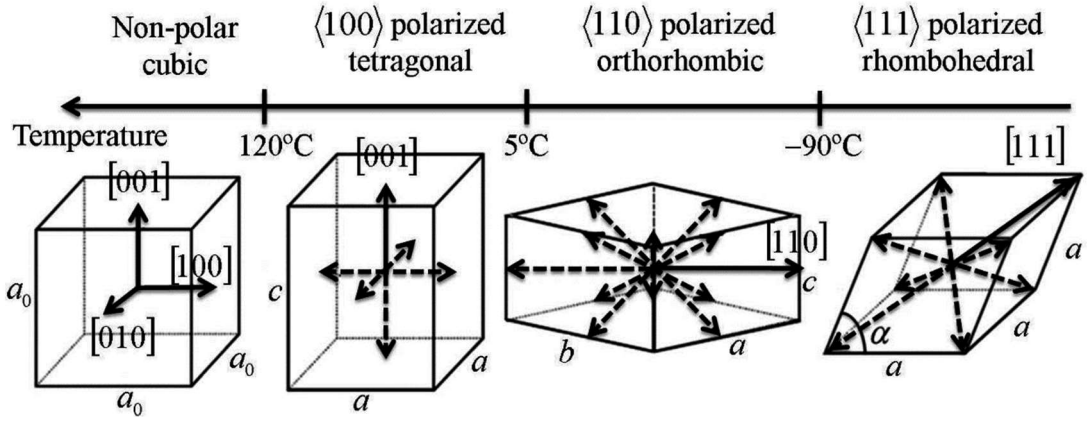

Figure 4.2 *– Phase transition of $BaTiO_3$ (Shu & Bhattacharya, 2001).*

The piezoelectric properties of this material are due to the high coupling coefficient indicating a good conversion efficiency when it is mechanically stressed. This ability is maintained at elevated temperatures because the Curie temperature of $BaTiO_3$ is relatively high (T_c=130°C) (Vijatović, et al., 2008). In this work tetragonal barium titanate nanoparticles with 300 nm size have been used.

4.1 Preparation of PCL and PLA solutions

Polycaprolactone (PCL, Mw = 80000 Da), Dichloromethane (DCM) and methanol were used to prepare PCL solutions. Initially PCL and DCM were mixed together with % mass/volume ratio (% w/v) of 14%, 12%, 10% and 6% by solubilization of the polymer in DCM, under magnetic stirring at room temperature (Figure 4.3). Other PCL solutions were prepared by adding methanol with volume ratio 7:3 (DCM:methanol) and polymer concentrations of 14%, 13%, 10%, 8%.

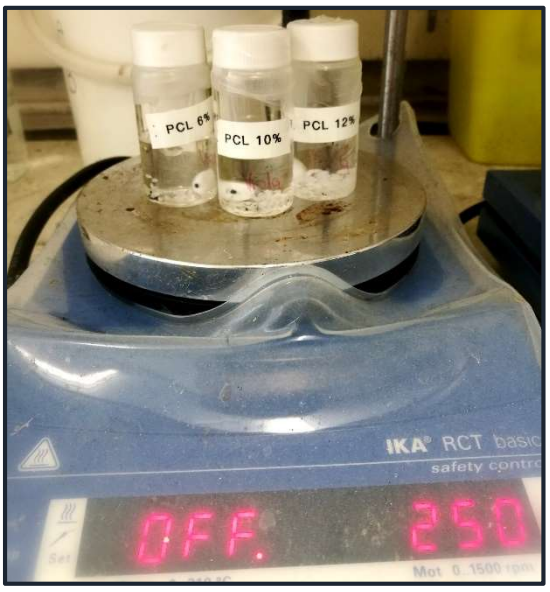

Figure 4.3 *– Solutions of PCL and DCM were mixed under magnetic stirring (250 rpm) at room temperature overnight.*

Poly(lactic acid) (PLA, Mw = 4060 Da) based solutions were formulated by mixing together the polymer and acetone with a % mass/volume ratio (% w/v) of 14%. The various prepared solutions (S) are listed in Table 4.2.

Table 4.2 – *Compositions (% w/v) of PCL and PLA based solutions.*

Solutions	**PCL% (w/v)**	**PLA% (w/v)**	**Solvent**
S1	14	0	DCM
S2	14	0	DCM:methanol (7:3)
S3	13	0	DCM:methanol (7:3)
S4	12	0	DCM
S5	10	0	DCM
S6	10	0	DCM:methanol (7:3)
S7	8	0	DCM:methanol (7:3)
S8	6	0	DCM
S9	0	14	Acetone

4.2 Preparation of PCL/BTNPs and PLA/BTNPs dispersions

Once PCL and PLA solutions were optimized in terms of polymer concentration and solvent type, barium titanate nanoparticles (BTNPs) were added. PCL/BTNPs and PLA/BTNPs dispersions were prepared by adding various concentrations (mg/ml of polymer solution) of barium titanate nanoparticles. These were mixed with 10 % (w/v) PCL and DCM:methanol (7:3) and with 14 % (w/v) PLA and acetone.

The particles were added only after the polymer was completely solubilized in order to obtain a homogeneous distribution by avoiding the formation of aggregates. The solutions were maintained under magnetic stirring at room temperature overnight. The various prepared dispersions (P) are listed in Table 4.3.

Table 4.3 - *Compositions (% w/v) of PCL, PLA and (mg/ml) BTNPs based dispersions.*

Dispersions	**PCL% (w/v)**	**PLA% (w/v)**	**Solvent**	**BTNPs (mg/ml)**
P1	10	0	DCM:methanol (7:3)	10
P2	10	0	DCM:methanol (7:3)	30
P3	10	0	DCM:methanol (7:3)	50
P4	10	0	DCM:methanol (7:3)	100
P5	10	0	DCM:methanol (7:3)	150
P6	10	0	DCM:methanol (7:3)	200
P7	10	0	DCM:methanol (7:3)	250
P8	0	14	Acetone	10
P9	0	14	Acetone	30
P10	0	14	Acetone	50
P11	0	14	Acetone	100

4.3 Electrospinning Process

Electrospun fibers were obtained by vertical electrospinning using the Spraybase Electrospinning Kit (Figure 4.4).

Figure 4.4 - *Spraybase Electrospinning Kit used for fibers fabrication.*

It is constituted of:

- a high voltage power supply with a single voltage output up to 20 kV (positive);
- a syringe pump (infusion rate of 0.75 µl/hr to a maximum 2100 ml/hr);
- a software-controlled syringe pump to deliver the solution to the emitter tip (maximum syringe size is 60 cc);
- a 18 G x 25 mm stainless steel single needle and a plastic tube (internal diameter 1.0 mm) that links the syringe to the needle;
- a grounded plate for collecting fibers;
- a Z axis and manual manipulator to control the position of the needle relative to the collector plate;
- a camera and lens with visualization software capable of viewing and recording the Taylor cone;
- a safety hood that has an interlock to cut off the voltage once the door is opened, ensuring the safety of the end user.

The operating conditions of spinning, such as voltage, flow rate and needle-collector distance, were modulated according to the characteristics of the polymer solutions.

These parameters were optimized in order to obtain a continuous jet that could originate fibers without beads. The various tests are listed in Table 4.4. The process was carried out at atmospheric pressure, maintaining temperature and relative humidity (RH) within a set interval (27-33 ° C, 20-30% RH).

Table 4.4 - *Electrospinning conditions of PCL, PLA, PCL/BTNPs and PLA/BTNPs based formulations.*

Solutions	**Distance (cm)**	**Voltage (kV)**	**Flow rate (ml/hr)**
S1	15	15	0,3
S2	10	18	1
S3	10	15	1
S4	15	12	0,8
S5	15	10	0.8
S6	11	10	2.5
S7	15	18	0.4
S8	15	18	0.7
S9	15	10	0.7
P1	11	15	1.5
P2	11	15	1.5
P3	11	15	1.5
P4	11	15	1.5
P5	11	15	1.5
P6	11	15	1.5
P7	11	15	1.5
P8	15	10	0.7
P9	15	10	0.7
P10	15	10	0.7
P11	15	15	1

5 3D-Bioplotter: PCL Scaffolds Fabrication

In this work the bio-plotting technique was used to produce polycaprolactone (PCL) scaffolds with and without barium titanate nanoparticles. Several sample thicknesses, porosities and geometries were tested to obtain optimized scaffolds for skin regeneration. Low and high temperature processes were performed to produce piezoelectric and non-piezoelectric scaffolds, respectively. Indeed, to print scaffolds with homogenously distributed BTNPs, a solution of PCL and consequently a low temperature process are needed.

3D-Bioplotter System used in this work is shown in Figure 4.5.

Figure 4.5 *- 3D-Bioplotter® Developer Series (Envisiontec) used for fabricating PCL scaffolds.*

It is constituted of:

- one low-temperature print head (0 °C – 70 °C) with disposable polyethylene cartridges;
- one high-temperature print head (30 °C – 250 °C) with reusable stainless steel cartridges;
- plastic or stainless steel needle tips with 0.1 mm to 1.0 mm internal diameter;
- needle cleaning station with automatic cleaning before and during the print;
- air pressure regulator, particle and sterile filters, a temperature control, a camera, a needle sensor;
- a height platform which can be heated.

The minimum strand diameter is 0.1 mm and it depends on the needle size used, the distance between the needle and the platform (z-offset) and the target material.
The print head speed can be set to a value between 0.1 and 150 mm/s while the pressure ranges from 0.1 bar to 9.0 bar. This machine has an axis resolution (XYZ) of 1 μm.
3D-Bioplotter is connected to a computer with two software: Bioplotter RP® and VisualMachines. The first can modify and design simple CAD models. Successively it converts the models to .STL files, a format that can be processed by the machine. To design complex structures other software, such as SolidWorks, are used.
VisualMachines is the software used to control the Bioplotter, by tuning several parameters and by setting the optimal condition to obtain the desired structure. Indeed, this software acts on needle calibration, needle z-offset, pressure and speed parameters, pattern design, temperature and other settings.

5.1 High temperature 3D-printing process

In order to develop non-piezoelectric PCL scaffolds, a high temperature 3D-printing process was performed. Initially, a box 30x30 mm^2 was designed by using Bioplotter RP® (Figure 5.1). The thickness of each layer was set at 150 μm.

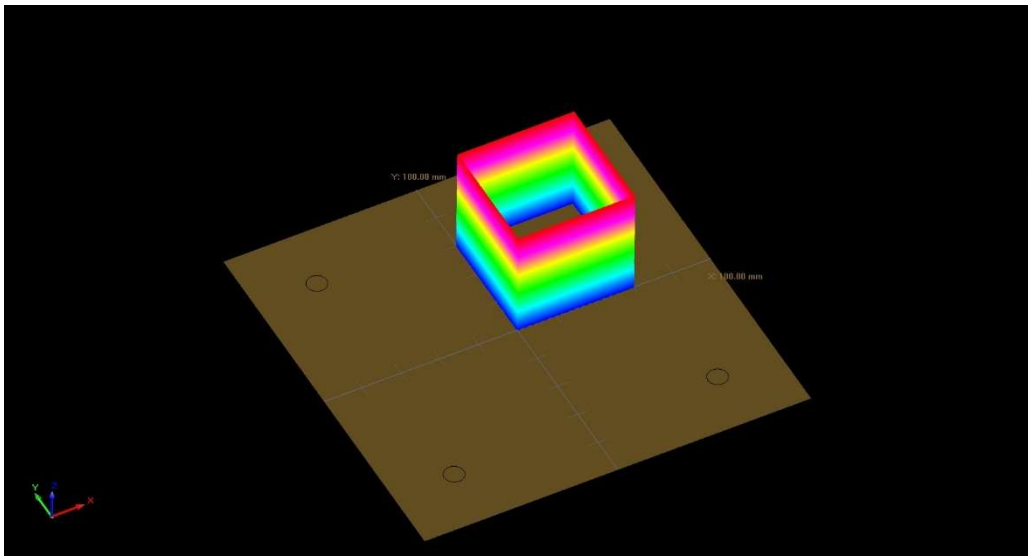

Figure 5.1 *– The geometry, the thickness and the number of layer were set by using Bioplotter RP®.*

Then, Polycaprolactone (PCL, Mw = 45000 Da) was added into the stainless-steel cartridge and the temperature of the print head was set at 160 °C.

Once the temperature was reached and the needle calibration was performed, the material parameters were chosen by manually tuning pressure, speed and z-offset. Figure 5.2 shows the values that were chosen to print non-piezoelectric scaffolds. The optimisation of these physical quantities is critical because they depend on the material characteristics like viscosity, on the temperature and on the needle size. For this process a steel needle with 0.3 mm inner diameter was used.

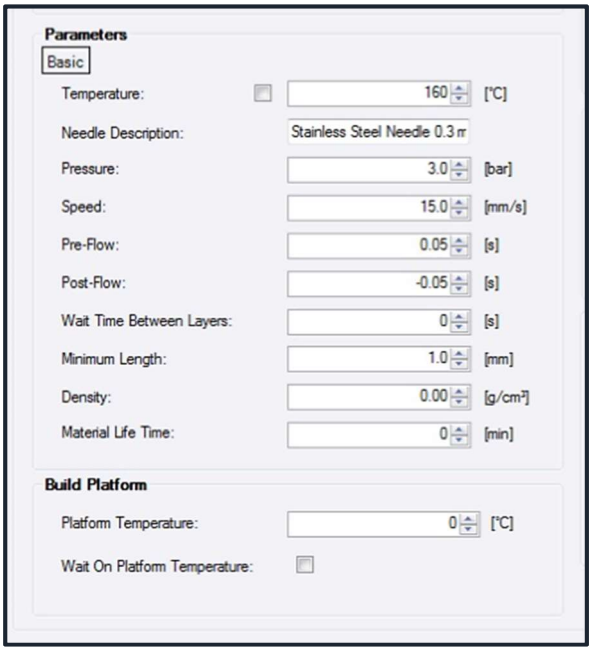

Figure 5.2 *– Material parameters were set in the "Programming" section.*

A linear pattern with a distance between strands of 0.90 mm was chosen, while a 90 °C rotation of lines between one layer and another was set (Figure 5.3). The distance between strands determines the porosity size of the final scaffold.

Several thicknesses were tested, by varying the number of layers of each scaffold. Three layers and consequently a thickness of 450 µm were found to be the best combination.

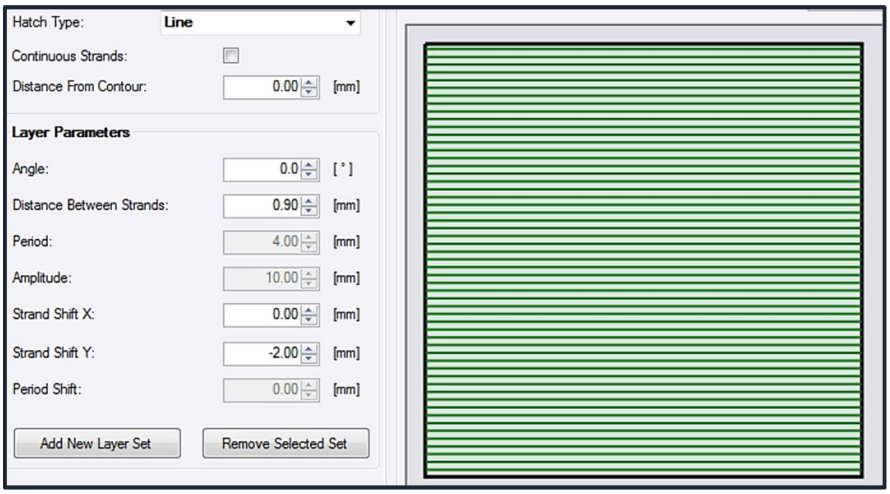

Figure 5.3 - *A linear structure was set in the "Pattern Designer" section in order to print a PCL mesh.*

5.2 Preparation of PCL/BTNPs dispersions

To fabricate piezoelectric wound dressings, dispersions of barium titanate nanoparticles (BTNPs) in polycaprolactone (PCL, Mw = 45000 Da) and acetone were prepared. The solvent is needed to obtain a homogeneous dispersion of particles within the structure and to avoid the formation of agglomerates. Initially 500 mg/ml BTNPs and acetone were mixed together under magnetic stirring at 50.5 °C in an oil-water bath. Once the particles were uniformly dispersed in the solvent, PCL was slowly added and the solution was maintained under a strong magnetic stirring (1500 rpm) and in the heated (45°C) oil-water bath overnight. The content of piezoelectric nanoparticles was preserved at 500 mg/ml, while the concentration % of PCL was varied in order to optimize the viscosity and consequently promote the printing process.

The various % mass/mass ratio (% w/w) that were formulated are listed in Table 5.1.

Table 5.1 - *Compositions (% w/w) of PCL and (mg/ml) BTNPs based dispersions.*

Solutions	**PCL% (w/v)**	**Solvent**	**BTNPs (mg/ml)**
D1	60	Acetone	500
D2	50	Acetone	500
D3	40	Acetone	500
D4	30	Acetone	500

5.3 Low temperature 3D-printing process

The presence of acetone, an inflammable solvent with a boiling point at 60 °C, imposes the use of low temperatures during the print process. The PCL/BTNPs dispersion was added into the polyethylene cartridge and the temperature was set at 40 °C, after several temperature tests. Before starting the procedure, the needle and camera calibrations were performed (Figure 5.4).

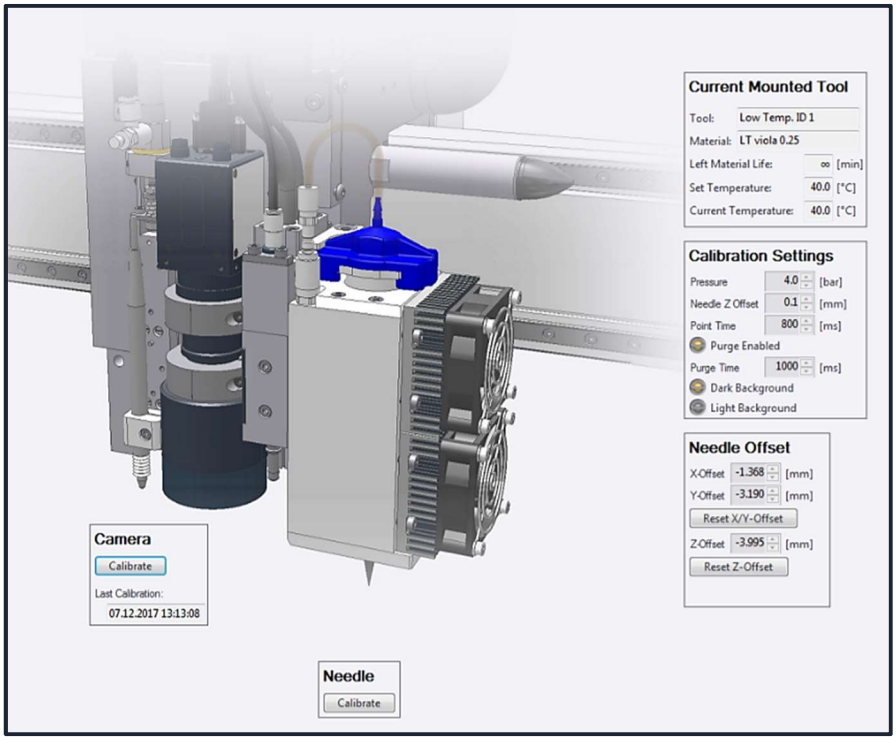

Figure 5.4 *– Camera and needle calibration.*

The analogous cubic CAD model of non-piezoelectric scaffolds was also used to fabricate the piezoelectric dressings. Three different needle sizes (0.25 mm, 0.44 mm and 0.33 mm) were used and several tests were performed to optimize the pressure, speed and z-offset. The goal was to find the setting that would allow to obtain a filament of continuous material, without bubbles or agglomerations of particles in order to obtain a defect-free structure. The optimized parameters are shown in Figure 5.5.

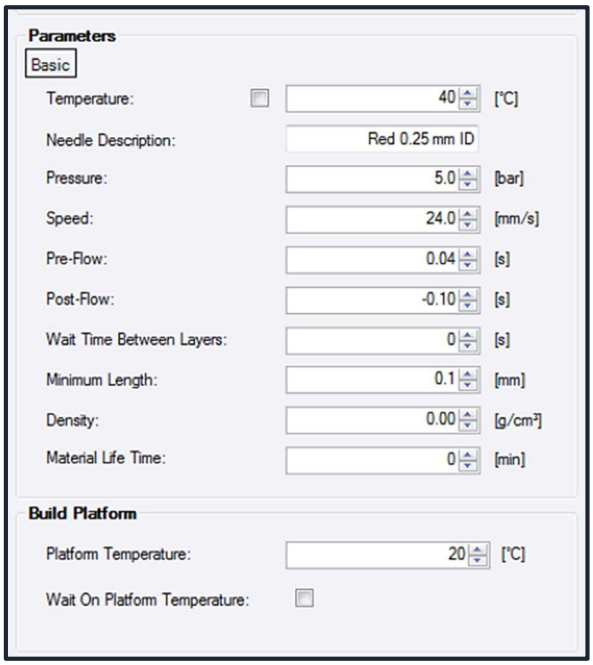

Figure 5.5 *–Material parameters were set in the "Programming" section.*

The mesh pattern was maintained, but the distance between strands was increased at 1.10 mm. However, the porosity size is 0.5 mm, resulting inferior respect to the non-piezoelectric PCL scaffold. Indeed, the width of piezoelectric single strand was larger than that of non-piezoelectric strand. The use of a steel needle with an inner diameter of 0.33 mm allowed to obtain a continuous strand, while the plastic needle with the internal diameter of 0.25 mm provoked the formation of disconnected filaments. Three layers is the number of layers that has allowed to obtain an optimized thickness.

5.4 Fabrication of Composite Scaffolds

The strategy that was adopted to fabricate the composite wound dressings consists in the direct fibers electrospinning on the surface of 3D-printed scaffolds. To this aim, PCL printed scaffolds with 500 mg/ml of barium titanate piezoelectric nanoparticles were immobilised on the aluminium foil which was placed on the metal collector with adhesive conductive tape (Figure 5.6).

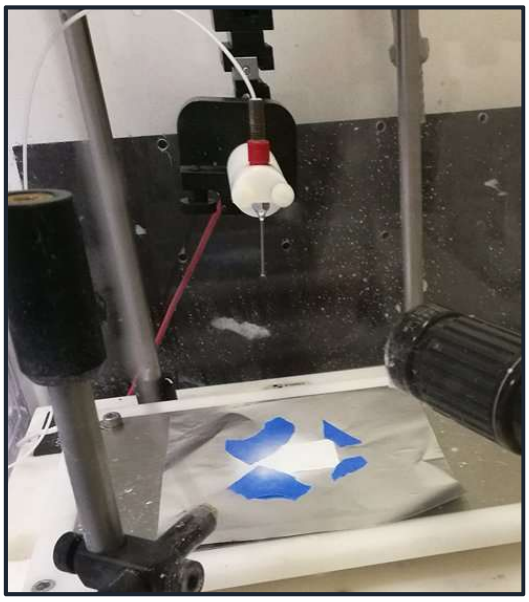

***Figure 5.6** – Fabrication of composite scaffolds.*

P5 and P7 solutions, with 150 mg/ml and 250 mg/ml particles concentration were electrospun by using a voltage of 10 kV, a flow rate of 1.5 ml/hr and a distance of 11 cm. Figure 5.7 shows the scaffold before and after the electrospinning process.

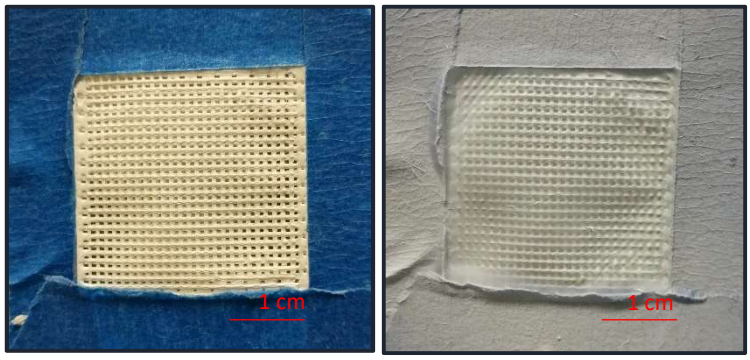

***Figure 5.7** – 3D-printed scaffold before and after being subjected to the electrospinning process.*

Polycaprolactone has been chosen to fabricate the composite wound dressings for the better mechanical properties respect those of poly(lactic acid). This aspect will be discussed in Chapter 8. The composites have been realised with two different contents of piezoelectric particles in order to evaluate the possible effects on cells due to the BTNPs concentration.

6 Characterization of Nanofibrous mats, 3D-printed scaffolds and Composite Wound Dressings

The nanofibrous mats and the 3D-printed constructs were characterized by investigating their surface properties and the cytocompatibility. For the morphological analysis, scanning electron microscopy (SEM), scanning and transmission electron microscopy (STEM) and optical microscopy were carried out. To evaluate the versatility of wound dressings and the cellular adhesion on the substrates, an *in vitro* study was performed. The nanocomposites were also characterized by investigating the cellular response to piezoelectric scaffold. Fibroblasts on the substrates were stimulated with ultrasounds and their calcium activity was simultaneously monitored.

6.1 Scanning electron microscopy (SEM) for nanofibers surface characterization

The morphological analysis of the fibers was carried out using a scanning electron microscope (Scanning Electron Microscope, SEM), with a beam of focused primary electrons as radiation source. The primary electron beam, by interacting with the atoms of the sample, determines the emission of a secondary electron beam. This is collected by a detector and converted into a black and white image with high resolution and great depth of field. The electron source of a scanning electron microscope is generally a tungsten filament. Prior to imaging, a surface treatment was performed on the samples. Indeed, all non-metals samples need to be made conductive to avoid charge effects that could cause image distortion or drift during SEM acquisition. For this reason, the samples were immobilised on a metal stub with adhesive conductive tape and covered with a thin layer of conductive material by gold sputtering the surface (Figure 6.1).

The coating was performed by the deposition of particles that were removed from a solid target when it is bombarded with energetic and heavy ions coming from a plasma, for instance argon. In this work samples were made conductive by vacuum-phase vapor deposition by using Quorum Q150R-S sputter with a current of 20 mA, time 90 s and material Au/Pd (80:20).

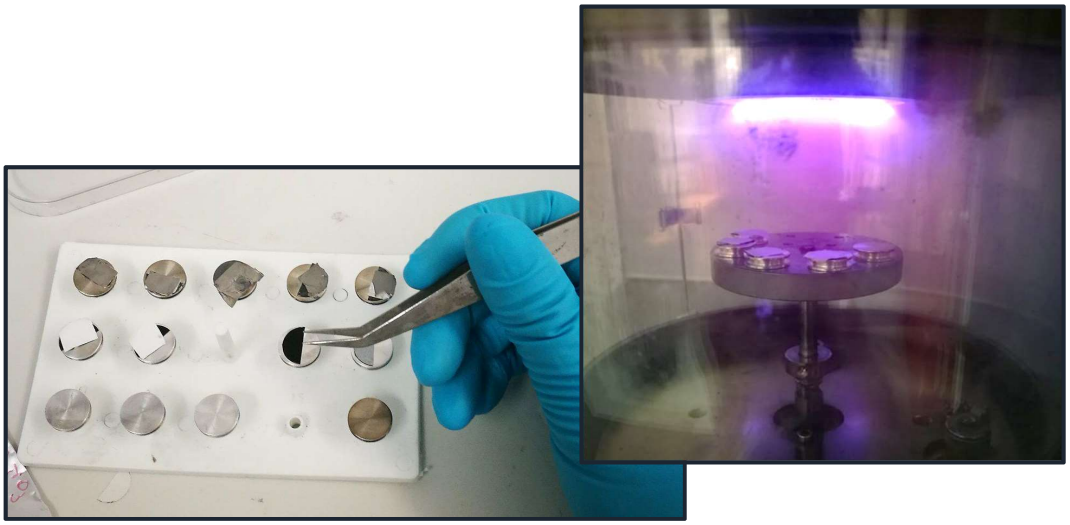

Figure 6.1 *– The samples were prepared to be gold sputtered by using an argon plasma.*

The surface characterization of PCL, PLA, PCL/BTNPs and PLA/BTNPs nanofibers was performed by using a ZEISS GeminiSEM 450 microscope (Carl Zeiss, Oberkochen, Germania) at the Material Engineering Department of Loughborough University. The analyses were implemented with voltages of 5-7 kV, under vacuum conditions, at room temperature and by trying various magnifications. Part of the SEM images was acquired using a JSM-7800F Schottky Field (Jeol, USA) emission scanning electron microscope. The surface morphology of PLA and PCL nanofibers with different BTNPs concentrations was analysed and images were obtained with 2000X, 5000X, 10000X and 20000X magnifications.

6.2 Scanning and transmission electron microscopy (STEM) of nanofibers

Scanning transmission electron microscopy (STEM) represents a combination of the principles of transmission electron microscopy (TEM) and scanning electron microscopy (SEM). As with the TEM, imaging is formed through an electron beam transmitted by the sample and consequently requires very small sample thicknesses. Like SEM, this instrument can detect the scattered electrons, whose intensity is traced according to the position of the electronic probe. The advantages of STEM are the capability to use signals that can not be spatially correlated in TEM and a better spatial resolution compared to SEM.

In this thesis work the Helios NanoLab^{TM} 600i (FEI, Thermo Fisher Scientific) scanning and transmission electron microscope was used to better analyse PCL/BTNPs nanofibers with 100 mg/ml, 150 mg/ml, 200 mg/ml and 250 mg/ml $BaTiO_3$ concentrations. To obtain the images a voltage of 25 kV, a current of 43 pA, and a DF/HAADF mode were set.
The instrument was made available by the Italian Institute of Technology (IIT) in Pontedera.

6.3 Optical microscopy analysis of printed scaffolds and composites

The imaging of 3D-printed piezoelectric scaffolds was performed by using a Leica DMi8 inverted optical microscope (Figure 6.2) at the Material Engineering Department of Loughborough University.

***Figure 7.2** – The inverted optical microscope used for 3D-printed piezoelectric scaffold imaging.*

An inverted microscope, unlike the traditional microscope, presents the eyepieces below the stage pointing up, oriented toward the lower face of the sample. This instrument allows to observe from the bottom the scaffolds that are flattened on the superior surface.

On the obtained images an analysis of the porosity perimeter and area was also performed by using the software ImageJ.

The imaging of all printed scaffolds and composites was performed at the Italian Institute of Technology (IIT) in Pontedera, by using the Nikon Eclipse Ti inverted optical microscope and the NIS-Elements Advanced Research software.

6.4 Biological characterization

In vitro studies were performed to analyse the cell proliferative capability and the cellular response to the piezoelectric substrates. NIH 3T3 fibroblasts were cultured on PCL, PCL/BTNPs scaffolds and cell proliferation was evaluated after 24 h and 72 h with WST-1 assay (K301-500, BioVision) and alamarBlue assay (DAL1025, Invitrogen). The biological characterization of substrates, which is described below with reference to fibroblasts, was performed using also SaOS-2 cells to evaluate the versatility of scaffolds. This cell line derives from a primary osteosarcoma and displays several osteoblastic features.

6.4.1 Culture system preparation

PCL and PCL/BTNPs substrates were prepared as described in Chapters 4-5. In additions Thermanox^{TM} Coverslips (174934) were used as control substrate. They are conventionally used as control substrates for cell culture tests due to their non-cytotoxicity, high transparency, stiffness and resistance to solvents. In order to perform biological experiments, samples were cut into 0.5 mm side squares to adapt their size to the area of each well. Because cellular adhesion is favored on hydrophilic surfaces (Abedalwafa, et al., 2013) and polycaprolactone is hydrophobic, an additional surface modification of the substrates was required. Plasma-surface modification is an effective and economical surface treatment technique that can improve adhesion strength and biocompatibility and can be easily scaled up to industrial production (Chu, et al., 2002). Plasma is an electrically neutral medium that consists of positive and negative charged ions and neutral elements such as atoms, molecules and radicals. When an atom or a molecule gains enough energy from an outside excitation source or via interaction (collisions) with one another, ionization occurs. Generally, to produce plasma a gas is heated or it is subjected to a strong electromagnetic field that ionize a fraction of atoms. Plasma implantation introduces polar functional groups that modify the surface properties of material making it more hydrophilic. Formation of oxygen functionalities by ion implantation is one of the most useful and effective processes of surface modification (Chu, et al., 2002). In this work the samples were exposed to O_2 plasma obtained in a TUCANO Gambetti plasma reactor (Figure 6.3).

Figure 6.3 – *TUCANO Gambetti plasma reactor system used for surface modification of substrates (Gambetti, 2016).*

It is a reactor in configuration with flat and parallel electrodes, in which the upper electrode is polarized by a radio frequency power generator while the lower electrode is connected to the ground. A special tray allows to load manually the samples into the process chamber which is made of aluminum. The system uses power signals with RF frequency (13.56 MHz) to generate the plasma inside its process chamber (Gambetti, 2016). Figure 6.4 shows a schematic diagram of a plasma reactor (Ratner, et al., 1996).

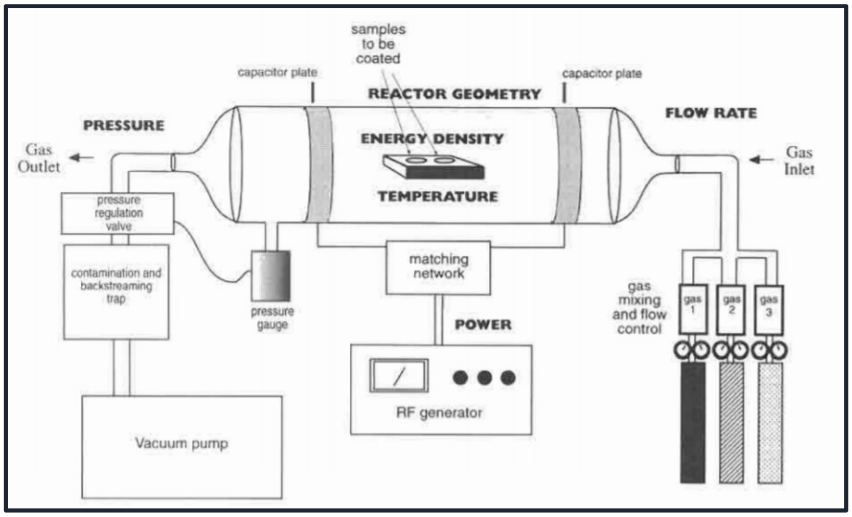

Figure 6.4 – *A diagram of a typical inductively coupled RF plasma reactor (Ratner, et al., 1996).*

The treatment was performed with the following conditions: 60W power, 10^{-1} mbar pressure, 50 sccm flow and 30 s plasma time.

In order to fabricate *ad hoc* prepared multi-well plate in polydimethylsiloxane (PDMS) for cell seeding, PDMS (Sylgard 184) was prepared by mixing base and curing agent at ratio 20:1 (w/w). Then, it was exposed to vacuum to obtain its degassing. By using the laser cutting (UNIVERSAL Laser System) and the software CoreIDRAW, 0.7x0.7x0.6 cm^3 plexiglass molds were fabricated (Figure 6.5).

Figure 6.5 *– Laser cutting used for fabrication of plexiglass molds (https://www.ulsinc.com).*

The mods were then positioned on the previously deposited silicon layer and they were coated with 30 g of PDMS. Once the cross-linking in the oven has taken place for about two hours at 60 °C, *ad hoc* prepared multi-well plate was obtained (Figure 6.6).

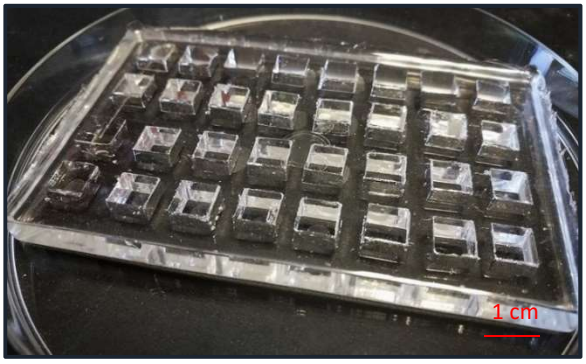

Figure 6.6 - *Ad hoc prepared multi-well PDMS plate with 24 wells used for cell seeding.*

Sterilization of samples was performed by using ultraviolet (UV) light for 20 minutes.

6.4.2 Cell culture

Cell culture is the technique in which cells of different organism are maintained in a fluid medium with proper conditions of temperature, pH, humidity and nutrition. This favourable artificial environment allows the growing of cells and typically it is represented by suitable glass or plastic culture vessels containing a liquid or semisolid medium that supply nutrients to cells (Lynn, 2009). Cell culturing is an effective technique to study the physiology and biochemistry of a specific cell line and to indagate the effects of drugs and toxic agents.

Two main type of cultures exist: primary (mortal) cultures and continuous (immortal) cell lines. Primary cells are isolated directly from human or animal tissue using enzymatic or mechanical methods. They can be classified as adherent or suspension cells. Adherent cells require attachment for growth and are said to be anchorage-dependent cells. They are usually derived from tissues of organs, while suspension cells do not require attachment for growth and are said to be anchorage-independent cells. All suspension cells are isolated from blood system.

Primary cells can expand for only 50 to 100 generations after which senescence occurs. On the contrary, the continuous cell lines can divide indefinitely and they generally derive from tumour tissue or from modified primary cells (Philippeos, et al., 2012). In this project the *in vitro* test has been used to characterize PCL substrates from the biological point of view and to analyse the piezoelectric effects of BTNPs on cells. The NIH 3T3 cells line are mouse embryonic fibroblast anchorage-dependent cells. They were initiated from a cell line isolated in 1962 at the New York University School of Medicine Department of Pathology (Leibiger, et al., 2013).

In this work NIH 3T3 cells (ATCC® CRL-1658™) were cultured in plastic flasks of 75 cm^2 (T-75 flask) in proliferation conditions: Dulbecco's Modified Eagle's Medium (DMEM, Gibco) high glucose, supplemented with 10% fetal bovine serum (FBS, Gibco), 2 mM L-glutamine (Gibco), 1 mM sodium pyruvate (Gibco), 2.5 µg/ml amphoterycin B (Sigma Aldrich, Saint Louis, MO), and 100 U/ml penicillin-100 µg/ml streptomycin (Gibco). Cells were maintained at 37 °C with 5% CO_2 at saturated humidity that are proper conditions for human cells growth. DMEM (Dulbecco's Modified Eagle Medium) is a widely used basal medium for supporting the growth of many different mammalian cells, such as primary fibroblasts, neurons and glial cells. It contains glucose, in low or high concentrations, that is the main energy source for cellular metabolism.

DMEM uses a sodium bicarbonate buffer system (3.7 g/L), and therefore requires a 5–10% CO_2 environment to maintain physiological pH. It also incorporates phenol red, a pH indicator that allows constant monitoring of pH which changes as consequence of the metabolic activity of cells (Esumi, et al., 2002; Wyszynski, et al., 2002). FBS is the commonly used animal serum and it consists of embryonic growth promoting factors, hormones, vitamins and inorganic minerals (Mitry & Hughes, 2012). The antibiotics were used to avoid bacterial contamination of cell cultures by acting against both gram-positive and gram-negative bacteria (Philippeos, et al., 2012). Amphoterycin B is an antifungal drug that prevents mold contamination and fungal infections. All the biological procedures, such as the preparation of culture medium, were conducted in a laminar flow hood that is designed to provide a barrier against bacteria. It protects the user and the environment from inhaling toxic gases and prevents contamination of experiment from dust and microorganisms. All items placed in the hood were disinfected with ethanol 70% or sterilized with autoclave, in order to maintain the environment sterile.

6.4.3 Cell seeding

NIH 3T3 fibroblasts progressive grow in an undifferentiated state until they reach the almost confluence which is the state in which the available space is covered due to cellular expansion. If the medium and other conditions are satisfactory, then the cell line may progress through several serial subcultures.

Fibroblasts generally achieve around 50-60 population doublings before entering senescence (McKeehan, et al., 1977). Senescent cells no longer proliferate and after some months cells death occurs (Figure 6.7).

For this reason, to keep the culture at an optimal density and to continue growth and proliferation, the culture has to be divided and fresh medium is needed. In this work the cell splitting or passaging was performed using 0.05% trypsin, a proteolytic enzyme that binds to specific amino acid sequences in intercellular and cell-to-substrate proteins connections and cut them by detaching cells from the surface (Nelson, et al., 2008).

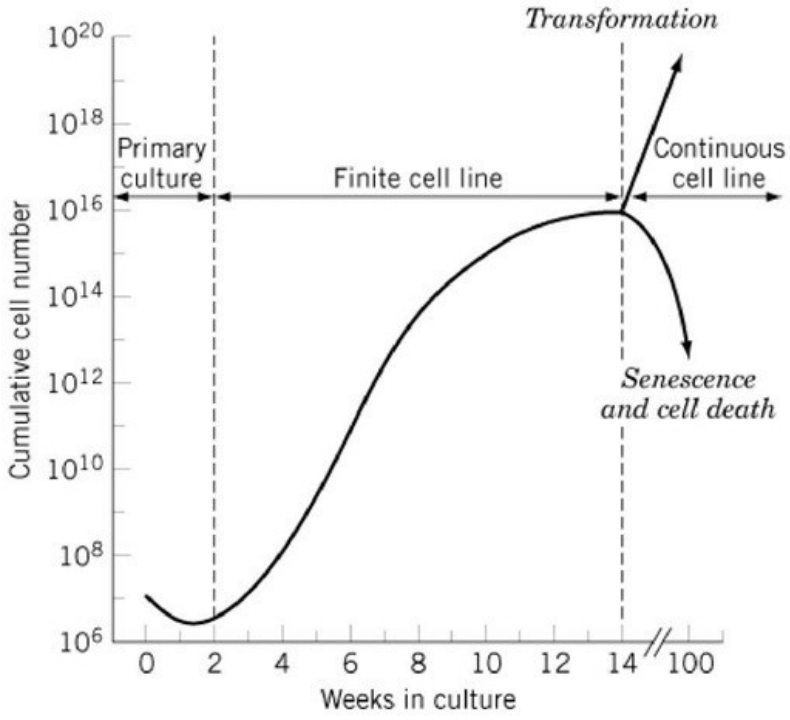

Figure 6.7 - *The curve shows the exponential growth during the replicative phase following by the growth arrest and senescence. If the finite cell line is transformed into the continuous cell line, the proliferation continues (McKeehan, et al., 1977).*

The protocol adopted for this procedure is as follows:

- **<u>Protocol 1</u>**: Cell splitting
  - Removal of the culture medium from the flask;
  - Rinse of cells with Dulbecco's phosphate-buffered saline (DPBS, Gibco) without Ca^{2+} and Mg^{2+} (10 ml) to remove any trace of serum that could influence the action of trypsin;
  - Removal of the rinse and addition of 2 ml of trypsin (prewarmed at 37 °C) in the flask;
  - Incubation of the flask at 37 °C for 2-3 minutes for allowing the trypsin to work;
  - Observation of cell morphology at the microscope: rounded cells suggest detachment from the surface;
  - Addition of the growth medium in the flask to block the action of trypsin;
  - Aspiration of the cell suspension and placement in a tube;

- Centrifugation at 2500 rpm for 5 minutes (the gravity acceleration corresponds to 700 g): the solid phase represented by cells (pellet) is deposited at the tube bottom;
- Aspiration of the supernatant fluid and re-suspension of pellet in a fresh media by repeatedly gently pipetting on the bottom of the tube.

After this procedure cells were observed at optical microscopy and they were counted using the Burker chamber (Optik Labor). It is a thick glass slide with a rectangular indentation that represents a chamber of known size (Figure 6.8 (a)). A 10 µL drop of cell suspension is poured into the chamber and covered by cover glass. Cells are counted in a square grid engraved on the bottom of the chamber (Figure 6.8 (b)).

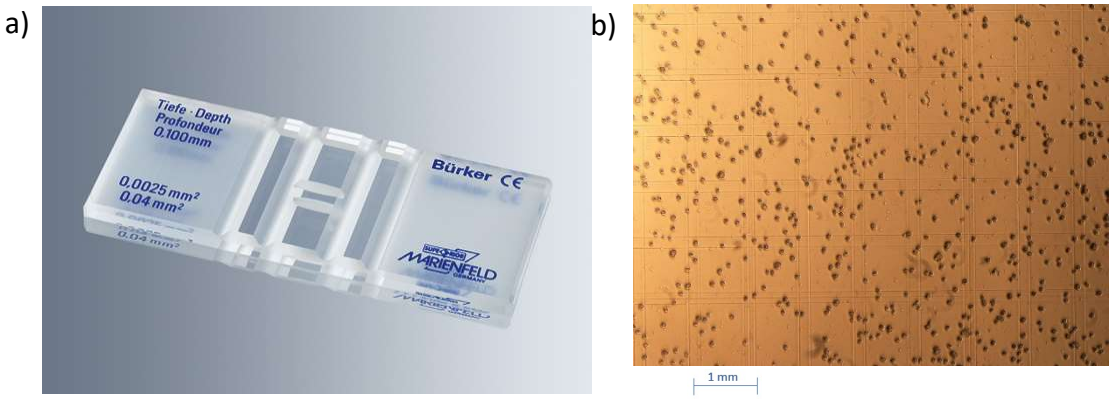

Figure 6.8 - *Burker chamber (Optik Labor) used like counting chamber a) and a microscope image of the grid where the cells are counted b).*

The number of cells is used to calculate the appropriate volume of cellular suspension for seeding. The resulting number of cells was approximately 2150000 cells/ml. A cellular density of 5000 cell/cm^2, a culture area of 0.6x0.6 cm^2 and 72 wells were considered to calculate the desired number of cells for the seeding:

$$0.6 \times 0.6\ (cm^2) \times 5000\ \left(\frac{cell}{cm^2}\right) \times 72 = 129600\ cells$$

To obtain the volume of cell suspension that correspond to this number of cells the following mathematical proportion has been set:

$$\frac{2150000}{ml} = \frac{129600}{x} => x = 60.3\ \mu L$$

This volume has been placed in two 24 well plates previously prepared with substrates (Figure 6.9).

For the seeding Dulbecco's Modified Eagle Medium (DMEM, Gibco) was used, supplemented with 10 % fetal bovine serum (FBF, Gibco), penicillin/streptomycin (100 U/ml, Gibco) andamphotericin B (2.5 µg/ml, Sigma Aldrich). After seeding the cells were placed into the incubator at 37 °C in a 5% CO_2 humidity saturated atmosphere. Cell culture medium was changed every two days.

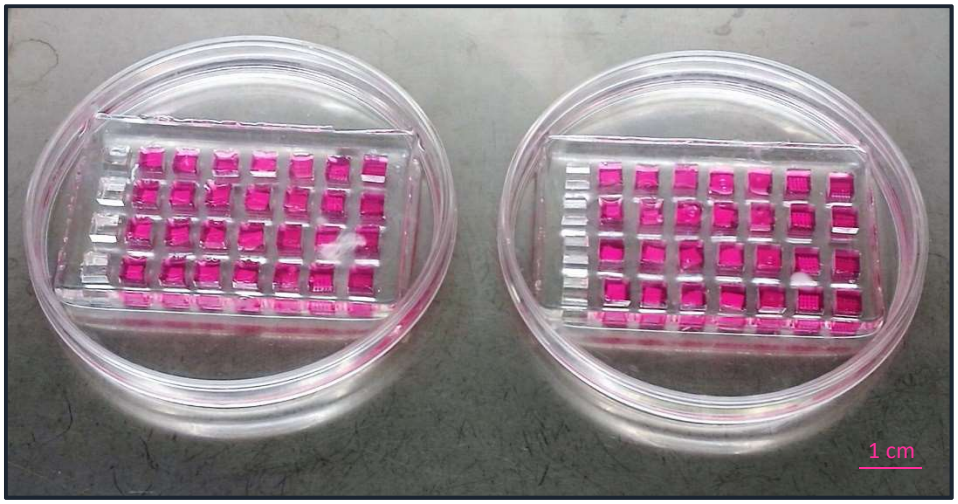

Figure 6.9 *– Cell seeding in 24 wells containing the tested substrates.*

As a consequence of the results obtained from the WST-1 assay, this cell seeding procedure was repeated by considering a cellular density of 10000 cell/cm^2.

6.4.4 Cell proliferation analysis: WST-1 and alamarBlue assays

The adhesion and the proliferation of cells were evaluated respectively after 24h and 72h from seeding through a procedure that analyses the metabolic activity of succinate dehydrogenase (SDH). It is a complex enzyme, found in many bacterial cells and in the inner mitochondrial membrane of eukaryotes. SDH is the only enzyme that participates in both the citric acid cycle and the electron transport chain (Oyedotun & Lemire, 2004). The WST-1 tetrazolium salt is cut by SDH into a soluble compound called formazan through a cellular mechanism (Figure 6.10).

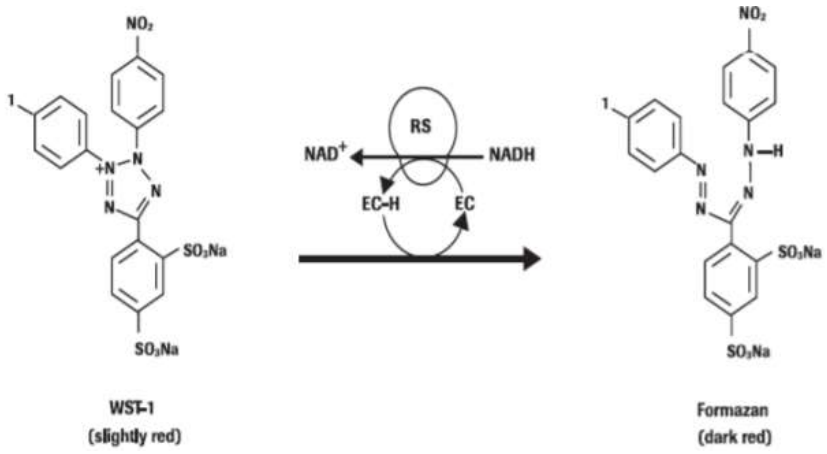

Figure 6.10 – *Cleavage of the tetrazolium salt WST-1(4-[3-(4-Iodophenyl)-2-(4-nitro-phenyl)-2H-5-tetrazolio]-1,3-benzene disulfonate) to formazan (Comby, et al., 2007).*

(EC = electron coupling reagent; RS = mitochondrial succinate-tetrazolium-reductase system)

This bio-reduction requires the presence of NADH (nicotinamide adenine dinucleotide) produced by living cells. Thus, the amount of formazan that is formed in the culture medium is proportional to the number of metabolically active cells in culture (Comby, et al., 2007). To measure the quantity of formazan in cellular medium, the absorbance is detected by a spectrophotometer. Indeed, according to the Beer–Lambert law, the light absorbed by a medium is proportional to the molar absorption coefficient ε_λ, to the absorption path length l and to the molar concentration M (McNaught & Wilkinson, 2014):

$$A = \varepsilon_\lambda l M$$

Therefore, the absorbance level is directly proportional to the molar concentration of formazan.

The protocol adopted for this procedure is as follows:

- **<u>Protocol 2</u>**: WST-1 assay
  - Removal of the culture medium from the flask;
  - Rinse of cells with Dulbecco's phosphate-buffered saline (DPBS, Gibco) without Ca^{2+} and Mg^{2+} to remove weakly anchored cells (300 µL for each well). This phase must be fast to avoid removing even the correctly bound cells;
  - Preparation of the medium without phenol red which could offset measures: Dulbecco's Modified Eagle's Medium (DMEM, Gibco), supplemented with 10% fetal bovine serum (FBS, Gibco), 2 mM L-glutamine (Gibco) and 1 mM sodium pyruvate (Gibco);
  - Addition of WST-1 to the medium with a 1:11 ratio: 4727 µL of medium and 473 µL of WST-1;
  - Removal of the rinse and addition of 200 µL of medium for each well. The fourth line of wells has not been filled to compare the cellular morphologies after the test (Figure 6.11);
  - Incubation of the plate at 37 °C for 90 minutes for allowing the WST-1 to work;
  - Supernatant fluid transfer (90 µL) to a 96 wells multiwell plate;
  - Analysis of supernatant liquid absorbance in a plate reader at 450 nm (Victor X3, Perkin Elmer).

Then the medium was added to the wells containing the substrates and a rinse with DPBS was performed to completely remove the WST-1. At this point 200 µL of formaldehyde was added in each well to make a fixation of cells. Fixation allows to preserve cellular architecture and composition of cells. Formaldehyde fixes tissue by cross-linking the proteins, primarily the residues of the basic amino acid lysine. It must act for 20 minutes at 4 °C in order to complete the process. At this point a rinse with DPBS was performed and fresh DPBS was added to conserve samples at 4°C.

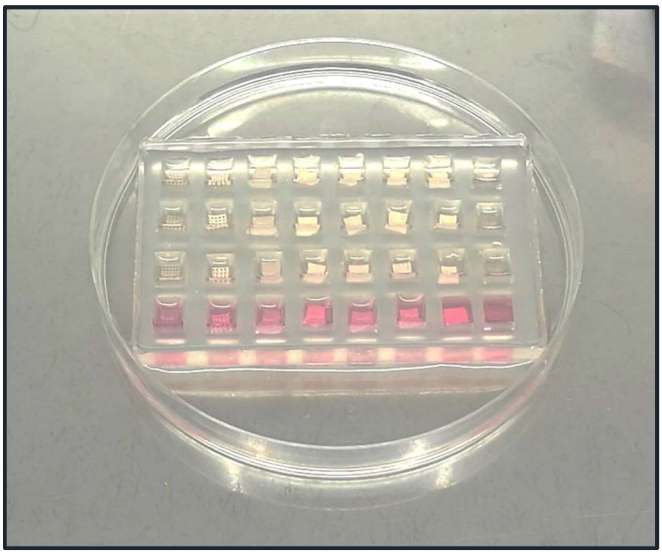

Figure 6.11 *– WST-1 could virtually alter cellular morphology. For this reason, the salt has not been added in the fourth line of wells to perform a more truthful imaging analysis.*

In order to quantitively evaluate the proliferation and adhesion of 3T3 on substrates the alamarBlue assay was also performed. This bioassay is based on an oxidation-reduction (REDOX) indicator (resazurin) that both fluoresces and changes colour in response to chemical reduction of growth medium resulting from cell proliferation (Lancaster & Fields, 1996). A state of continued growth maintains a reduced environment while inhibition of growth maintains an oxidized environment. Reduction related to growth causes the REDOX indicator to change from oxidized (non-fluorescent, blue) form to reduced (fluorescent, red) form (resorufin) (Lancaster & Fields, 1996). The detection of the absorbance levels represents a direct measure of the content of reorufin and consequently of the living cells concentration.

- **<u>Protocol 3</u>**: AlamarBlue assay
  - Removal of the culture medium from the flask;
  - Rinse of cells with Dulbecco's phosphate-buffered saline (DPBS, Gibco) without Ca^{2+} and Mg^{2+} to remove weakly anchored cells (300 µL for each well). This phase must be fast to avoid removing even the correctly bound cells;

- Preparation of the medium without phenol red which could offset measures: Dulbecco's Modified Eagle's Medium (DMEM, Gibco), supplemented with 10% fetal bovine serum (FBS, Gibco), 2 mM L-glutamine (Gibco) and 1 mM sodium pyruvate (Gibco);
- Addition of alamarBlue to the medium with a 1:11 ratio: 10 mL of medium and 1,1 mL of alamarBlue;
- Removal of the rinse and addition of 300 µL of medium for each well. (Figure 6.12);
- Incubation of the plate at 37 °C for 3 hours for allowing the alamarBlue to work;
- Supernatant fluid transfer (90 µL) to a 96 wells multiwell plate;
- Analysis of supernatant liquid absorbance in a plate reader at 570
- nm and 595 nm (Victor X3, Perkin Elmer).

Figure 6.12 *– AlamarBlue was added to each well with a 1:11 ratio.*

6.4.5 Cytochemistry

A fluorescent staining procedure was developed for determining the cells capability to adhere to the substrates and consequently for investigating the cytocompatibility of scaffolds. For this purpose, Hoechst 33342 (Invitrogen) and phalloidin-Tetramethylrhodamine B isothiocyanate (TRITC, Sigma Aldrich) fluorescent stains were used and a fluorescence microscopy was performed.

Hoechst 33342 (bisbenzimide) is an organic compound (Figure 6.13) belonging to blue fluorescent dyes used to stain cellular nuclei (Latt, et al., 1975).

Indeed, this dye binds to the minor groove of double-stranded DNA with a preference for sequences rich in adenine and thymine.

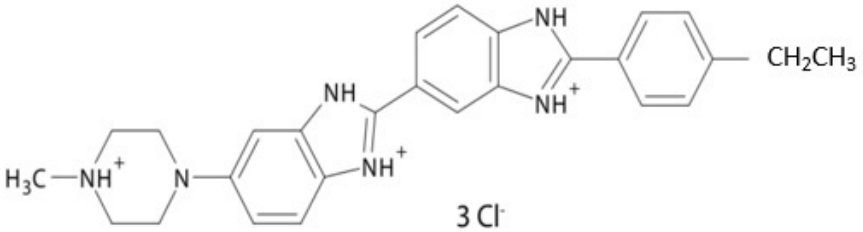

Figure 6.13 *– Chemical structure of Hoechst 33342.*

It is excited by ultraviolet light at around 350 nm and emits blue-cyan fluorescent light around an emission spectrum maximum at 461 nm (Figure 6.14 (a)) (Mocharla, et al., 1987). Phalloidin is a rigid bicyclic heptapeptide and belongs to a class of toxins called phallotoxins, that are found in the death cap mushroom *(Amanita phalloides)* (Lynen & Wieland, 1937). Due to its affinity for actin, phalloidin is used in fluorescence microscopy for localizing actin filaments (f-actin) that are the main components of cellular cytoskeleton, while TRITC provides orange-red fluorescence. TRITC dye is a bright, orange fluorescent dye with excitation ideally suited to the 540-545 nm laser line and an emission spectrum maximum at 570-573 nm (Figure 6.14 (b)).

The protocol adopted to perform fluorescence imaging is as follows:

- **<u>Protocol 4</u>**: Fluorescence staining of fixed cells
  - Addition of Triton X-100 (0.1%) in PBS for 15 minutes to permeabilize cellular membranes;
  - Rinse with PBS to remove all the detergent;
  - Addition of Hoechst 33342 and phalloidin-TRITC (300 nM);
  - Incubation for 30 minutes at room temperature, in soft light conditions;
  - Removal of fluorescent dyes;
  - Rinse and addition of PBS with Ca^{2+} and Mg^{2+};
  - Inversion and observation of samples with fluorescence microscopy.

a)

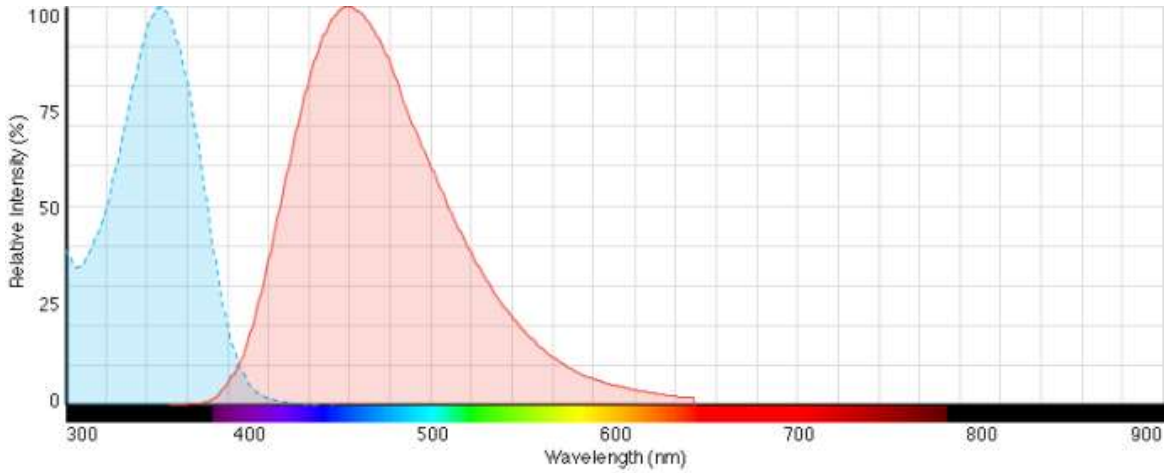

b)

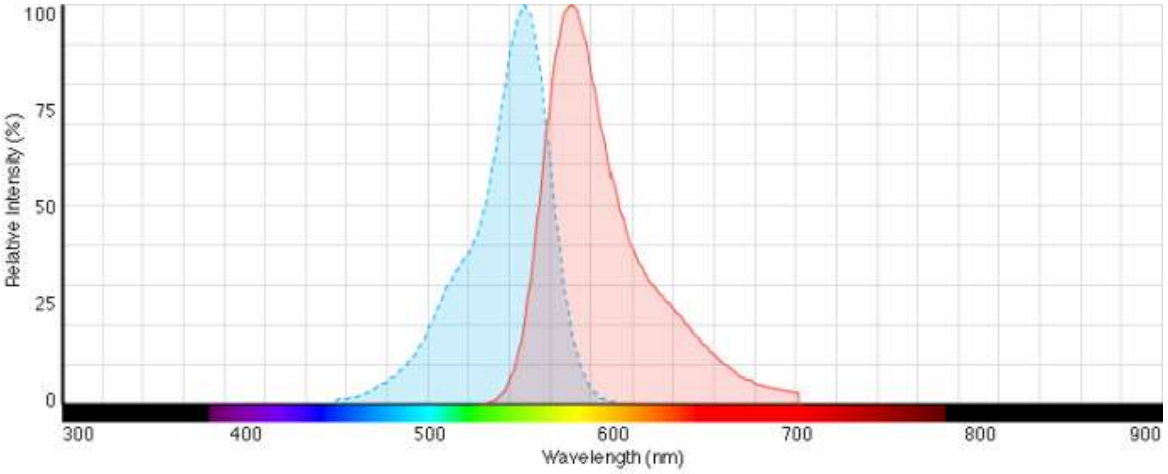

Figure 6.14 *– Excitation (blu) and emission (red) spectra of Hoechst 33342 (a) and TRITC (b) (https://www.thermofisher.com/order/catalog/product/H1399-R415).*

To carry out the fluorescence imaging, optical and confocal microscopes were employed.

The Nikon Eclipse Ti inverted optical microscope used in this work is shown in Figure 6.15 (a).

It is composed by the following main components:

1. A mercury lamp, which emits light over the whole optical spectrum as well as in the ultraviolet range;
2. An optical excitation filter needed to isolate the wavelength specific to excite the fluorochrome;

3. A dichroic mirror that reflects the excitation light to the sample and simultaneously transmits only the emitted light from the sample to the detector (a CCD camera) and to binoculars;
4. An emission filter that transmits only the wavelengths of the emitted light from the sample blocking the unwanted background light;
5. A CCD camera that detects the light from the sample.

The camera is connected to a computer and the image can be also observed on the monitor through the NIS-Elements Advanced Research software. Figure 6.15 (b) shows a schematic diagram of the inverted fluorescence microscope working principle.

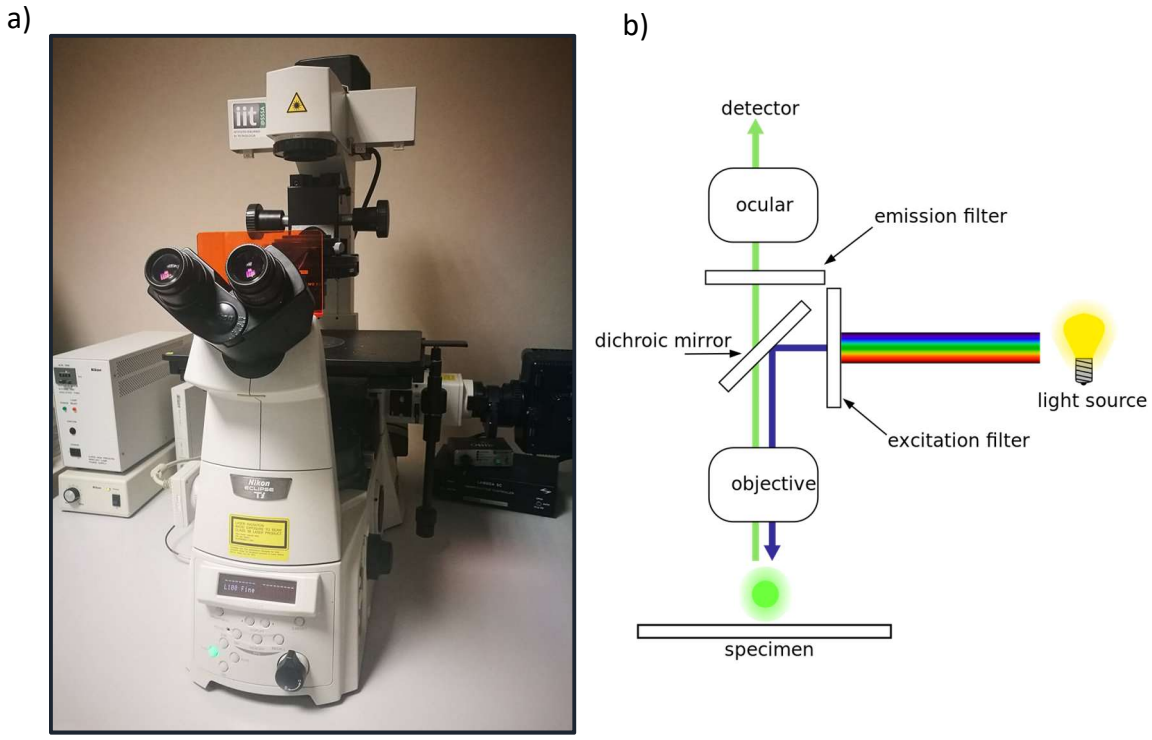

Figure 6.12 *– The inverted fluorescence microscope used in this work (a) and a schematic diagram of its working principle (b).*

The confocal microscopy is an optical imaging technique that can capture multiple two-dimensional images at different depths in a sample and rebuild the three-dimensional structure of the object. This process is known as optical sectioning. Moreover, the resolution is better than a traditional microscope.

Indeed, this technology allows to detect only the fluorescence light very close to the focal plane since the out-of-focus signal is eliminated by a pinhole in an optically conjugate plane in front of the detector. More precisely, a laser source emits the light which is collimated by a lenses and mirrors system on the sample. The light intensity from the sample focus plane is not shielded by the pinhole and is detected by a sensitive detector. Generally, this is a photomultiplier tube (PMT) or avalanche photodiode and converts the light signal into an electrical one that is recorded by a computer. Figure 6.16 shows the schematic structure of the confocal technology.

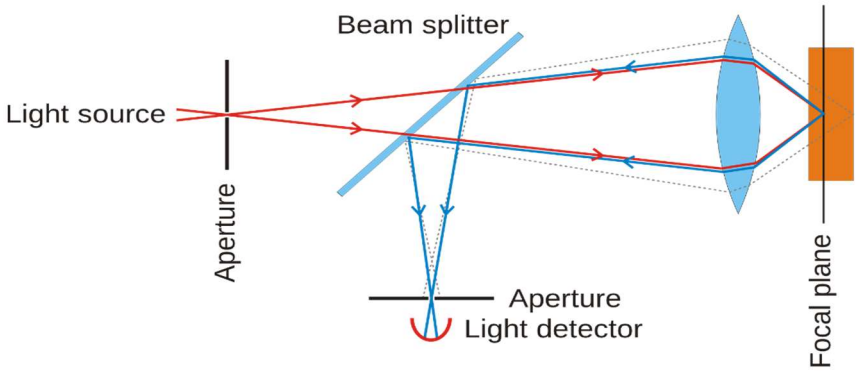

Figure 6.16 - *Schematic essential structure of a confocal microscope; for simplicity, the eyepiece has been omitted, positioning the detector at the point of formation of the intermediate image.*

In this thesis work the Nikon Eclipse Ti confocal microscope and NIS-Elements Advanced Research 4.13.03 were used to obtain two-dimensional and three-dimensional images.

6.5 Fibroblasts response to electric stimulation

Piezoelectric nanomaterials have shown to be a very promising tool for a wireless and targeted electric stimulation of cells and tissues. For instance, ultrasounds (US) represent a mechanical and non-invasive solicitation that can efficiently penetrate biological tissues in a non-harmful way. Some recent studies (Ciofani, et al., 2010; Marino, et al., 2015; Genchi, et al., 2016) report the successful remote stimulation of different cell types, prevalently neuronal-like cells, by synergistically exploiting biocompatible piezoelectric barium titanate nanoparticles (BTNPs) in combination with US. In this thesis work the intracellular Ca^{2+} levels of NIH 3T3 cells have been analysed through time-lapse Ca^{2+} imaging.

This experiment was carried out to evaluate the fibroblasts response to the electric stimuli in order to verify the effectiveness of the piezoelectric substrates. Two voltage-sensitive calcium channel types are present in the membrane of 3T3 fibroblasts: L-type (high voltage) and T-type (low voltage) (Chen, et al., 2015).

6.5.1 Ultrasounds stimulation and Ca^{2+} imaging

Prior to carry out the US stimulation and calcium imaging, a stock solution of 50 µg Fluo-4 AM (1 µM, Invitrogen) and 16,6 µl of DMSO was prepared. Then, cells were incubated for 30 min at 37°C with a solution (2.7 µM) prepared by mixing the stock (0.7 µl) and the phenol red-free DMEM (1 ml). Samples were successively rinsed with PBS and incubated with HEPES-supplemented (25 mM) phenol red-free DMEM (Thermo Fisher) for time-lapse fluorescence imaging. The confocal microscope (Eclipse Ti-E epifluorescence microscope, Nikon) was used to perform the calcium imaging. US stimulations were applied with a KTAC-4000 device (Sonidel) with a planar ultrasound transducer of 20 mm diameter by setting 1 W/cm^2, 0.5 Hz burst rate, and 10% duty cycle (Figure 6.17). This US configuration setting is not able to induce detectable temperature increases of cell medium even after many hours of stimulation. The experiment was carried out by stimulating the 3T3 fibroblasts on the piezoelectric substrates and on the control for 192 s. Fluorescence intensities at different time points were calculated as mean value of pixels measured in intracellular region of interest (ROI), once subtracted the extracellular background. The probe (Fluo-4 AM) enters the cell and binds to Ca^{2+}. As a result, the fluorescence intensity is proportional to the Ca^{2+} concentration:

$$F = \mathrm{K}\,[\mathrm{Ca}^{2+}]$$

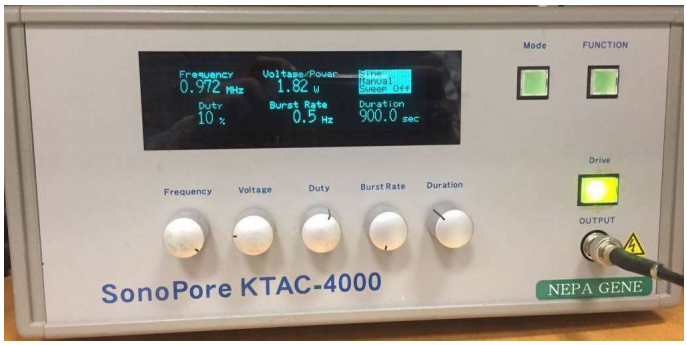

Figure 6.17 *– The SonoPore KTAC-4000 device used for the US stimulation.*

Results

7 PLA and PLA/BTNPs nanofibers

The nanofibers obtained by electrospinning of S9 (solution of 14% w/v PLA) in acetone) are defect-free and with a homogeneous distribution of diameter sizes. The electrospinning parameters that were set (see Table 4.4) allow to spin a continuous jet which leads to the formation of a uniform fibrous mat. Figure 7.1 shows scanning electron microscopy (SEM) images of PLA nanofibers with 2000X and 20000X magnifications.

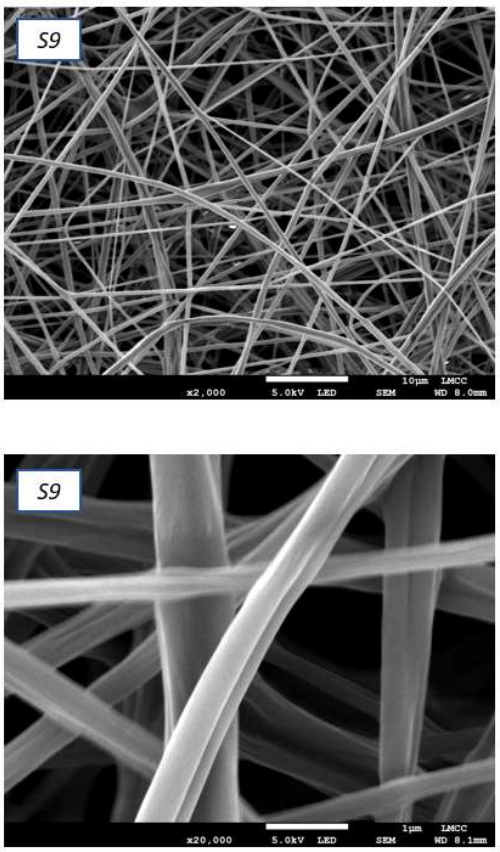

Figure 79.1 *– SEM images of PLA nanofibers with 2000X (top) and 20000X (bottom) magnifications.*

Figure 7.2 shows PLA/BTNPs nanofibers obtained by electrospinning of P8, P9, P10, P11 dispersions (see Table 4.3) with the conditions previously illustrated in Table 4.4. The maximum concentration of barium titanate nanoparticles that has been tested is 100 mg/ml. The fibers produced starting from P10 and P11 solutions present beads and break points due to the low elongation at break of PLA.

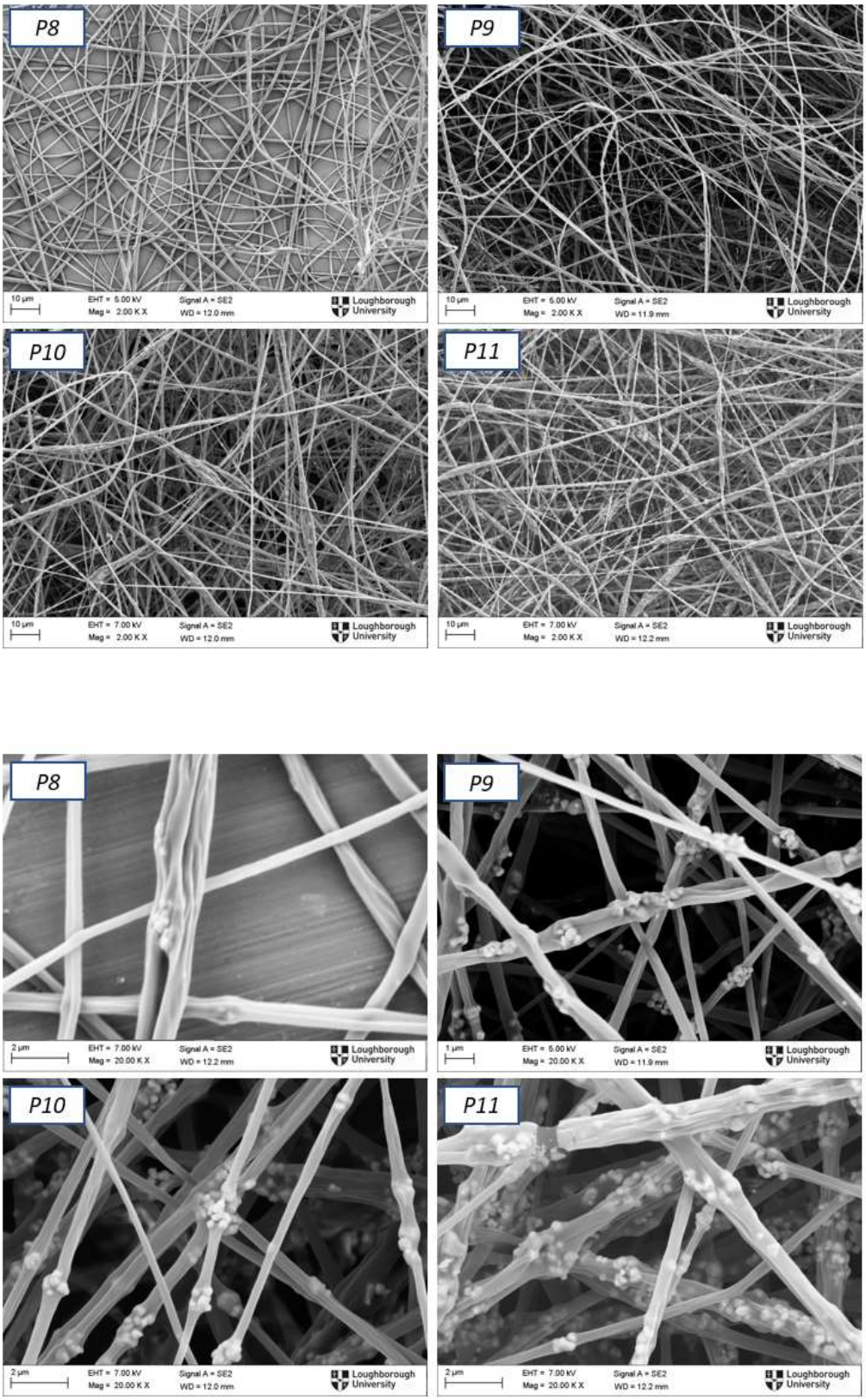

Figure 7.2 - *SEM images of PLA/BTNPs nanofibers with 2000X (at the top of the page) and 20000X (at the bottom of the page) magnifications. Defects and break points are visible in electrospun fibers with 50 mg/ml and 100 mg/ml particle loadings (P10 and P11).*

8 PCL and PCL/BTNPs nanofibers

Polycaprolactone based solutions have been optimized by trying various concentrations, in order to find the suitable type of solvent, molecular weight and viscosity to produce defect-free nanofibers. The PCL formulations that have been tested are listed in Table 4.2: S1, S2, S3, S4, S5, S6, S7 and S8. To choose the more appropriate concentration of polymer, the opportune solvent and the correct process parameters, the fibrous mat has been analysed by means of optical microscopy and scanning electron microscopy. The Taylor's cone has also been evaluated through the camera of the electrospinning system. Table 8.1 shows a summary of the nanofibers morphology for each PCL solution. The process parameter used have been previously reported in Table 4.4.

Table 8.1 *– Morphological characteristics of nanofibers resulting from the electrospinning of PCL solutions.*

Solutions	**PCL% (w/v)**	**Solvent**	**Morphologic characteristics of nanofibers**
S1	14	DCM	High and irregular diameter sizes. Presence of superficial defects.
S2	14	DCM:methanol (7:3)	Difficulty to carry out the electrospinning process. The viscosity of solution is excessive.
S3	13	DCM:methanol (7:3)	Branched and broken fibers.
S4	12	DCM	Presence of beads. Non-uniform fibrous mat.
S5	10	DCM	Presence of beads, non-homogenous fibers and difficulty to carry out the electrospinning process.
S6	10	DCM:methanol (7:3)	Uniform and defect-free fibers with small diameter sizes.
S7	8	DCM:methanol (7:3)	Ribbon shaped fibers and presence of superficial defects.
S8	6	DCM	High concentration of beads. Branched and broken fibers. The viscosity is insufficient.

Figure 8.2 shows SEM images of nanofibers obtained by electrospinning of S1, S4, S5 and S7 dispersions. The defects highlighted in Table 8.1 are indicated using arrows or circles.

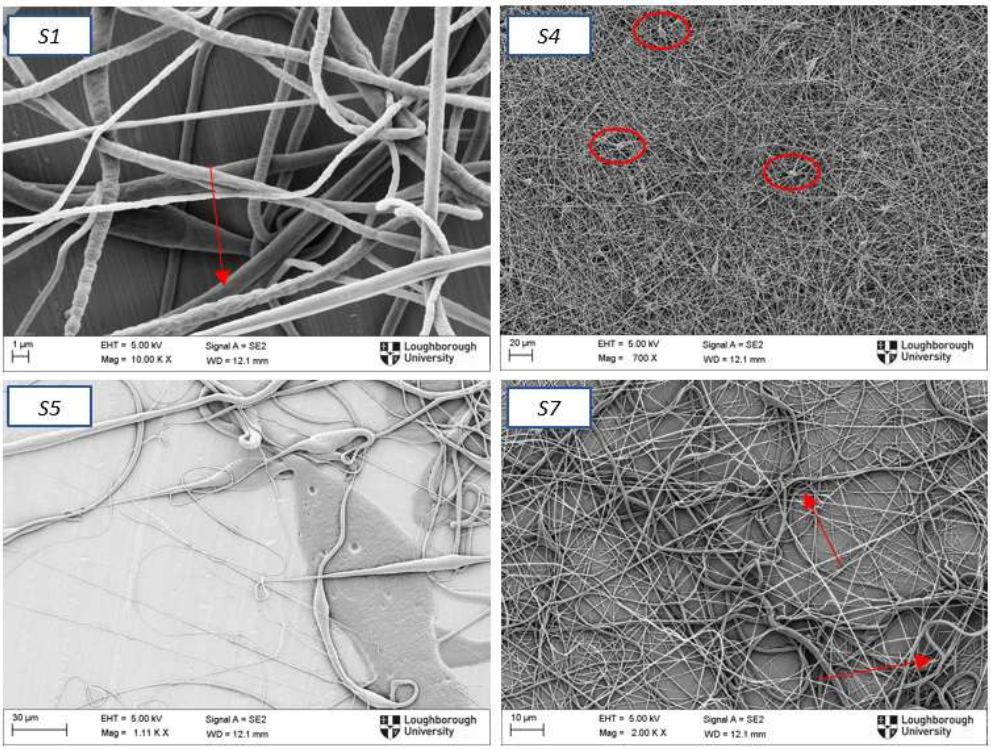

***Figure 8.2** – SEM images of nanofibers obtained by electrospinning of S1, S4, S5 and S7 solutions. Superficial defects, beads and ribbon shaped fibers are indicated by arrows and circles.*

The solution that allows to obtain defect-free and homogenous fibers with small diameters is S6 (10% w/v PCL in DCM:methanol (7:3)). Moreover, the Taylor cone shape is better defined for S6 than for other solutions (Figure 8.3).

Figure 8.4 shows SEM images, of PCL nanofibers obtained by electrospinning of S6.

The following images in Figure 8.5 and Figure 8.6 show PCL/BTNPs nanofibers obtained by electrospinning of P1, P2, P3, P4, P5, P6 and P7 dispersions (see Table 4.3) with the conditions previously illustrated in Table 4.4. The maximum concentration of barium titanate nanoparticles that has been tested is 250 mg/ml, decidedly higher than the content of particles tested for PLA. For this reason, PCL has been chosen to fabricate the wound dressings. Indeed, PCL fibers remain defect-free and uniform even with the highest particles loads.

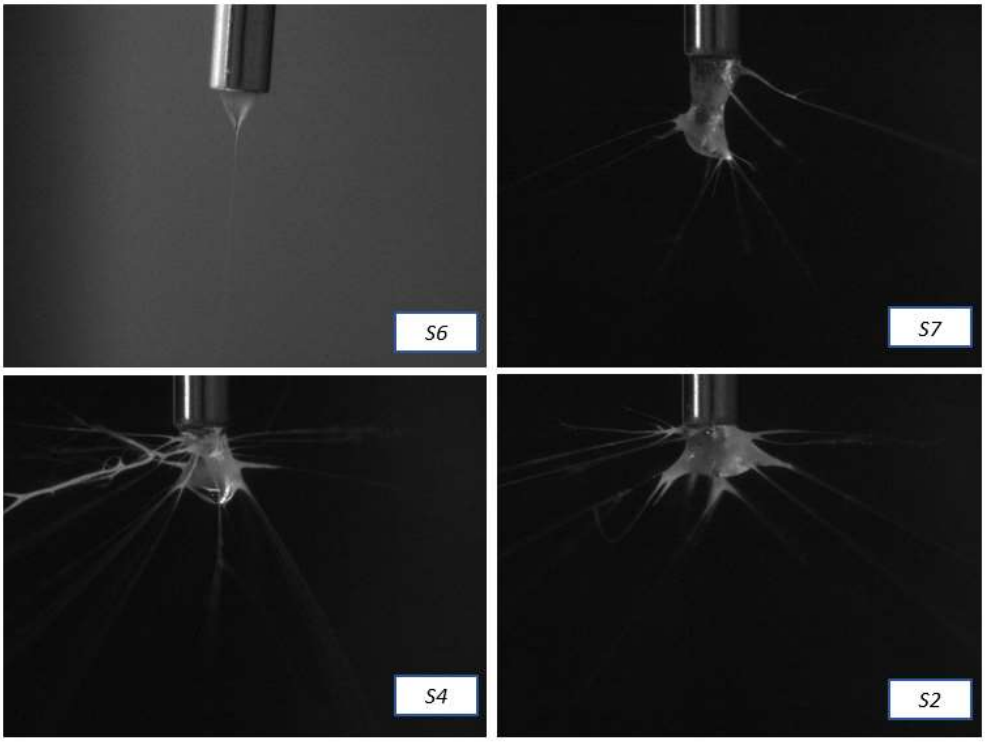

Figure 8.3 – *Photographs of the **T**aylor cones formed during the electrospinning process for different solutions. Taylor cone formed by S6 solution has a well-defined shape.*

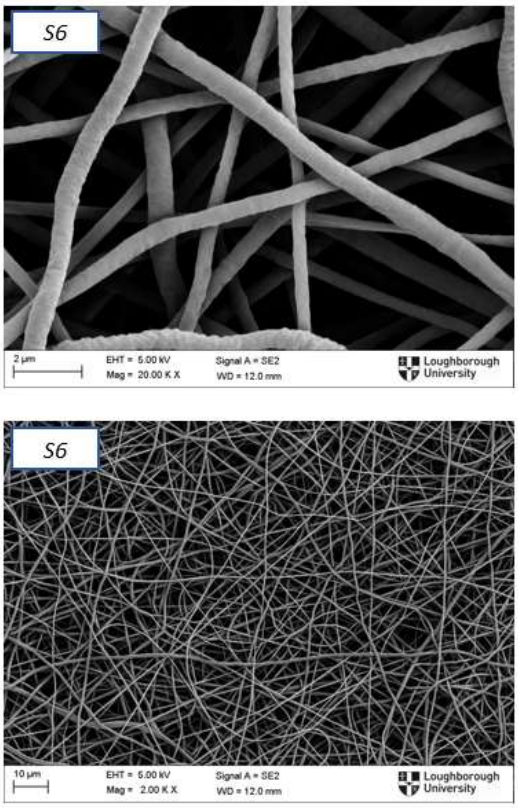

Figure 8.4 - *SEM images of PCL nanofibers with 2000X (top) and 20000X (bottom) magnifications.*

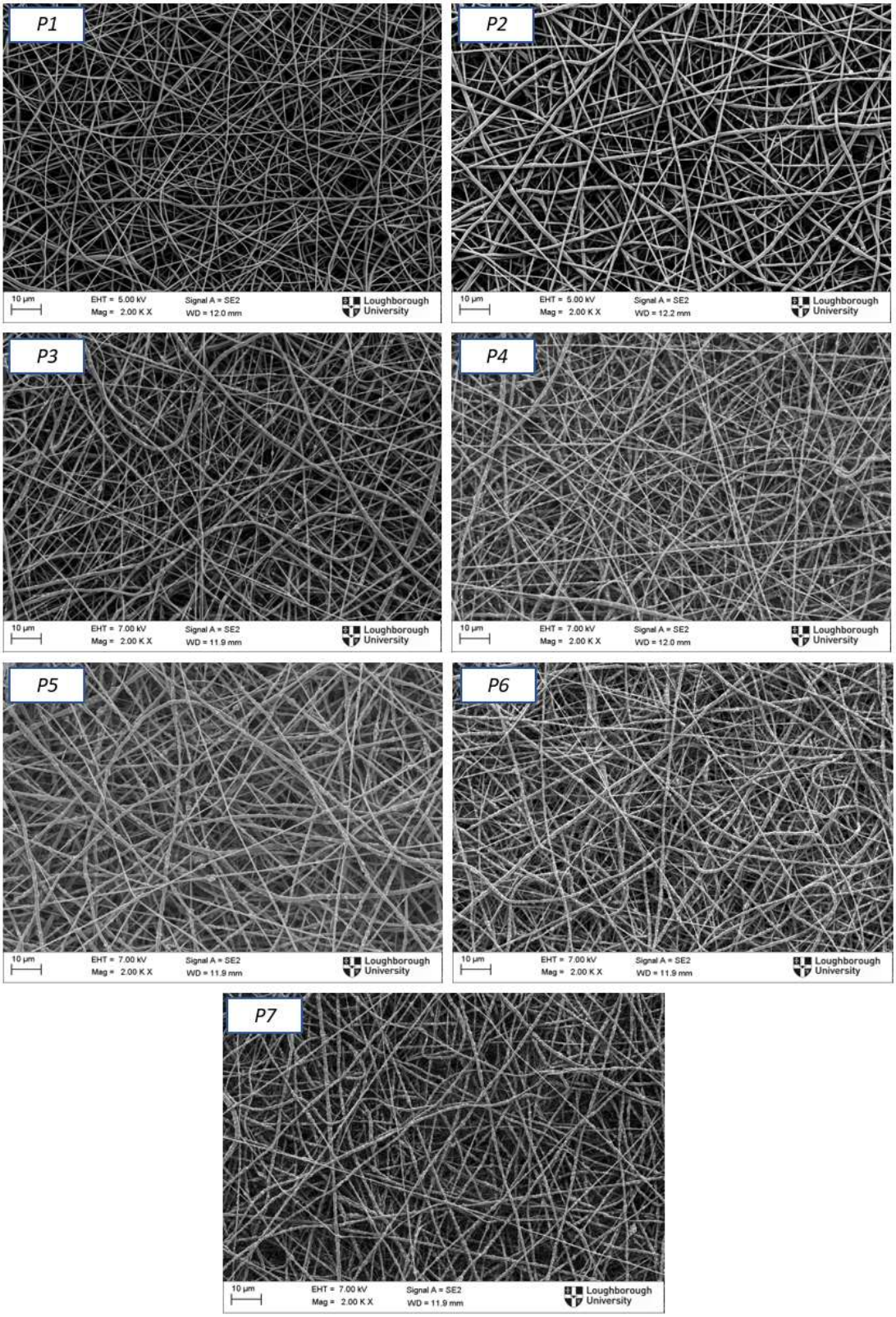

Figure 8.5 *– SEM images of PLA/BTNPs nanofibers. A magnification of 2000X, a voltage of 7 KV and a working distance (WD) of 11.9 mm were set. The concentrations of BaTiO3 nanoparticles are 10 mg/ml (P1), 30 mg/ml (P2), 50 mg/ml (P3), 100 mg/ml (P4), 150 mg/ml (P5), 200 mg/ml (P6) and 250 mg/ml (P7).*

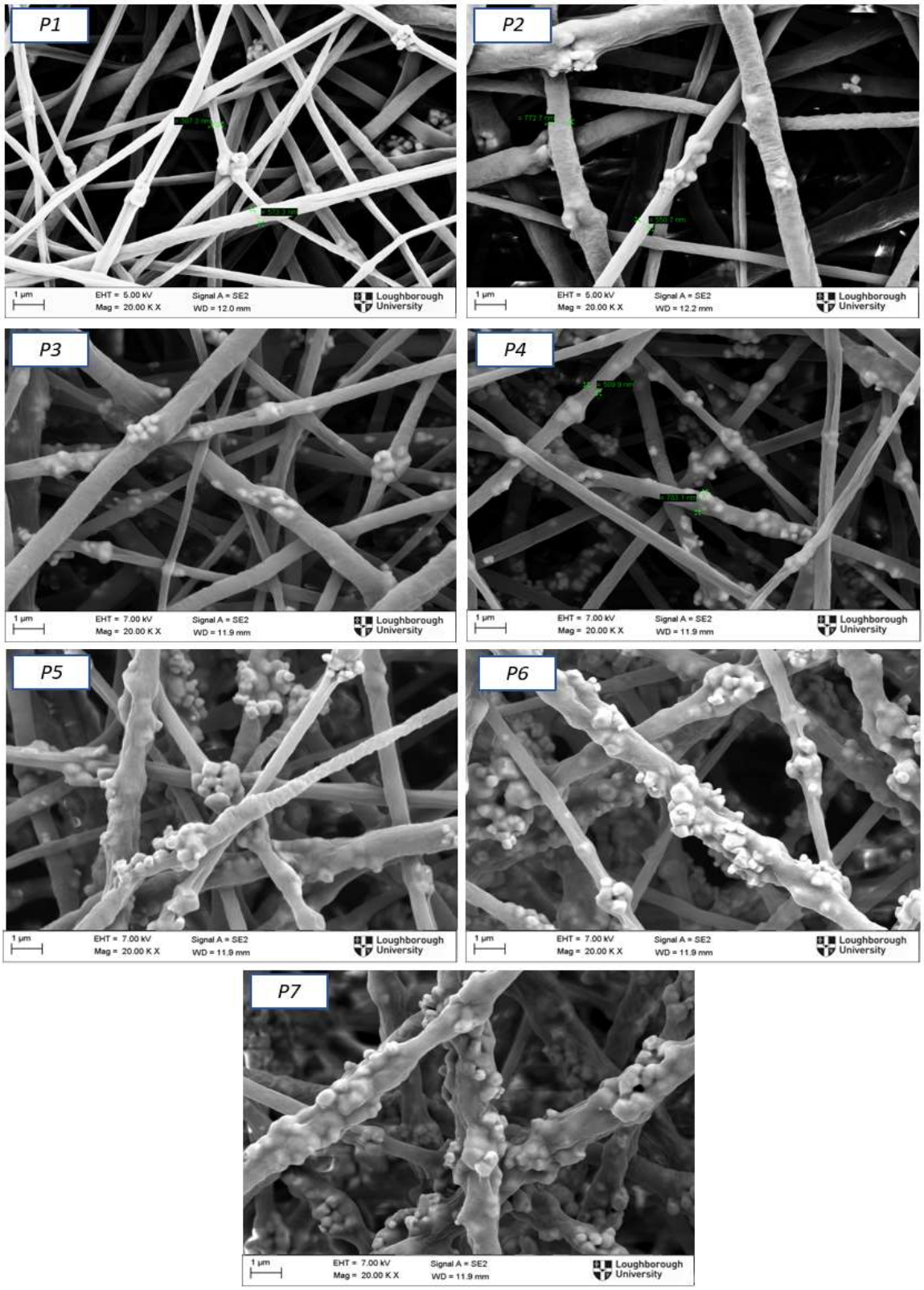

Figure 8.6 – *SEM images of PLA/BTNPs nanofibers. A magnification of 20'00X, a voltage of 7 KV and a working distance (WD) of 11.9 mm were set. The concentrations of BaTiO3 nanoparticles are 10 mg/ml (P1), 30 mg/ml (P2), 50 mg/ml (P3), 100 mg/ml (P4), 150 mg/ml (P5), 200 mg/ml (P6) and 250 mg/ml (P7).*

To better investigate the morphology of PCL/BTNPs nanofibers, the samples were also analysed by scanning and transmission electron microscopy (STEM). Figure 8.7 shows fibers obtained by P4, P5, P6 and P7 dispersions. The magnifications are around 30000X and acquisitions were performed by using both dark-field and high-angle annular dark-field imaging. The morphology of the nanofibers is not distorted by the particles, the circular diameter section endures, the size remains in the order of hundreds of nanometers and no breakage develops even with loads of 250 mg/ml. Although the particles tend to form aggregates, the appearance of surface defects or beads does not occur.

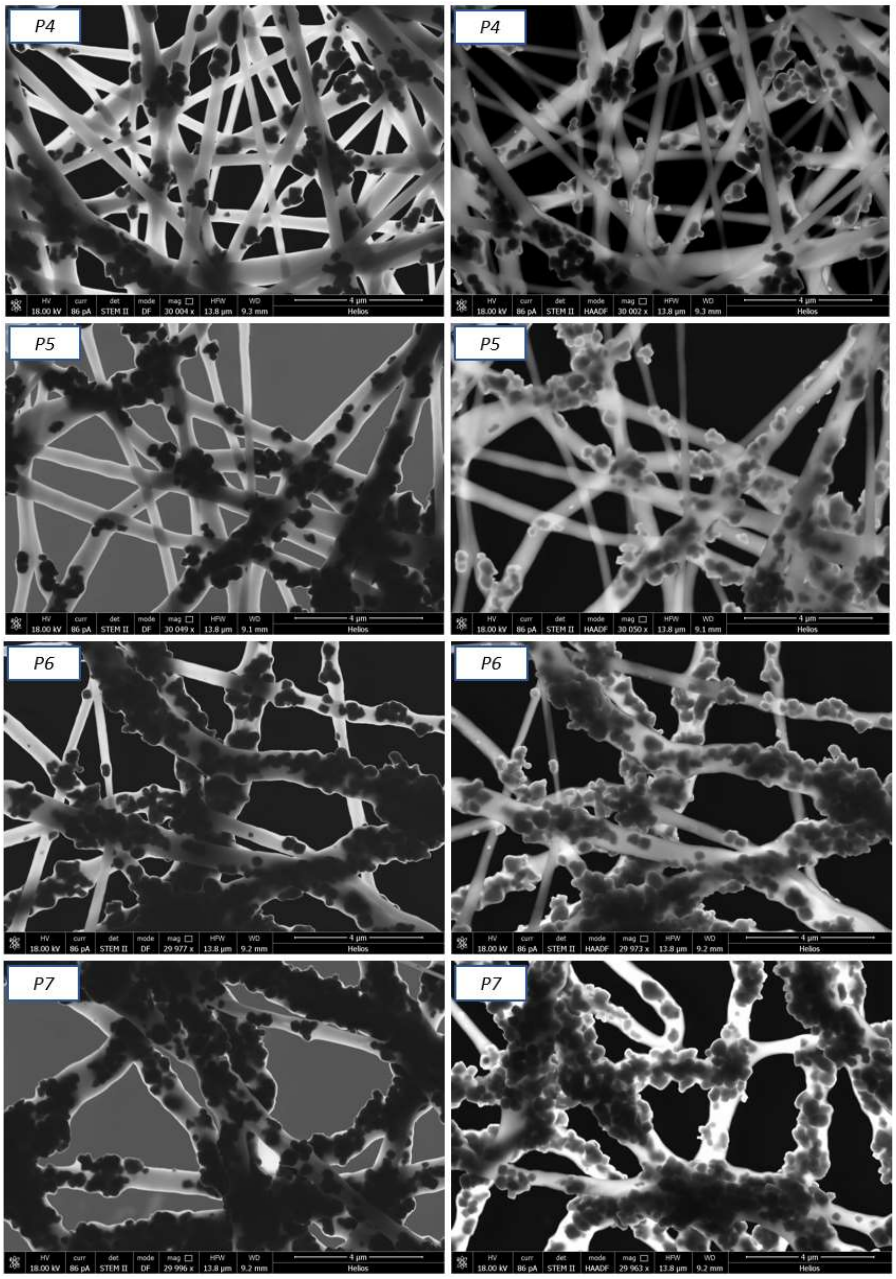

***Figure 8.7** – STEM images of nanofibers obtained by electrospinning P4, P5, P6 and P7 solutions. Images were acquired with DF imaging (on the left) and HAADF imaging (on the right).*

9 3D-printed scaffolds and Composites

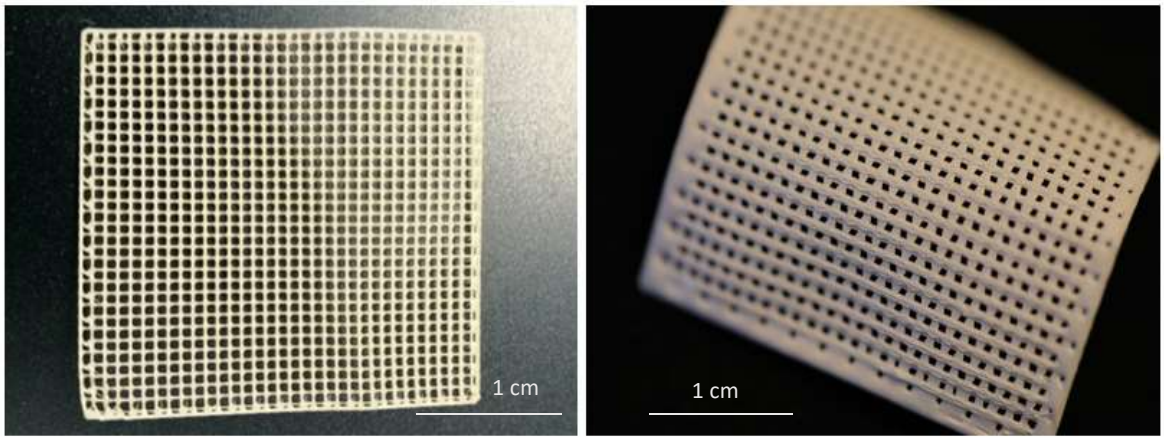

***Figure 9.1** – 3D-printed PCL scaffold (on the left) and 3D-printed PCL/BTNPs scaffold (on the right).*

Figure 9.1 reports the printed scaffolds obtained by performing two different temperature processes: the high-temperature procedure to produce the PCL scaffold and the low-temperature procedure to fabricate the PCL scaffold with 500 mg/ml $BaTiO_3$ nanoparticles. The images show the final porosity sizes that correspond to 0.9 mm for the non-piezoelectric construct and 0.5 mm for the piezoelectric construct. Additional analyses on the porosity of the PCL/BTNPs scaffold have been carried out by using an inverted microscope (Figure 9.2).

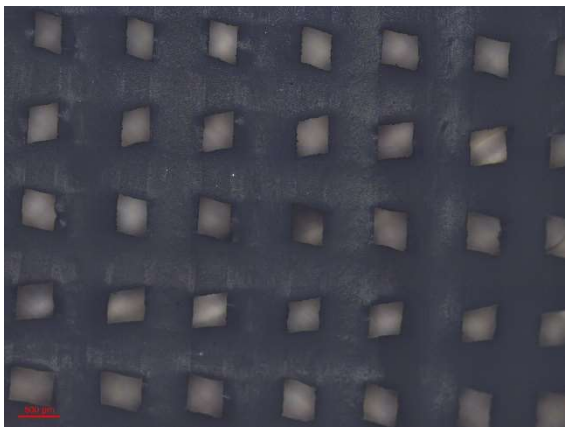

***Figure 9.2** – PCL/BTNPs scaffold image obtained by using the Leica DMi8 inverted optical microscope.*

Two different locations on the sample showed in Figure 7.10 have been chosen to perform an indicative analyse on the geometry of pores by using the software ImageJ (Figure 9.3).

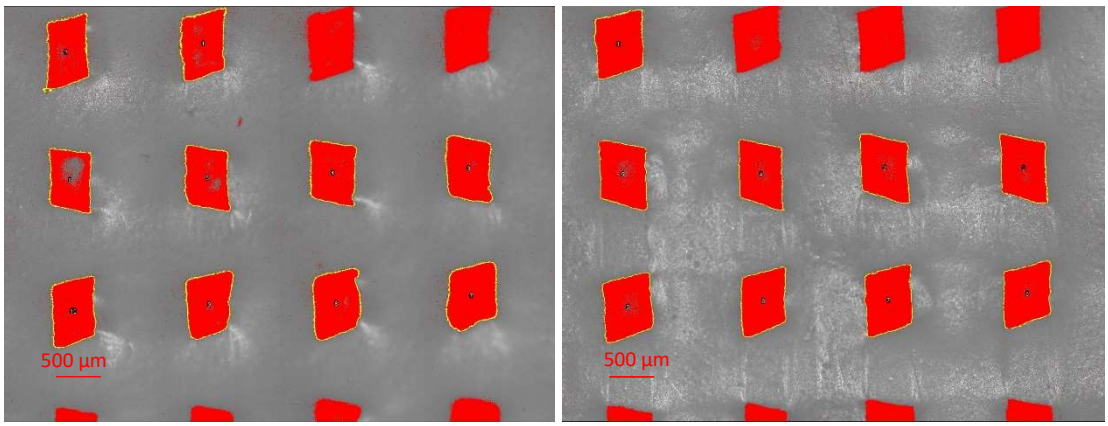

***Figure 9.3** – Location 1 (on the left) and Location 2 (on the right) of the same sample.*

The graphs displayed in Figure 9.4 report the perimeter and area trends of the 19 pores that have been calculated in Location 1 and Location 2.

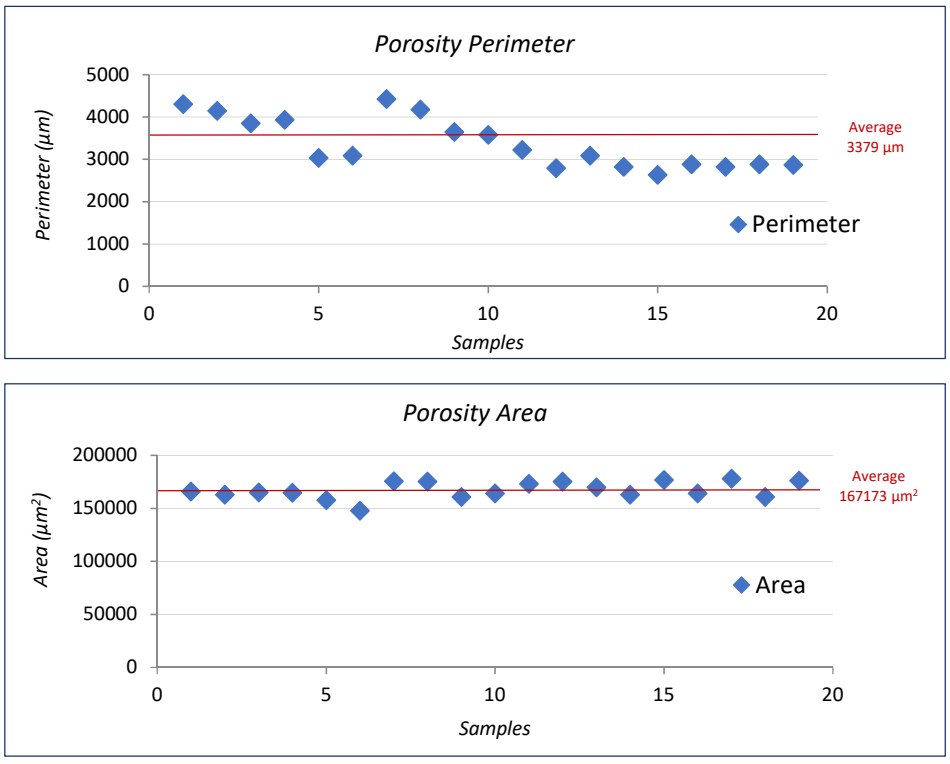

***Figure 9.4** – Area and perimeter trends evaluated on 19 pores (samples) of two different locations. The averages are shown in red colour.*

The values of areas and perimeters of pores vary, and the averages are 1.67×10^5 μm^2 and 3378 μm, respectively. The variability in the porosity geometry is probably due to the characteristics of the material. Indeed, as discussed in paragraph 5.3, the width of piezoelectric single strand results larger than that of non-piezoelectric strand because of the presence of nanoparticles and solvent. The strand, once deposited on the platform, is subjected to a stress relaxation which deforms the shape of each pore. Moreover, the nanoparticles are not uniformly distributed in the material, by provoking the consequent different sizes and shapes of porosity.

The composite wound dressings were observed by using a scanning electron microscope to verify the adhesion of the fibers to the scaffold (Figure 9.5). The fibers remain attached to the substrate even if subjected to a mechanical stretch.

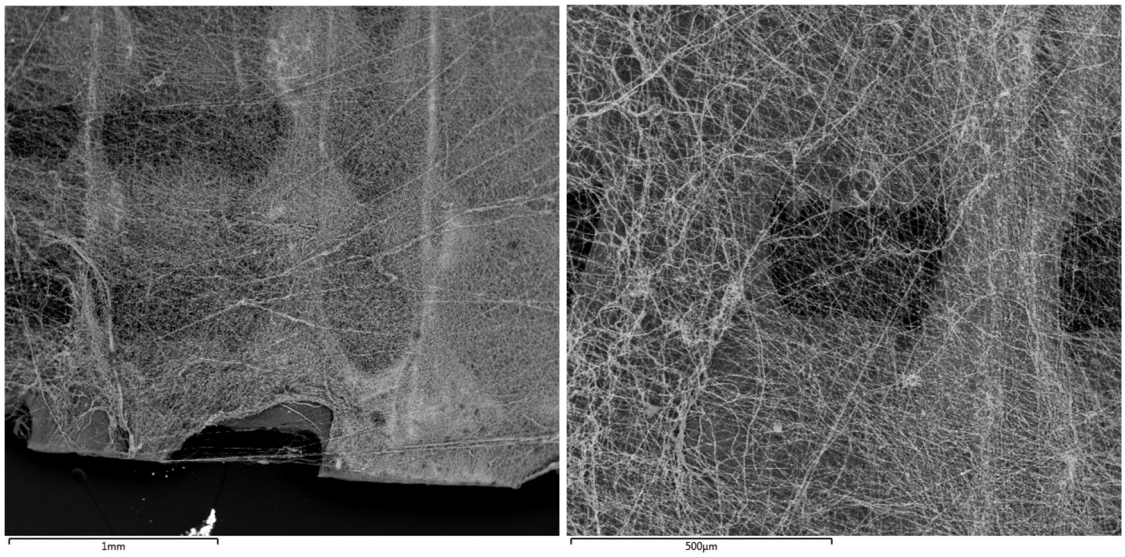

Figure 9.5 *– SEM images of the composite wound dressing: Electrospun fibers deposited onto a 3D printed scaffold.*

The composites and the printed scaffolds were also analysed by employing the inverted optical microscope. The following images, represented in Figure 9.6, show the non-piezoelectric scaffold (PCL0), the piezoelectric scaffold with 500 mg/ml of $BaTiO_3$ nanoparticles (PCL500) and the composites with fibers obtained by electrospinning P5 and P7 dispersions (PCL500-fPCL150 and PCL500-fPCL250).

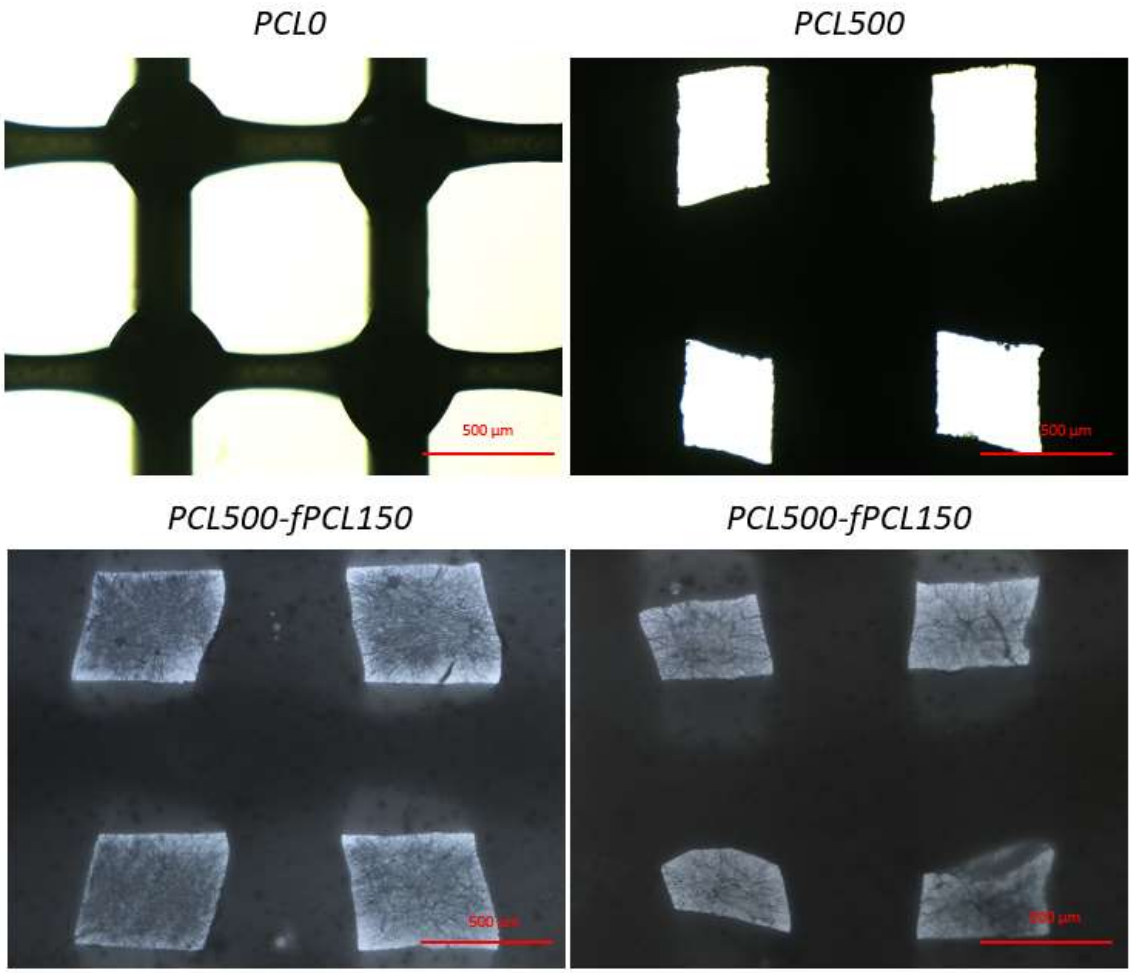

Figure 9.6 - *Images of 3D-printed PCL scaffold, PCL/BTNPs scaffold and composites obtained by using the inverted optical microscope.*

10 Cellular Responses

The response of NIH 3T3 and SaOS-2 cells was evaluated in terms of proliferation and viability, adhesion to the substrates and effect of the electric stimuli.

10.1 Proliferative capability of cells

Figure 10.1 reports the graphs relative to the WST-1 assay results for 3T3 and SaOS-2 cells. The experiment has been performed on 7 substrate typologies to compare the cellular response to each sample: non-piezoelectric scaffold (PCL0) piezoelectric scaffold (PCL500), non-piezoelectric PCL nanofibers (fPCL0), piezoelectric nanofibers with 150 mg/ml BTNPs (fPCL150), piezoelectric nanofibers with 250 mg/ml BTNPs (fPCL250) and composites (PCL500-fPCL150 and PCL500-fPCL250). Thermanox plastic coverslips have been used as control. The absorbance values showed on the y-axis have been obtain by measuring the light with a wavelength of 450 nm that has been absorbed by each sample. The statistical analysis has been conducted on different samples of the same day.

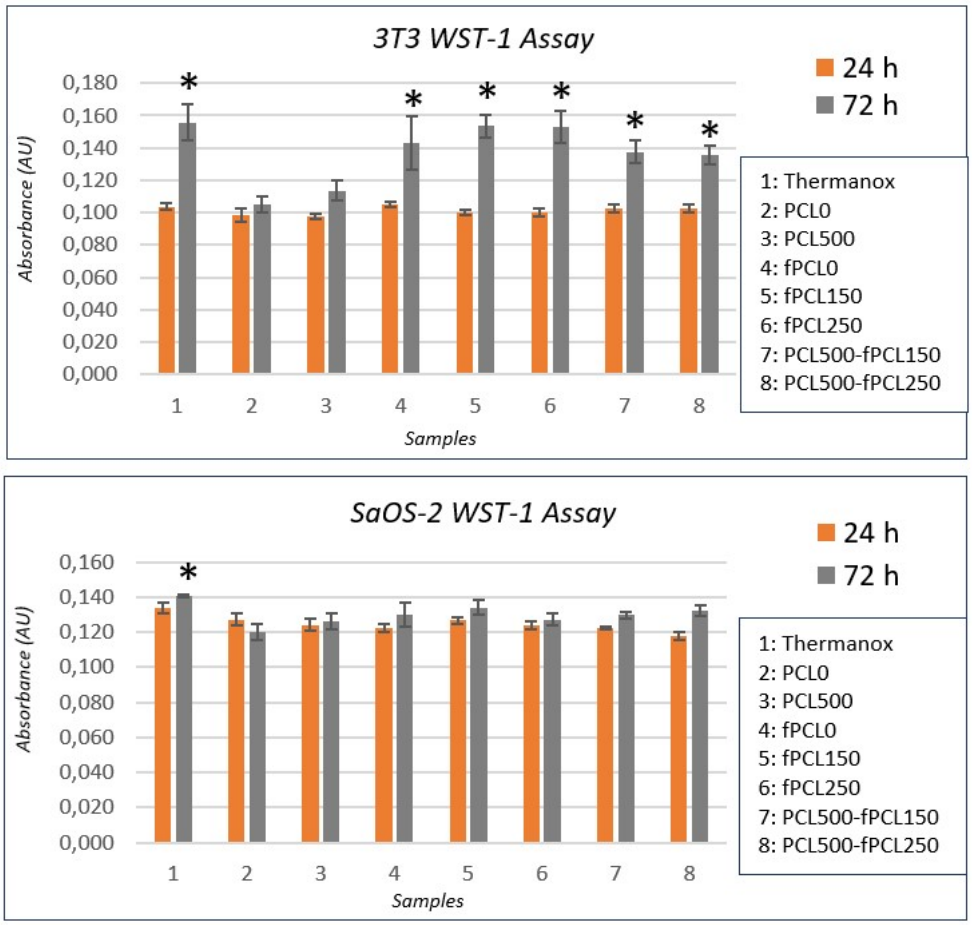

***Figure 10.1** – Results of WST-1 assay for 3T3 cells (at top) and SaOS-2 (at bottom).*

The results that have been measured in 3T3 cells after 24h from seeding demonstrate that the cellular adhesion is comparable for each substrate. By considering the absorbance values after 72h, the highest increment of proliferation occurs for samples 4,5 and 6 that correspond to the PCL nanofibers. These outcomes are reflected in literature (Fee, et al., 2016). Indeed, PCL electrospun nanofibers represent a suitable substrate for growth and proliferation of NIH 3T3 cells. The small differences between PCL nanofibers and composites (samples 7 and 8) suggest a good cytocompatibility of the composite wound dressings. On the contrary, as expected, the printed scaffolds without nanofibers (samples 2 and 3) are not appropriate substrates for cell proliferation because of the limited culture surface. The star indicates a statistically significant difference between samples 1-4-5-6-7-8 and samples 2-3. For SaOS-2 cells, the adhesion is comparable among all substrates. Indeed, after 24h from seeding, significative differences of absorbance levels do not appear. By evaluating the results after 72h from seeding, a cellular proliferation would seem not to occur. For this reason, cells adhesion and viability were also investigated with the alamarBlue assay, by increasing the cellular density.

Figure 10.2 reports graphs relative to the results of alamarBlue assay. The experiment has been performed on the same substrate typologies used for WST-1 assay. The absorbance values showed on the y-axis have been obtain by performing two readings with spectrometer: the first at 570 nm and the second at 595 nm.
The adhesion of 3T3 is comparable for all substrates. As for the WST-1 results, after 24h from seeding, significative differences among the absorbance values do not appear. On the contrary, after 72h the values increase and it suggests that the cellular proliferation occurs on every sample except the PCL0. The star indicates a statistically significant difference between samples 1-3-4-5-6-7-8 and the non-piezoelectric printed scaffold. Also in this case, the highest values are found for PCL nanofibers and composites (samples 6, 7, 8, 9). For SaOS-2 cells, the data reflect those obtained for 3T3 cells. The substrates that seem to have a better cytocompatibility are the nanofibrous PCL scaffolds (samples 5 and 6). The composites (samples 8 and 9) show absorbance levels higher than those of printed scaffolds without fibers, although the differences are not statistically significant.

Definitely, these data confirm the beneficial effects of structure nanofeatures that mimic the extracellular matrix (ECM) environment and represent a site for cells anchorage and growth.

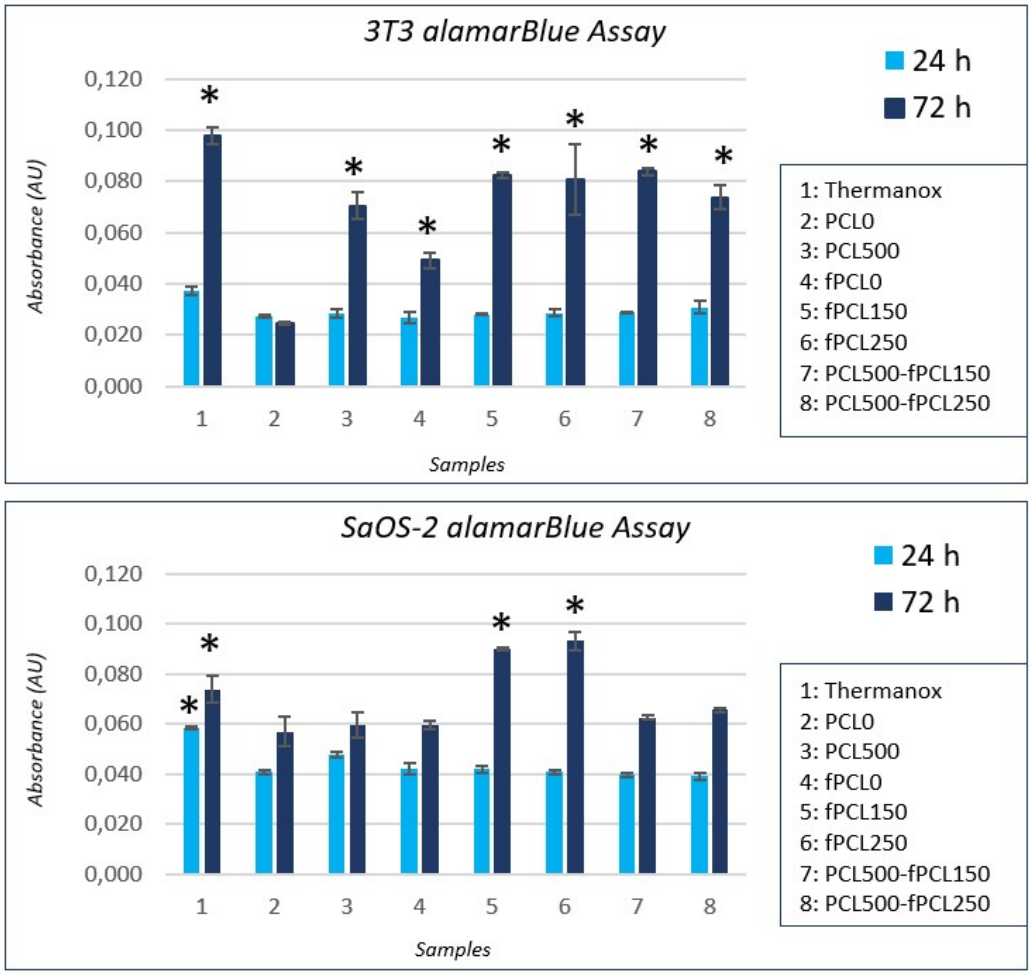

Figure 10.2 *– Results of WST-1 assay for 3T3 cells (at top) and SaOS-2 (at bottom).*

10.2 Cellular Adhesion

The adhesion of 3T3 and SaOS-2 cells after 72h of culture was evaluated by perform fluorescence imaging. Figure 10.3 and Figure 10.4 show images of 3T3 cells on different substrates and they are obtained by using the fluorescence microscope with 4X and 10X magnifications, respectively.

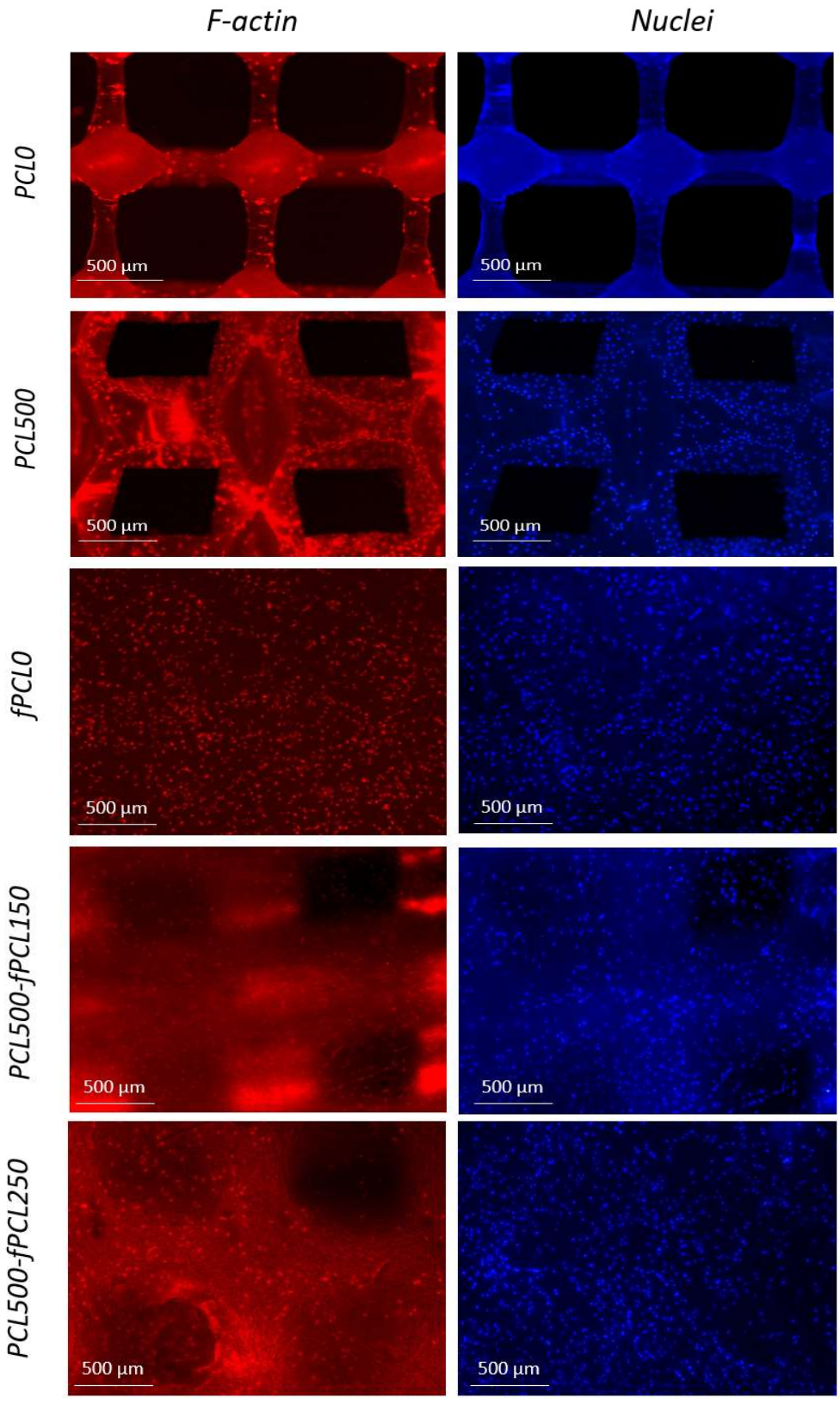

Figure 10.3 *– Fluorescence images of 3T3 f-actin (on the left) and nuclei (on the right). Non-piezoelectric scaffold (PCL0), piezoelectric scaffold (PCL500), non-piezoelectric nanofibers (fPCL0) and composites (PCL500-fPCL150 and PCL500-fPCL250) are shown with a 4X magnification.*

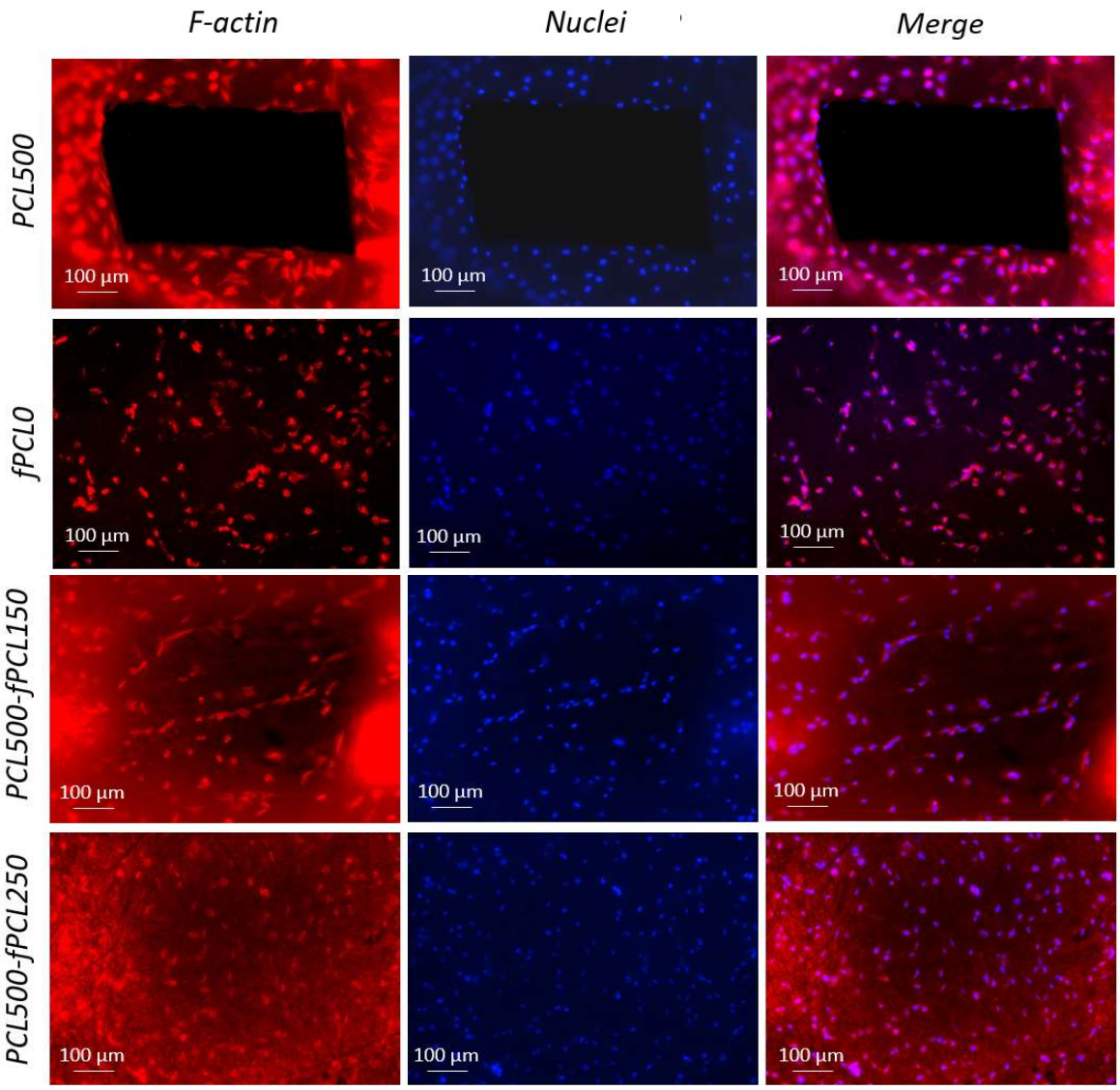

Figure 10.4 *– Fluorescence images of 3T3 f-actin (on the left), nuclei (in the middle) and merge (on the right). Piezoelectric scaffold (PCL500), non-piezoelectric nanofibers (fPCL0) and composites (PCL500-fPCL150 and PCL500-fPCL250) are shown with a 10X magnification.*

As expected, the cells primarily grew on substrates with a larger available area, spreading evenly over the entire surface. Indeed, on non-piezoelectric printed scaffolds the NIH 3T3 cells are anchored to the zone near the nodes, which represents the largest area in this substrate. The presence of piezoelectric nanoparticles of barium titanate does not affect cell adhesion and proliferation. The cells adhere indiscriminately to piezoelectric and non-piezoelectric substrates, as can be seen by comparing the images of the fPCL0 substrate with the others containing the BTNPs. Moreover, the 3T3 cells adhered both to the fiber-free scaffolds and to the composites, as is evident in the 10X magnification images showing the pores of composite wound dressing.

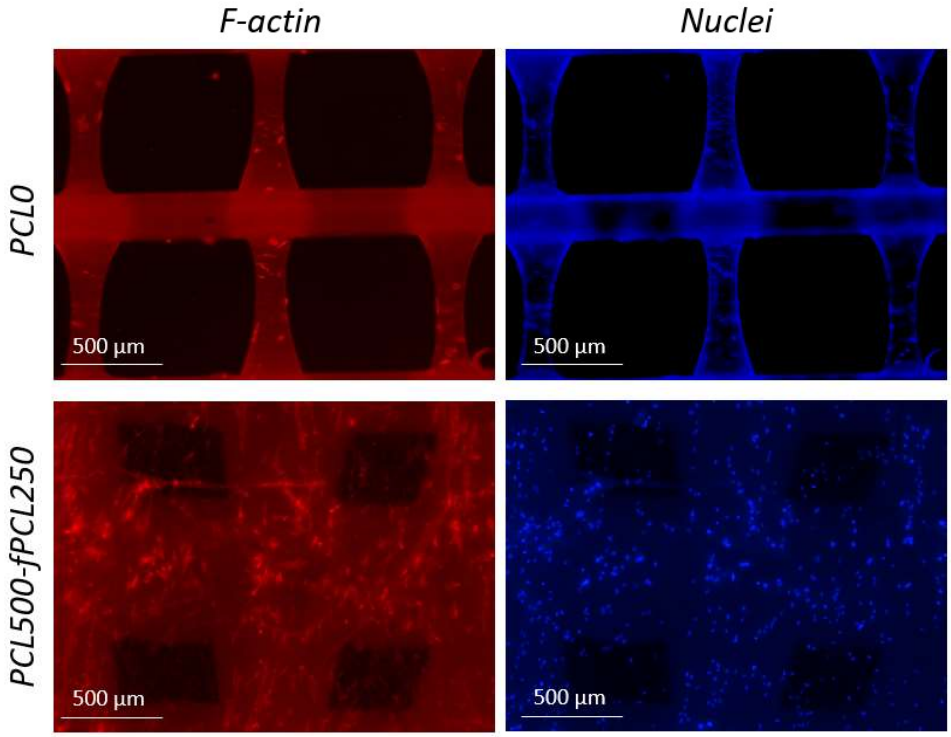

Figure 10.5 - *Fluorescence images of SaOS-2 f-actin (on the left) and nuclei (on the right). Non-piezoelectric scaffold and composite wound dressing (PCL500-fPCL250) are shown with a 4X magnification.*

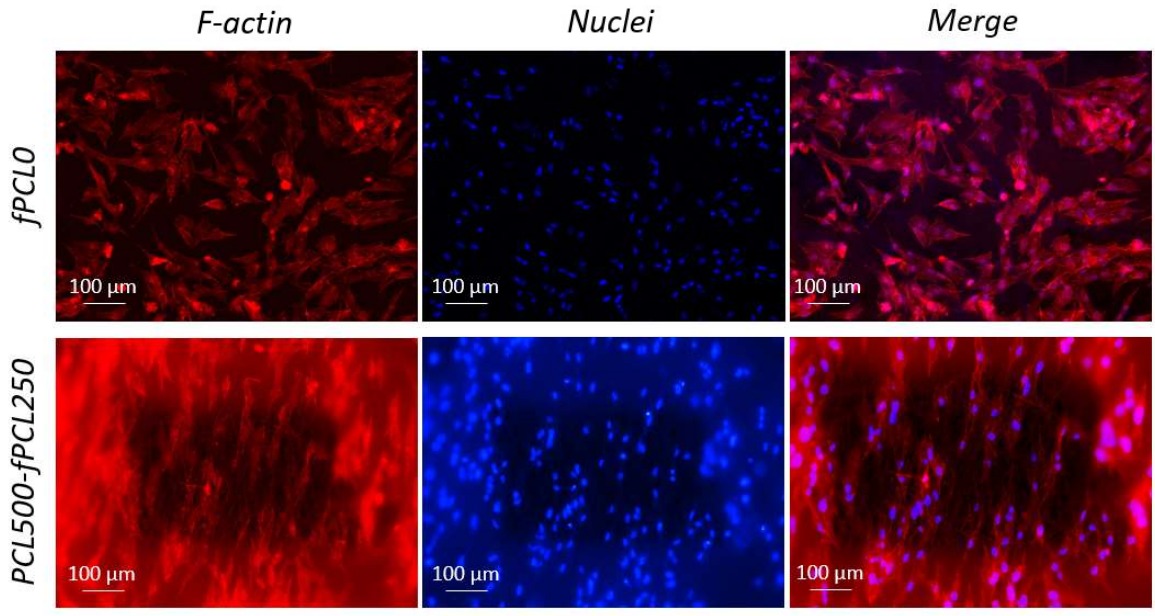

Figure 10.6 – *Fluorescence images of SaOS-2 f-actin (on the left), nuclei (in the middle) and merge (on the right). Non-piezoelectric nanofibers (fPCL0) and composite wound dressing (PCL500-fPCL250) are shown with a 10X magnification.*

Figure 10.5 and Figure 10.6, shown on the previous page, display images of SaOS-2 cells on three types of substrate and they are obtained by using the fluorescence microscope with 4X and 10X magnifications, respectively. The images show an optimal cells-substrate interaction. SaOS-2 cells are homogeneously distributed on substrates with a sufficient area of cell culture. These cells appear more spread and elongated than 3T3 cells that are smaller and have a more rounded morphology. Indeed, this type of fibroblasts generally develop few cytoplasmic protrusions even when the cell spreading phase occurs.

The following images were obtained with the confocal microscope by choosing 20X as magnification. They show a 2D slice and the 3D section of the composite final scaffold (PCL500-fPCL250) with 3T3 fibroblasts (Figure 10.7) and SaOS-2 cells (Figure 10.8). To form the three-dimensional image of the scaffold, a z-stack has been acquired by setting 100 slices with a step size of 580 nm.

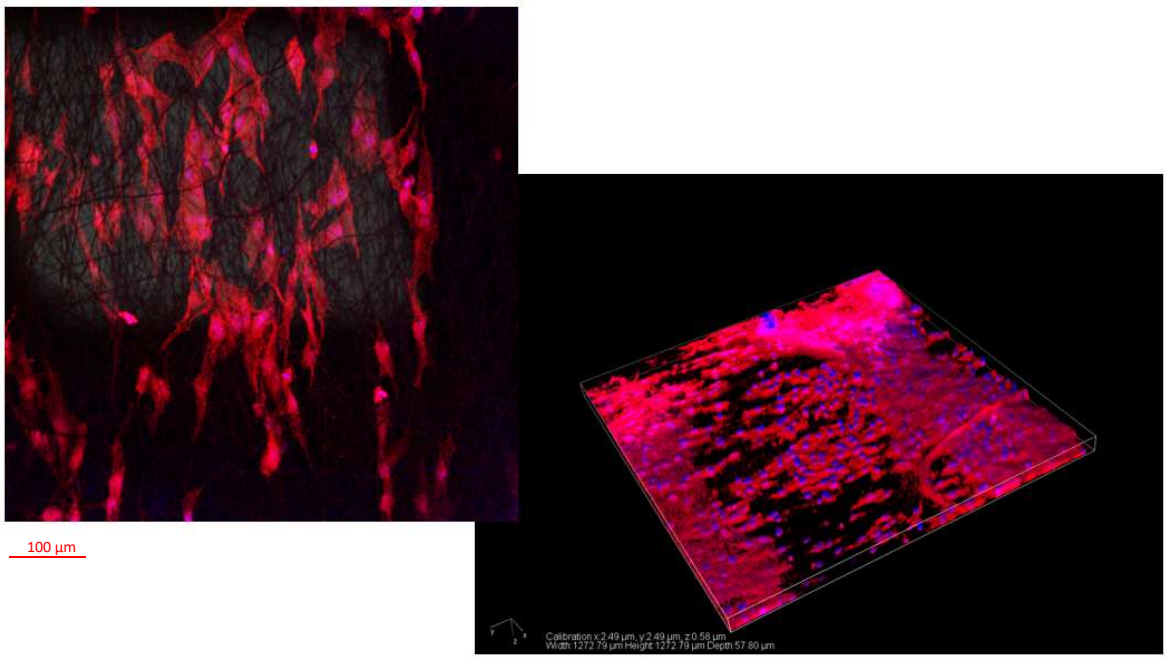

Figure 10.7 *– A 2D slice (on the left) of the 3D reconstruction (on the right) which has been obtained by acquiring a z-stack. The image shows the composite scaffold (PCL500-fPCL250) with 3T3 fibroblasts.*

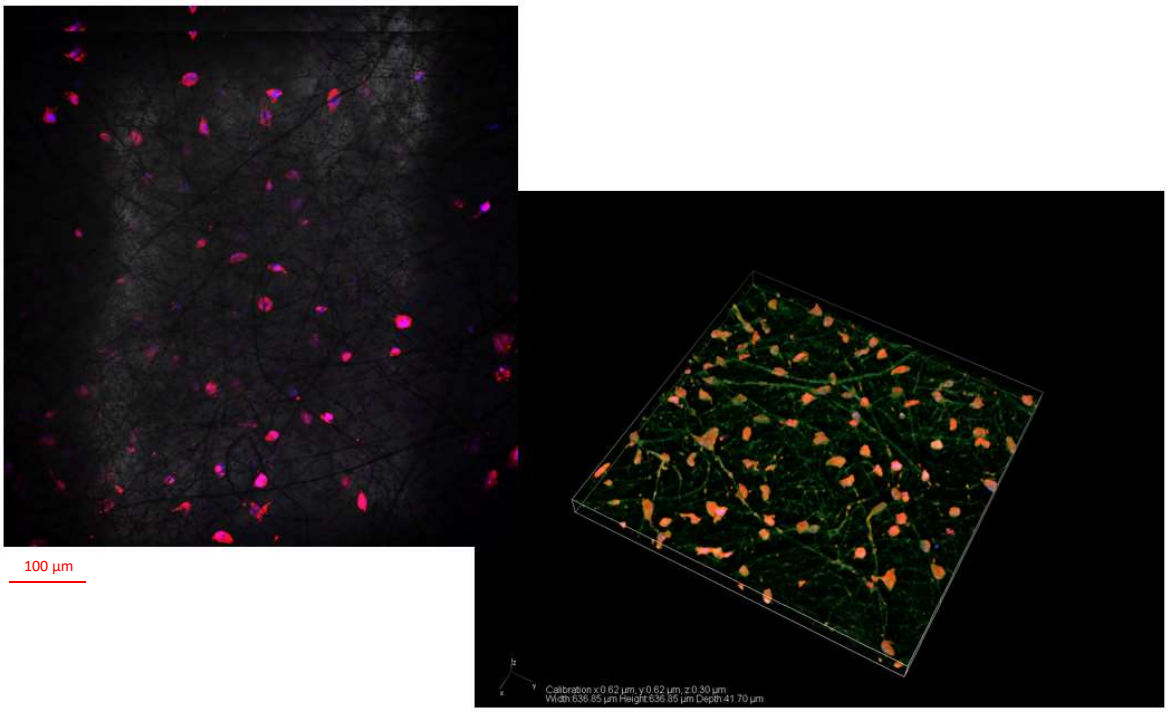

Figure 10.8 *– A 2D slice (on the left) of the 3D reconstruction (on the right) which has been obtained by acquiring a z-stack. The image shows the composite scaffold (PCL500-fPCL250) with SaOS-2.*

10.3 Piezoelectric Effect on Fibroblasts

Figure 10.9 reports plots relative to the measurements of the fluorescence intensity at different time intervals. The average fluorescence intensity of the different ROIs was indicated as F_0 at time $t = 0$ s, while for $t > 0$ s it was generically indicated as F. In the non-piezoelectric substrate (control) the intensity remains almost constant while in the piezoelectric final scaffold (composite) an increment of the fluorescence intensity occurs at the time the ultrasounds stimulation starts (136 s). The difference between the intensities and consequently between the calcium concentrations inside the fibroblasts is highlighted in the "Comparison" graph. This result demonstrates the efficacy of the barium titanate nanoparticles within the piezoelectric substrates. The NIH 3T3 cells respond to the wireless and targeted electric stimulation. Further analyses are necessary to investigate the role of the electric stimuli in proliferation, growth and migration of human skin cells.

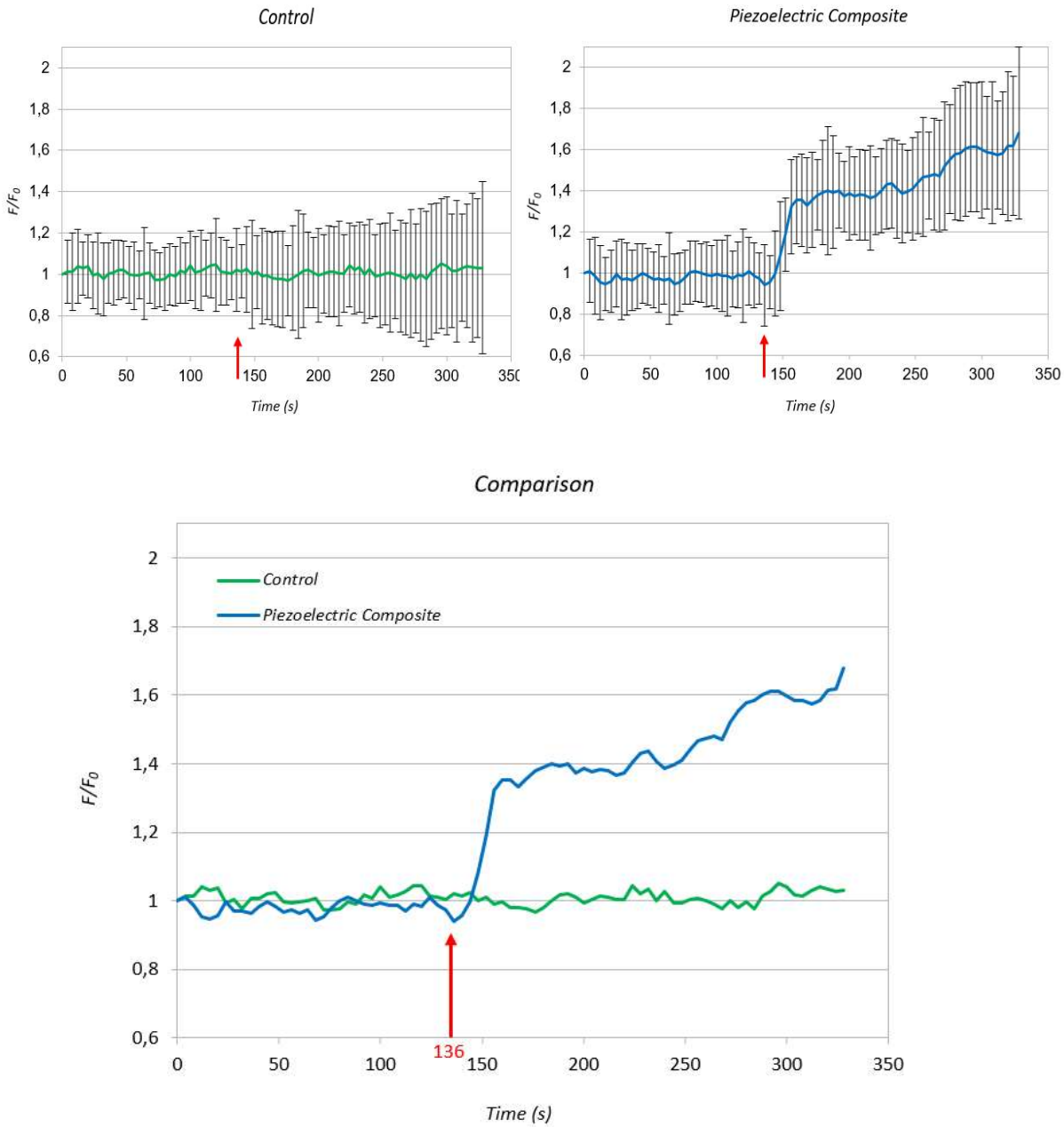

Figure 10.9 - *Fluorescence intensity at different time intervals. Graphs representing the average fluorescence intensity measured in the control (top left), in the piezoelectric composite (top right) and the plot showing the comparison between them (at bottom). The red arrow indicates the instant in which the stimulation starts.*

Discussion

Diabetes mellitus, peripheral arterial disease, venous insufficiency and pressure ulcers represent pathologies that generally lead to the formation of chronic skin wounds. They are characterized by a continuous inflammatory state with excessive levels of cytokines, exudate and necrosis. In this thesis project an advanced, biomimetic and responsive wound dressing has been developed with the purpose of improving the healing process and stimulating the regeneration of chronic wounds.

The biomimetic aspect has been reproduced by designing a hierarchical scaffold made with two different techniques: 3D Bioprinting and Electrospinning. As some recent studies (Puppi, et al., 2014; Vaquette, et al., 2012) demonstrate, a porosity with multiple length scales can both give biomechanical stability to the structure and make the scaffold highly biomimetic. Indeed, cell-cell and cell-ECM interactions occur on nano-scale and consequently the nanofibers produced by using the electrospinning technique, with diameter sizes ranging from tens of nanometres to micrometres, represent a physiological environment for skin cells. In addition, the small porosity of electrospun fibrous webs allows the drainage of the wound exudate, the gaseous exchange, the moist environment control and represents a filter against the microbial infections. On the other hand, the scaffold fabricated with 3D Bioplotter, provides a hard compartment which supports the tissue formation by promoting the vascularisation and by allowing the three-dimensional migration of dermal and epidermal cells through the macro-porosity. The main advantages of using an additive manufacturing technique in combination with electrospinning are the better control of geometry and interconnectivity of porosity and a higher mechanical stability. In addition, the 3D-printing technique allows to optimise the stiffness of the construct and precisely replicate the anatomy/form of the defect area through the CAD model. Definitively, this semi-permeable scaffold, with the nanofeatures in contact with the wounded tissue and the hard support which grants the neovascularization, can constitute a smart strategy for the skin regeneration.

The responsive aspect of the wound dressing has been reproduced by adding piezoelectric barium titanate nanoparticles into the structure. Some research groups have recently begun to investigate the effects of an electric field on the wound healing process (Messerli & Graham, 2011; Zhao, 2008; McCaig, 2005). These studies demonstrate that an electric stimulus can effectively promote the regeneration of skin because it reproduces the physiologic endogenous electric fields (EFs) that generate when an injury occurs.

Indeed, as reported in literature, the potential gradients developed between the site of the wound and the surrounding non-wounded tissue, can activate signaling pathways that guide cell migration. The study of Bhang et al. is one of the few examples in literature relative to piezoelectric scaffold for wound healing application (Bhang, et al., 2017). The present work is based on the same principle consisting in the use of piezoelectric nanomaterials that can generate EFs even under small mechanical deformations, thus avoiding the use of subsidiary and external electrical devices to induce EFs. However, the innovative aspect of the wound dressing designed in this thesis is the incorporation of $BaTiO_3$ nanoparticles both into the electrospun nanofibers and into the printed scaffold with concentrations up to 250 mg/ml and 500 mg/ml (of polymer solution), respectively.

The PLA-based solutions could be Electrospun more easily than PCL-based solutions. Indeed, the optimised protocol to electrospin PLA fibers was available (Zhang, et al., 2017) and only one concentration of PLA was needed to try, in order to produce defect-free fibers. The images of PLA nanofibers obtained by SEM analyses were compared with those produced by the research group of Elisa Mele, Wanwei Zhang and other collaborators at the Materials Department of Loughborough University (Zhang, et al., 2017).

On the contrary, several tests were performed to achieve the optimised concentration of PCL and type of solvent that allowed to fabricate defect-free nanofibers with almost uniform and small diameter sizes (hundreds of nanometres). However, once the $BaTiO_3$ nanoparticles were added to the solutions, PCL-based dispersions resulted more suitable for electrospinning than PLA-based dispersions. The morphology of PCL/BTNPs fibrous mats was preserved and superficial defects did not appear even with high particles loads. On the other hand, the PLA/BTNPs-based dispersions produced fibers with beads and break points. For this reason, PCL nanofibers with 150 mg/ml and 250 mg/ml of BTNPs have been chosen to fabricate the composite final scaffold. The maximum concentration of $BaTiO_3$ that has been achieved in this work is definitely high if compared to other concentrations of particles inside PCL electrospun nanofibers (Erisken, et al., 2008; Yang, et al., 2009; Patlolla, et al., 2010).

The PCL/BTNPs 3D-printed scaffold, fabricated in this thesis work, has a less regular porosity geometry than the PCL scaffold geometry (Figure 9.6). This is due to the presence of nanoparticles which require the solvent and a low temperature process, different from that used for non-piezoelectric scaffolds, as discussed in Chapter 9.

However, by comparing the images obtained with the inverted optical microscope to data in literature, it was found that the shape of pores of PCL scaffolds rarely remains perfectly regular (La, et al., 2016; Maurmann, et al., 2017).

The same procedure used in this work to fabricate the composite scaffold has been performed by a Brazilian research group. They produced 3D PCL matrices through a 3D printing process that were successively covered by electrospun PLGA to improve cell attachment (Maurmann, et al., 2017). As for the cited study, also in this work it was not necessary to add an adhesive (like gelatine) between the fibers and the scaffold. Indeed, the fibers remain attached to the substrate even if subjected to a mechanical stretch.

The WST-1 and alamarBlue assays that have been performed, demonstrate that the substrates with the major number of living cells include the control, the fibrous mats and the composite scaffolds. The cell viability on PCL0 and PCL500 scaffolds is inferior respect with the other samples. This result confirms the beneficial effects of nanofibers that improve the cells attachment and proliferation on the 3D-printed scaffolds.

Fluorescence images also show that the substrates with more adhered cells are the nanofibrous mats and the composites. SaOS-2 cells appear spread and elongated on the surface, a behaviour that indicates the formation of mature focal adhesions between the cells and the substrate. The 3T3 fibroblasts develop less cytoplasmic protrusions than SaOS-2 and appear with a rounded morphology which could suggest the unsuitableness of substrates. However, the images obtained in this project reflect the data found in literature: NIH 3T3 fibroblasts remain with a rounded-shape even during the cellular spreading phase (Merkle, et al., 2014).

The calcium imaging experiment and the US stimulation, which were performed to evaluate the effectiveness of the piezoelectric composite scaffolds, demonstrate that 3T3 fibroblasts respond differently depending on the substrate type. The fluorescence intensity measured in cells seeded on the piezoelectric composite substrate increases when the ultrasounds stimulation starts. On the contrary, the calcium activity in cells seeded on the control remains almost constant. Although it is a promising result, further analyses are necessary in order to test the effects of electric stimuli on fibroblasts proliferation and migration.

Conclusion

The present thesis project involved the design and fabrication of advanced wound dressings for the treatment of chronic wounds. To this aim the combination of a conventional scaffolding technique with an additive manufacturing technology has been used. The results obtained demonstrate that polycaprolactone (PCL) could represent the suitable material for producing piezoelectric scaffolds. Indeed, the high elongation at break typical of this polymer allows to load elevated concentrations of barium titanate nanoparticles (BTNPs) into the electrospun fibers. The innovative aspect of this study is the integration of the piezoelectric particles both into the electrospun nanofibers and into the 3D-printed scaffold resulting in the amplification of the electric signal. Moreover, the combination of electrospinning and 3D-Bioplotting generates a hierarchical scaffold with porosity over multiple length scales. Cell viability that has been analysed for this piezoelectric composite scaffold indicates that it represents an appropriate substrate for adhesion, growth and proliferation of 3T3 and SaOS-2 cells. The number of living cells on composites is comparable with that on the nanofibrous mats and higher than the number of living cells on the fibers-free 3D-printed scaffolds. This result confirms the positive influence of nanofeatures on the cell attachment. On the other hand, the use of an additive manufacturing technique allows to obtain a better control of geometry and interconnectivity of porosity and a higher mechanical stability. In addition, the 3D printing technique can precisely replicate the anatomy/form of the defect area through the CAD model. The effectiveness of this piezoelectric composite scaffold has been demonstrated by the response of fibroblasts to a wireless and non-invasive electric stimulus. The future perspectives could include a detailed analysis to test the effects of electric stimuli on fibroblasts proliferation and growth. The influence of electric fields on the skin cells migration and consequently on the wound healing process, could be investigated by orienting the mechanical solicitation. A unidirectional mechanical stretch could be applied to verify the activation of signaling pathways into the cells, responsible of cell migration. In addition, a precise mechanical characterization and a study of the degradation are needed to complete the analysis on the behaviour of these hierarchical scaffolds in a wound site.

To conclude, this biomimetic and responsive wound dressing represents an interesting and promising start point for the development of a scaffold that can consistently improve the healing of chronic wounds.

References

Abedalwafa, M., Wang, F., Wang , L. & Li, C., 2013. Biodegradable poly-epsilon-caprolactone (pcl) for tissue engineering applications: a review. *Rev. Adv. Mat. Sci.,* Volume 34, pp. 123-140.

Abrigo, M., McArthur, S. L. & Kingshott, P., 2014. Electrospun Nanofibers as Dressings for Chronic Wound Care: Advances, Challenges, and Future Prospects. *Macromolecular Bioscience,* Volume 14, pp. 772-792.

Acosta, J. B., 2008. The pro-inflammatory environment in recalcitrant diabetic foot wounds. *Int Wound J.,* Volume 5, pp. 530-539.

Agren, M. S., 2016. *Wound Healing Biomaterials.* Duxford, UK: Woodhead publishing.

Aguilar, M. R. & San Roman, J., 2014. Introduction to smart polymers and their applications. In: M. R. Aguilar & J. San Roman, eds. *Smart Polymers and their Application.* s.l.:Woodhead Publishing Limited, pp. 1-11.

Amir, O., Liu, A. & Chang, A. L., 2012. Stratification of Highest-Risk Patients with Chronic Skin Ulcers in a Stanford Retrospective Cohort Includes Diabetes, Need for Systemic Antibiotics, and Albumin Levels. *Hindawi Publishing Corporation,* pp. 1-8.

Anastasi, G., Capitani, S. & Carnazza, M. L., 2006. *Trattato di anatomia umana.* 4 ed. Milan: Edi.Ermes.

Aramwit, P., 2016. Introduction to biomaterials for wound healing. In: M. S. Agren, ed. *Wound Healing Biomaterials.* Duxton: Elsevier, pp. 4-38.

Ausprunk, D. H. & Folkman, J., 1977. Migration and proliferation of endothelial cells in pre-formed and newly formed blood vessels during tumor angiogenesis. *Microvasc Res,* 14(1), pp. 53-65.

Balaji, A. et al., 2015. An insight on electrospun-nanofibers-inspired modern drug delivery system in the treatment of deadly cancers. *RSC Advances,* Volume 8, pp. 57984-58004.

Barker, A. T., Jaffe, L. F. & Vanable, J. W., 1982. The glabrous epidermis of cavies contains a powerful battery. *Am. J. Physiol. Regul. Integr. Comp. Physiol.,* Volume 242, pp. 358-366.

Basu, P., Kumar, N. & Manjubala, I., 2017. Wound healing materials – a perspective for skin tissue engineering. *CURRENT SCIENCE,* Volume 112, pp. 2392-2404.

Bhang, S. H. et al., 2017. Zinc Oxide Nanorod-Based Piezoelectric Dermal Patch for Wound Healing. *Advanced Science News,* Volume 27, pp. 1-13.

Bhardwaj, N. & Kundu, S. C., 2010. Electrospinning: A fascinating fiber fabrication technique. *Biotechnology Advances,* Volume 28, pp. 325-347.

Bhattarai, S. R. et al., 2004. *Biomaterials.* s.l.:s.n.

Bloom, H., 1945. "Cellophane" dressing for second-degree burns. *The Lancet,* Volume 246, p. 559.

Boateng, J. S., Matthews, K. H., Stevens , H. N. & Eccleston, G. M., 2008. Wound Healing Dressings and Drug Delivery Systems: A Review.. *Indian J Pharml Sci,* Volume 97, pp. 2892-2923.

Bolognia , J., Rapini, R. P. & Jorizzo, J. L., 2003. *Dermatology.* University of Chicago: Mosby.

Boughton, E. & Mclennan, S., 2013. Biomimetic scaffolds for skin tissue and wound repair. In: *Biomimetic biomaterials. Structure and applications.* Sydney: Woodhead Publishing Limited, pp. 153-80.

Breitkreutz, D., Mirancea, N. & Nischt, R., 2009. Basement membranes in skin: unique matrix structures with diverse functions?. *Histochem Cell Biol,* Volume 132, pp. 1-10.

Broughton, G., Janis, J. E. & Attinger, C. E., 2006. The basic science of wound healing. *Plast Reconstr Surg,* Volume 117, pp. 12S-34.

Burcu, E., 2013. The Overview of The Electrical Properties of Barium Titanate. *American Journal of Engineering Research (AJER),* Volume 2, pp. 1-7.

Candia, O. A., 2004. Electrolyte and fluid transport across corneal, conjunctival and lens epithelia. *Exp Eye Res,* Volume 78, pp. 527-535.

Cao, H., Liu, T. & Chew, S. Y., 2009. The application of nanofibrous scaffolds in neural tissue engineering. *Advanced Drug Delivery Reviews,* Volume 61, pp. 1055-1064.

Chan, B. P. & Leong, K. W., 2008. Scaffolding in tissue engineering: general approaches and tissue-specific considerations. *Eur Spine J,* Volume 17, pp. 467-479.

Chen, C., Corbley, M. J., Roberts, T. M. & Hess, P., 2015. Voltage-Sensitive Calcium Channels in Normal and Transformed 3T3 Fibroblasts. *Science,* Volume 239, pp. 1024-1026.

Chen, J. P., Kuo, C. Y. & Lee, W. L., 2012. Thermo-responsive wound dressings by grafting chitosan and poly(N-isopropylacrylamide) to plasma-induced graft polymerization modified non-woven fabrics. *Applied Surface Science,* Volume 262, pp. 95-101.

Chu, P. K., Chen, J. Y. & Huang, N., 2002. Plasma-surface modification of biomaterials. *Materials Science and Engineering: Reports,* Volume 36, pp. 143-206.

Ciofani, G. et al., 2010. Enhancement of neurite outgrowth in neuronal-like cells following boron nitride nanotube-mediated stimulation. *ACS Nano,* Volume 4, pp. 6267-6277.

Clark, R. A., 1988. Overview and general considerations of wound repair. In: *The molecular and cellular biology of wound repair.* New York: Plenum Press, pp. 3-50.

Comby, S., Imbert, D., Vandevyver, C. D. & Bünzli, J. G., 2007. A Novel Strategy for the Design of 8-Hydroxyquinolinate-Based Lanthanide Bioprobes That Emit in the Near Infrared Range. *Chemistry,* Volume 13, pp. 936-944.

Cooper, J. A., 1987. Effects of cytochalasin and phalloidin on actin. *J. Cell Biol.,* Volume 105, pp. 1473-1478.

Daunton , C., Kothari , S., Smith , L. & Steele, D., 2012. A history of materials and practices for wound management. *Wound Pract Res,* Volume 20, pp. 174-186.

Dawson , D. & N., C., 2014. *The Integumentary System (The Skin).* [Online]
Available at: http://healthsciencetechnology.wikispaces.com/5th+integumentary+system
[Accessed 07 01 2018].

De Donatis, A., Ranaldi, F. & Cirri, P., 2010. Reciprocal control of cell proliferation and migration. *Cell Communication and Signaling,* Volume 8, pp. 1-4.

Degreef, H., 1998. How to heal a wound fast. *Dermatol Clin,* Volume 16, pp. 365-375.

Deng , J., Li, P. Y. & Cheng, H., 2017. Advances of smart materials for wound healing. In: Q. Wang, ed. *Smart Materials for Tissue Engineering: Applications.* s.l.:Royal Society of Chemistry, p. 692.

Dhivya, S., Padma, V. V. & Santhini, E., 2015. Wound dressings – a review. *BioMedicine,* Volume 5, pp. 24-28.

Diegelmann, R. F., Rothkopf, L. C. & Cohen, I. K., 1975. Measurement of collagen biosynthesis during wound healing. *J Surg Res,* 19(4), pp. 239-243.

Do, A., Khorsand, B., Geary, S. M. & Salem, A. K., 2015. 3D Printing of Scaffolds for Tissue Regeneration Applications. *Advanced Healthcare Materials,* Volume 4, pp. 1742-1762.

Doillon, C. J., 1985. Collagen fiber formation in repair tissue: development of strength and toughness. *Coll Relat Res,* 5(6), pp. 481-492.

Eaglstein, W. H. & Falanga, V., 1997. Chronic wounds. *Surg Clin North Am,* Volume 77, pp. 689-700.

Esumi, H. et al., 2002. Hypoxia and Nitric Oxide Treatment Confer Tolerance to Glucose Starvation in a 5'-AMP-activated Protein Kinase-dependent Manner. *J Biol Chem,* Volume 277, pp. 32791-32799.

Farah, S., Anderson, D. G. & Langer, R., 2016. Physical and mechanical properties of PLA, and their functions in widespread applications — A comprehensive review. *Advanced Drug Delivery Reviews,* Volume 107, pp. 367-392.

Fee, T. et al., 2016. Cell Orientation and Cytoskeletal Gene Expression on Electrospun PCL+Gelatin Nanofibers. *Plos One,* Volume 11, pp. 1-12.

Forrest, L., 1983. Current concepts in soft connective tissue wound healing. *Br J Surg,* 70(3), pp. 133-140.

Foulds, I. S. & Barker, A., 1983. Human skin battery potentials and their possible role in wound healing. *Br J Dermatol,* Volume 109, pp. 515-522.

Friedman, P. A. & Gesek, F. A., 1995. Cellular calcium transport in renal epithelia: measurement, mechanisms, and regulation. *Physiol Rev,* Volume 75, pp. 429-471.

Gabriel, A., 2016. *Medscape. Vascular Ulcers.* [Online]
Available at: https://emedicine.medscape.com/article/1298345-overview#a8

Gambetti, 2016. *MEDIUM BENCH-TOP PLASMA SYSTEM – TUCANO.* [Online]
Available at: http://www.plasmi.eu/index.php?url=tucano-reattore-al-plasma-medio

Gates, J. L. & Holloway, G. A., 1992. A comparison of wound environments. *Ostomy Wound Manage,* Volume 38, pp. 34-37.

Gatford, J., 2008. *The New Zealand Institute for Plant and Food Research Ltd.* [Online]
Available at: https://www.plantandfood.co.nz/

Geetha, M., 2017. Mechanical characterization of nanofiber composites. In: M. Ramalingam & S. Ramakrishna, eds. *Nanofiber Composites for Biomedical Applications.* Duxford (UK): Elsevier, pp. 116-155.

Genchi, G. G. et al., 2016. P(VDF-TrFE)/BaTiO3 Nanoparticle Composite Films Mediate Piezoelectric Stimulation and Promote Differentiation of SH-SY5Y Neuroblastoma Cells. *Adv. Healthc Mater.,* Volume 5, pp. 1808-1820.

Giannitelli, S. M., Mozetic, P., Trombetta, M. & Rainer, A., 2015. Combined additive manufacturing approaches in tissue engineering. *Acta Biomaterialia,* Volume 24, pp. 1-11.

Gurtner, G. C., Werner, S., Barrandon, Y. & Longaker, M. T., 2008. Wound repair and regeneration. *Nature,* Volume 453, pp. 314-321.

Haider, A., Haider, S. & Kang, I., 2015. A comprehensive review summarizing the effectof electrospinning parameters and potentialapplications of nanofibers in biomedicaland biotechnolog. *Arabian Journal of Chemistry,* Volume 17, pp. 1-24.

Hajiali, F., Tajbakhsh, S. & Shojaei, A., 2017. Fabrication and Properties of Polycaprolactone Composites Containing Calcium Phosphate-Based Ceramics and Bioactive Glasses in Bone Tissue Engineering: A Review. *Polymer Reviews,* Volume 9, pp. 1-41.

Holzapfel, B. M. et al., 2013. How smart do biomaterials need to be? A translational science and clinical point of view. *Adv. Drug Deliv. Rev.,* Volume 65, pp. 581-603.

Huang, Z. M., Zhang, Y. Z., Ramakrishna, S. & Lim, C. T., 2004. Electrospinning and mechanical characterization of gelatin nanofibers. *Polymer,* Volume 45, pp. 5361-5368.

Jiang, H., Zhao, P. & Zhu, K., 2007. Fabrication and characterization of zein-based nanofibrous scaffolds by an electrospinning method. *Macromolecular Bioscience,* Volume 7, pp. 517-525.

Jiang, S., Lv, L. P., Landfester, K. & Crespy, D., 2016. Nanocontainers in and onto nanofibers. *Accounts of Chemical Research,* Volume 49, pp. 816-823.

Johnson, F. R. & McMinn, R. M., 1960. The cytology of wound healing of body surfaces in mammals. *Biol Rev Camb Philos Soc,* 35(3), pp. 364-410.

Khanna, S., 2010. Macrophage dysfunction impairs resolution of inflammation in the wounds of diabetic mice. *PLoS One.,* Volume 5, p. e9539.

Koh , T. J. & DiPietro, L. A., 2013. Inflammation and wound healing: The role of the macrophage. *Expert Rev Mol Med,* Volume 13, p. e23.

Kriegel, C. et al., 2008. Fabrication, functionalization, and application of electrospun biopolymer nanofibers. *Critical Reviews in Food Science and Nutrition,* Volume 48, pp. 775-797.

Kumar, S. & Leaper, D. J., 2007. Classification and management of acute wounds. *Surgery,* Volume 26, pp. 43-47.

Kurkinen, M., 1980. Sequential appearance of fibronectin and collagen in experimental granulation tissue. *Lab Invest,* 43(1), pp. 47-51.

Labet, M. & Thielmans, W., 2009. Synthesis of polycaprolactone: a review. *Chemical Society Reviews,* Volume 38, pp. 3484-3504.

Lancaster, M. V. & Fields, R. D., 1996. *Antibiotic and Cytotoxic Drug Susceptibility Assays using Resazurin and Poising Agents.* US, Patent No. 5,501,959 .

Latt, S. A. et al., 1975. Recent developments in the detection of deoxyribonucleic acid synthesis by 33258 Hoechst fluorescence. *Journal of Histochemistry and Cytochemistry,* Volume 23, pp. 493-505.

Laudenslager, M. J. & Sigmund, W. M., 2012. “Electrospinning” Encyclopedia of Nanotechnology. *Springer Publishers,* pp. 769-775.

La, W. et al., 2016. Systemically replicated organic and inorganic bony microenvironment for new bone formation generated by a 3D printing technology. *The Royal Society of Chemistry,* Volume 6, pp. 11546-11553.

Leibiger, C. et al., 2013. First Molecular Cytogenetic High Resolution Characterization of the NIH 3T3 Cell Line by Murine Multicolor Banding. *J Histochem Cytochem,* Volume 61, pp. 306-312.

Levenson, S. M., 1965. The healing of rat skin wounds. *Ann Surg,* Volume 161, pp. 293-308.

Levin, M. H., Kim, J. K., Hu, J. & Verkman, A. S., 2006. Potential difference measurements of ocular surface Na+ absorption analyzed using an electrokinetic model. *Invest Ophthalmol Vis Sci,* Volume 47, pp. 306-316.

Lippert-Gruner, M., 2003. Gluteal neuromuscular stimulation in therapy and prophylaxis of recurrent sacral pressure ulcers. *Spinal Cord,* Volume 41, pp. 365-366.

Liu, G. et al., 2017. Electrospun starch nanofibers: Recent advances, challenges, and strategies for potential pharmaceutical applications. *Journal of Controlled Release,* Volume 252, pp. 95-107.

Liu, L. et al., 2017. A pH-Indicating Colorimetric Tough Hydrogel Patch towards Applications in a Substrate for Smart Wound Dressings. *polymers,* Volume 9, pp. 1-15.

Liu, M. et al., 2017. Electrospun nanofibers for wound healing. *Materials Science and Engineering,* Volume 76, pp. 1413-1423.

Liu, Y. et al., 2013. Self-assembling peptide reduces glial scarring, attenuates post-traumatic inflammation and promotes neurological recovery following spinal cord injury. *Acta Biomater,* Volume 9, pp. 8075-8088.

Loh, Q. L. & Choong, C., 2013. Three-Dimensional Scaffolds: for Tissue Engineering Applications. In: *TISSUE ENGINEERING: Part B.* Singapore: Mary Ann Liebert, Inc, pp. 485-502.

Lovvorn, H. N., 1999. Relative distribution and crosslinking of collagen distinguish fetal from adult sheep wound repair. *J. Pediatr. Surg.,* Volume 34, pp. 218-223.

Lynen, F. & Wieland, U., 1937. Uber die Giftstoffe des Knollenblätterpilzes. IV. *Justus Liebigs Annalen der Chemie ,* Volume 533, pp. 93-117.

Lynn, D. E., 2009. Cell Culture. In: *Encyclopedia of Insects (Second Edition).* s.l.:s.n., pp. 144-145.

Madden, J. W. & Peacock Jr, E., 1968. Studies on the biology of collagen during wound healing. I. Rate of collagen synthesis and deposition in cutaneous wounds of the rat.. *Surgery,* 64(1), pp. 288-294.

Manoukian, O. S., 2016. Bioactive nanofiber dressings for wound healing. In: M. S. Agres, ed. *Wound Healing Biomaterials.* Duxford, UK: Elsevier, pp. 451-481.

Marcia, R. E. & Castro, M. C., 2002. New dressings, including tissue engineered living skin. *Clin Dermatol,* Volume 20, pp. 715-723.

Marino, A. et al., 2015. Piezoelectric Nanoparticle-Assisted Wireless Neuronal Stimulation. *ACS Nano,* Volume 9, pp. 7678-7689.

Martin, L., Wilson, C. G. & Koosha, F., 2002. The release of model macromolecules may be controlled by the hydrophobicity of palmitoyl glycol chitosan hydrogels. *J Control Release,* Volume 80, pp. 87-100.

Matabola, K. P. & Moutloali, R. M., 2013. The influence of electrospinning parameters on the morphology and diameter of poly (vinyledene fluoride) nanofibers-effect of sodium chloride. *Journal of Materials Science,* Volume 48, p. 5475.

Maurmann, N. et al., 2017. Mesenchymal stem cells cultivated on scaffolds formed by 3D printed PCL matrices, coated with PLGA electrospun nanofibers for use in tissue engineering. *Biomedical Physics & Engineering Express,* Volume 3, pp. 1-15.

McCaig, C. D., 2005. Controlling Cell Behavior Electrically: Current Views and Future Potential. *Physiol Rev,* Volume 85, pp. 943-978.

McGrath, J. A., Eady, R. A. & Pope, F. M., 2004. *Rook's Textbook of Dermatology.* Manchester: Blackwell Publishing.

McKeehan, W. L., McKeehan, K. A., Hammond , S. L. & Ham, R. G., 1977. Improved medium for clonal growth of human diploid fibroblasts at low concentrations of serum protein. *In Vitro,* Volume 13, pp. 399-416.

McNaught, A. D. & Wilkinson, A., 2014. *IUPAC. Compendium of Chemical Terminology, 2nd ed. (the "Gold Book"), Blackwell Scientific Publications, 2006.* [Online]
Available at: http://goldbook.iupac.org/html/B/B00626.html

Megelski S., Stephens, J. S., Chase, D. B. & Rabolt, J. F., 2002. Micro-and nanostructured surface morphology on electrospun polymer fibers. *Macromolecules,* Volume 35, pp. 8456-8466.

Meikle, S. T., 2016. Silver-doped hydrogels for wound dressings. In: M. S. Agren, ed. *Wound Healing Biomaterials.* Duxford, UK: Elsevier, pp. 335-351.

Merkle, V. M., Zeng, L., Slepian, M. J. & Wu, X., 2014. Core-Shell Nanofibers: Integrating the Bioactivity of Gelatin and the Mechanical Property of Polyvinyl Alcohol. *Biopolymers,* Volume 101, pp. 77-87.

Messerli, M. A. & Graham, D. M., 2011. Extracellular Electrical Fields Direct Wound Healing and Regeneration. *Biol. Bull.,* Volume 221, pp. 79-92.

Mitry, R. R. & Hughes, R. D., 2012. Supplies techniques that can be adapted to obtain cell cultures from diseased cells to gain understanding of the pathogenic mechanisms involved. In: *Human Cell Culture Protocols.* s.l.:s.n., p. 435.

Mocharla, R., Mocharla, H. & Hodes, M. E., 1987. A novel, sensitive fluorometric staining technique for the detection of DNA in RNA preparations. *Nucleic Acids Research,* Volume 15, p. 10589.

Mohanty, S., 2015. Fabrication of scalable and structured tissue engineering scaffolds using water dissolvable sacrificial 3D printed moulds. *Materials Science and Engineering C,* pp. 569-578.

Moor, Z. & Cowman, S., 2008. Repositioning for treating pressure ulcers (Protocol). *The Cochrane Library,* Volume 1, pp. 1-10.

Moroni, L., De Wijn, J. & Van Blitterswijk, C., 2008. Integrating novel technologies to fabricate smart scaffolds. *J. Biomater. Sci. Polym. Ed.,* Volume 19, pp. 543-572.

Moroni, L. et al., 2013. Plug and play: combining materials and technologies to improve bone regenerative strategies. *J Tissue Eng Regen Med ,* Volume 9, pp. 745-759.

Murphy, S. V. & Atala, A., 2014. 3D bioprinting of tissues and organs. *nature biotechnology,* Volume 32, pp. 773-785.

Naimer, S. A. & Chemla, F., 2000. Elastic adhesive dressing treatment of bleeding wounds in trauma victims. *Am. J. Emerg. Med.,* Volume 18, pp. 816-819.

Nakamura, M. et al., 2010. Biomatrices and biomaterials for future developments of bioprinting and biofabrication. *Biofabrication,* Volume 2, pp. 1-6.

Nathoo, R., Howe, N. & Cohen, G., 2014. Skin Substitutes An Overview of the Key Players in Wound Management. *J Clin Aesthet Dermatol.,* Volume 4, pp. 44-48.

Nelson, D. L., Lehninger, A. L. & Cox, M. M., 2008. *Lehninger principles of biochemistry.* 5th ed. New York: W.H. Freeman.

Oyedotun, K. S. & Lemire, B. D., 2004. The quaternary structure of the Saccharomyces cerevisiae succinate dehydrogenase. Homology modeling, cofactor docking, and molecular dynamics simulation studies. *he Journal of Biological Chemistry,* Volume 279, pp. 9424-9431.

Parani, M., Lokhande, G., Singh, A. & Gaharwar, A. K., 2016. Engineered Nanomaterials for Infection Control and Healing Acute and Chronic Wounds. *ACS Applied Material Interfaces,* Volume 8, pp. 10049-10069.

Pelipenko, J. et al., 2012. Interfacial rheology: an overview of measuring techniques and its role in dispersions and electrospinning. *Acta Pharmaceutica,* Volume 62, pp. 123-140.

Pelipenko, J. et al., 2013. The impact of relative humidity during electrospinning on the morphology and mechanical properties of nanofibers. *International Journal of Pharmaceutics,* Volume 456, pp. 125-134.

Peltola, S. M., Melchels, F. P., Grijpma, D. W. & Kellomäki, M., 2008. A review of rapid prototyping techniques for tissue engineering purposes. *Ann Med,* Volume 40, pp. 268-280.

Peterson, J. M. et al., 1987. Significance of T-lymphocytes in wound healing. *Surgery,* Volume 102, pp. 846-852.

Philippeos, C., Hughes , R. D., Dhawan, A. & Mitry, R. R., 2012. Introduction to cell culture. *Methods of Molecular Biology,* Volume 806, pp. 1-13.

Pieper , B., Langemo, D. & Cuddigan, J., 2009. Pressure ulcer pain: a systematic literature review and national pressure ulcer advisory panel white paper. *Ostomy Wound Manag,* 55(2), pp. 16-31.

Pillay, V. et al., 2013. A review of the effect of processing variables on the fabrication of electrospun nanofibers for drug delivery applications. *Journal of Nanomaterials,* Volume 2013, p. 22.

Polverini, P. J., 1977. Activeted macrophages include vascular proliferation. *Nature,* 269(5631), pp. 804-806.

Proksch, E., Brandner, J. M. & Jensen, J., 2008. The skin: an indispensable barrier. *Blackwell Munksgaard, Experimental Dermatology,* Volume 17, pp. 1063-1072.

Puppi, D. et al., 2014. Nano/microfibrous polymeric constructs loaded with bioactive agents and designed for tissue engineering applications: a review. *J. Biomed. Mater. Res. B,* Volume 102, pp. 1562-1579.

Qing, C., 2017. The molecular biology in wound healing & non-healing wound. *Chinese Journal of Traumatology,* Volume 20, pp. 189-193.

Qi, S. & Craig, D., 2016. Recent developments in micro-and nanofabrication techniques for the preparation of amorphous pharmaceutical dosage forms. *Advanced Drug Delivery Reviews,* Volume 100, pp. 67-84.

Ratner, B. D., Hoffman, A. S., Schoen, F. J. & Lemons, J. E., 1996. *Biomaterial Science: An Introduction to Materials in Medicine.* s.l.:Accademic Press.

Reichman, D. E. & Greenberg, J. A., 2009. Reducing surgical site infections: a review. *Rev Obset Gynecol,* 2(4), pp. 212-21.

Remensnyder, J. P. & Majno, G., 1968. Oxygen gradients in healing wounds. *Am J Pathol,* 52(2), pp. 301-323.

Reneker, D. H. & Hou, H., 2004. Electrospinning. In: *Encyclopedia of biomaterials and biomedical engineering.* s.l.:Taylor and Francis Group, pp. 543-550.

Reneker, D. H. & Yarin, A. L., 2008. Electrospinning jets and polymer nanofibers. *Polymer,* Volume 49, pp. 2387-2425.

Robson, M. C. & Steed, D. L., 2001. Wound Healing: Biologic Features and Approaches to Maximize Healing Trajectories. *Current Problems in Surgery,* 38(2), pp. 71-141.

Rogina, A., 2014. Electrospinning process: Versatile preparation method for biodegradable and natural polymers and biocomposite systems applied in tissue engineering and drug delivery. *Applied Surface Science,* Volume 296, pp. 221-230.

Rosic, R. et al., 2013. Nanofibers and their biomedical use. *Acta Pharmaceutica,* Volume 63, pp. 295-304.

Ross , R. & Benditt, E. P., 1961. Wound healing and collagen formation: I. Sequential changes in components of guinea pig skin wounds observed in the electrone microscope. *J Biophys Biochem Cytol,* Volume 11, pp. 677-700.

Schmitt-Graff, A., 1994. Heterogenity of myofibtoblast phenotypic features: an example of fibroblastic cell plasticity. *Vichows Archiv,* 425(1), pp. 3-24.

Sen, C. K., 2009. Human skin wounds: A major and snowballing threat to public health and the economy. *Wounds Repair and Regeneration,* Volume 17, pp. 763-771.

Sezer, A. & Cevher, E., 2011. Biopolymers as wound healing materials: challenges and new strategies. In: R. Pignatello, ed. *Biomaterials Applications for Nanomedicine.* s.l.:InTech, pp. 383-414.

Sheridan, R. L. & Tompkins, R. G., 1999. Skin substitutes in burns. *Burns ,* Volume 25, pp. 97-103.

Shu, Y. C. & Bhattacharya, K., 2001. Domain patterns and macroscopic behaviour of ferroelectric materials. *Philosophical Magazine B,* Volume 81, pp. 2021-2054.

Sill, T. J. & von Recum, H. A., 2008. Electrospinning: applications in drug delivery and tissue engineering. *Biomaterials,* Volume 29, pp. 1989-2006.

Simpson, D. M. & Ross, R., 1972. The neutrophilic leukocyte in wound repair. A study with antineutrophil serum. *J Clin Invest,* 51(8), pp. 2009-2023.

Sindrilaru, A., 2011. An unrestrained proinflammatory M1 macrophage population induced by iron impairs wound healing in humans and mice. *J Clin Invest.,* Volume 121, pp. 985-997.

Singer, A. J., Hollander, J. E. & Quinn, J. V., 1997. Evaluation and management of traumatic lacerations. *N Engl J Med,* 16(8), pp. 337-1142.

Singh, S., Young, A. & McNaught, C. E., 2017. The physiology of wound healing. *Surgery,* 35(9), pp. 473-477.

Sujatha , S., 2012. Recent advances in topical wound care. *Indian J Plast Surg,* Volume 45, pp. 379-387.

Sun, B. et al., 2014. Advances in three-dimensional nanofibrous macrostructures via electrospinning. *Progress in Polymer Science,* Volume 39, pp. 862-890.

Swezey, L., 2010. *WoundEducator.com.* [Online]
Available at: https://woundeducators.com/interactive-wound-dressings/
[Accessed 2018 01 14].

Tejiram, S., Kavalukas, S. L., Shupp, J. W. & Barbul, A., 2016. Wound Healing. In: *Wound Healing Biomaterials.* Duxford: Elsevier, pp. 3-12.

Tew, C., 2014. Recurring pressure ulcers: identifying the definitions. A National Pressure Ulcer Advisory Panel white paper. *Wound Repair Regen,* 22(3), pp. 301-304.

Than, P. A., Davis, C. R. & Gurtner, G. C., 2016. Clinical Management of Wound Healing and Hypertrophic Scarring. In: M. Z. Albanna & J. H. Holmes IV, eds. *Skin Tissue Engineering an Regenerative Medicine.* Medical Center Boulevard Winston-Salem, NC, USA: Elsevier, pp. 61-82.

Thenmozhi, S., Dharmaraj, N., Kadirvelu, K. & Kim, H. J., 2017. Electrospun nanofibers: New generation materials for advanced applications. *Materials Science and Engineering B,* Volume 217, pp. 36-48.

Thomas, S., 2010. *Surgical Dressing and Wound Management.* Peterborough: Medetec Publishing.

Van de Velde, K. & Kiekens, P., 2002. Biopolymers: overview of several properties and consequences on their applications. *Polymer Testing,* Volume 21, pp. 433-442.

Vanwijck, R., 2001. Surgical biology of wound healing. *Bull Mem Acad R Med Belg,* Volume 115, pp. 175-184.

Vaquette, C. et al., 2012. A biphasic scaffold design combined with cell sheet technology for simultaneous regeneration of alveolar bone/periodontal ligament complex. *Biomaterials,* Volume 33, pp. 5560-5573.

Velnar, T., Bailey, T. & Smrkolj, V., 2009. The Wound Healing Process: an Overview of the Cellular and Molecular Mechanisms. *The Journal of International Medical Research,* Volume 37, pp. 1528-1542.

Vijatović, M. M., Bobić, J. D. & Stojanović , B. D., 2008. History and Challenges of Barium Titanate: Part II. *Science of Sintering,* Volume 40, pp. 235-244.

Volker, J. H., 2017. *Cells and layers of the epidermis.* [Online]
Available at: https://www.earthslab.com/physiology/cells-layers-epidermis/
[Accessed 07 01 2018].

Vowden, K. & Vowden, P., 2017. Wound dressings: principles and practice. *Surgery,* Volume 35, pp. 490-494.

Waheed, S. et al., 2016. 3D printed microfluidic devices: enablers and barriers. *Royal Society of Chemistry,* Volume 16, pp. 1993-2013.

Wang, Z. L. & Song, J., 2006. Science. Volume 312, p. 242.

Werner, S., Krieg, T. & Smola, H., 2007. Keratinocyte–fibroblast interactions in wound healing. *J. Invest. Dermatol.,* Volume 127, pp. 998-1008.

Whelan, D., Caplice, N. M. & Clover, A. J., 2014. Fibrin as a delivery sustem in wound healing tissue engineering applications. *Journal of Controlled Release,* Volume 196, pp. 1-8.

Wood, E. J. & Bladon, P. T., 1985. *The Human Skin.* London: Edward Arnold.

Wyszynski, M. et al., 2002. Interaction between GRIP and Liprin-alpha/SYD2 Is Required for AMPA Receptor Targeting. *Neuron,* Volume 34, pp. 39-52.

Yang, Q. et al., 2004. Influence of solvents on the formation of ultrathin uniform poly(vinyl pyrrolidone) nanofibers with electrospinning. *Journal of Polymer Science Part B: Polymer Physics,,* Volume 42, pp. 3721-3726.

Yao, C., Li, X. & Song, T., 2007. Electrospinning and crosslinking of zein nanofiber mats. *Journal of Applied Polymer Science,* Volume 103, pp. 380-385.

Zafar, M. et al., 2016. Potential of Electrospun Nanofibers for Biomedical and Dental Applications. *materials,* Volume 9, pp. 1-21.

Zahedi, P. et al., 2010. A review on wound dressings with an emphasis on electrospun nanofibrous polymeric bandages. *Polymers Advanced Technologies,* Volume 21, pp. 77-95.

Zamboni, P., 2006. The overlapping of local iron overload and HFE mutation in venous leg ulcer pathogenesis. *Free Radic Biol Med.,* Volume 40, pp. 1869-1873.

Zarbock, A., Polanowska-Grabowska , R. K. & Ley, K., 2007. Platelet-neutrophil-interactions: linking hemostasis and inflammation. *Blood Rev,* Volume 21, pp. 99-111.

Zhang, W. et al., 2017. Electrospinning of polylactic acid fibers containing tea tree and manuka oil. *Reactive and Functional Polymers,* Volume 117, pp. 106-111.

Zhang, Y., Lim, C. T., Ramakrishna, S. & Huang, Z. M., 2005. Recent development of polymer nanofibers for biomedical and biotechnological applications. *Journal of Materials Science,* Volume 16, pp. 933-946.

Zhao, M., 2008. Electrical fields in wound healing—An overriding signal that directs cell migration. *Seminars in Cell & Developmental Biology,* Volume 20, pp. 674-682.

Zhu, J., Zhang, Y., Shao, H. & Hu, X., 2008. Electrospinning and rheology of regenerated Bombyx mori silk fibrion aqueous solutions: The effect of pH and concentration. *olymer,* Volume 49, pp. 2880-2885.

Acknoledgements

Foremost, I would like to express my sincere gratitude to my advisor Prof. Gianni Ciofani, for giving me the opportunity to develop this project and to have followed it in every phase with professionalism and extreme availability.

I thank Prof. Elisa Mele for welcoming me to the research group of the Department of Materials Engineering at the University of Loughborough (UK). Thank you for patiently resolving any doubt and uncertainty and for being a competent guide during the whole thesis course. Among the wonderful people that I got to know during my experience abroad, I extend a special thanks to Giulia, Tom, Sara and Ollie who helped me both at work and in English life.

I have to reserve an important acknowledgement to Dr. Giada Graziana Genchi, for having shared with me a significant part of the project, at the Italian Institute of Technology (IIT) in Pontedera (Italy). Thank you for introducing me to the wide world of biology, assisting me with patience as I took my first steps. I thank Attilio, Matteo, Daniele and Christos for welcoming me as one of them in the IIT Smart Bio-Interfaces group.

I thank all the people who in recent years have shared with me the hardships and joys of my studies, from the primary school to university. Among these, I address a special thank you to my old friends Francesca, Galli and Marcella who represent a constant in my life and continue to support me even from afar.

I thank my family, who has given to me the insatiable desire for knowledge and the determination necessary to reach it. Thanks for being able to make the failures less bitter and have tasted with me the satisfactions.

I thank Stefano, who is sharing the joy of this goal. Thanks for being by my side making me a happy person.

I reserve an infinite thanks to my parents, to whom I dedicate this thesis, to give me the affection, the encouragement and the means necessary to achieve my goals. Thank you for teaching me not to give up and look forward with awareness and determination. Thank you for the trust you have shown me every day and for always being my light and my reference point.

Finally, I address a special thought to Prof. Paolo Cortese, who gave me the precious message that I brought with me during these years of Politecnico. Although it was a way full of satisfactions but also obstacles, I came to the goal savouring the emotions at every step.

Ringrazio innanzitutto il Prof. Gianni Ciofani, per avermi dato l'opportunità di sviluppare questo progetto e per averlo seguito in ogni sua fase con professionalità ed estrema disponibilità.
Ringrazio la Prof.ssa Elisa Mele per avermi accolta nel gruppo di ricerca del Dipartimento di Ingegneria dei Materiali presso l'Università di Loughborough (UK). Grazie per aver risolto pazientemente ogni dubbio e incertezza e per essere stata una guida competente durante tutto il percorso di tesi. Tra le meravigliose persone che ho avuto modo di conoscere durante l'esperienza all'estero, rivolgo un ringraziamento speciale a Giulia, Tom, Sara e Ollie che mi hanno aiutata sia sul lavoro che nella vita inglese.
Sento inoltre di dover riservare un riconoscimento importante alla Dott.ssa Giada Graziana Genchi, per aver condiviso con me una parte significativa del progetto, svoltasi presso l'Istituto Italiano di Tecnologia (IIT) di Pontedera. Grazie per avermi introdotta nell'immenso mondo della biologia, assistendomi con pazienza mentre muovevo i primi passi. Ringrazio Attilio, Matteo, Daniele e Christos per avermi accolta come una di loro nel gruppo Smart Bio-Interfaces dell'IIT.
Ringrazio tutte le persone che in questi anni hanno condiviso con me le fatiche e le gioie del mio percorso di studi, dai banchi della scuola elementare fino all'università. Tra questi, rivolgo un grazie speciale ai miei amici di sempre Francesca, Galli e Marcella che rappresentano una costante nella mia vita e continuano a sostenermi anche da lontano.
Ringrazio la mia famiglia, che mi ha trasmesso l'insaziabile desiderio di conoscenza e la risolutezza necessaria a raggiungerla. Grazie per aver saputo rendere meno amari gli insuccessi e aver assaporato con me le soddisfazioni.
Ringrazio Stefano, con il quale condivido la gioia di questo traguardo. Grazie per essere al mio fianco rendendomi una persona felice.
Riservo un ringraziamento infinito ai miei genitori, a cui dedico questa tesi, per fornirmi l'affetto, l'incoraggiamento e i mezzi necessari al conseguimento dei miei obiettivi. Grazie per avermi insegnato a non demordere e a guardare avanti con consapevolezza e determinazione. Grazie per la fiducia che mi dimostrate ogni giorno e per essere da sempre la mia luce e il mio riferimento.
Infine, rivolgo un pensiero speciale al Prof. Paolo Cortese, il quale mi ha consegnato il prezioso messaggio che ho portato con me in questi anni di Politecnico. Sebbene sia stato un cammino ricco di soddisfazioni ma anche di ostacoli, sono giunta alla meta assaporando le emozioni ad ogni passo.

Appendix

11 Mechanical Characterization

11.1 Preliminary Tensile Test

An indicative tensile test has been performed to evaluate the mechanical strength, the Young's modulus or modulus of elasticity (E) and the extension at maximum load of the piezoelectric and non-piezoelectric PCL printed scaffolds, with and without the fibrous layer on the top. The experiment has been conducted at the STEMlab of Loughborough University with the Universal testing system 5944 (Instron) (Figure 11.1).

Figure 11.1 *– The system used to perform the tensile test.*

The deformation speed was set at 2 mm/min. Samples with 13 mm width, 45 mm length and 0.25-0.36 mm thickness were used. A 27 mm gauge length was chosen, while grips were placed at 9 mm from the top and the bottom of the specimen (Figure 11.2).

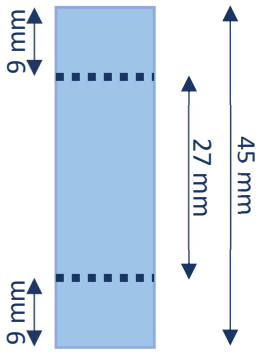

Figure 11.2 *– Specimen sizes used in this experiment.*

Figure 11.3 reports the load-extension curves relative to three samples of piezoelectric scaffolds covered with a fibrous mat containing 250 mg/ml of BTNPs (PCL500-fPCL250).

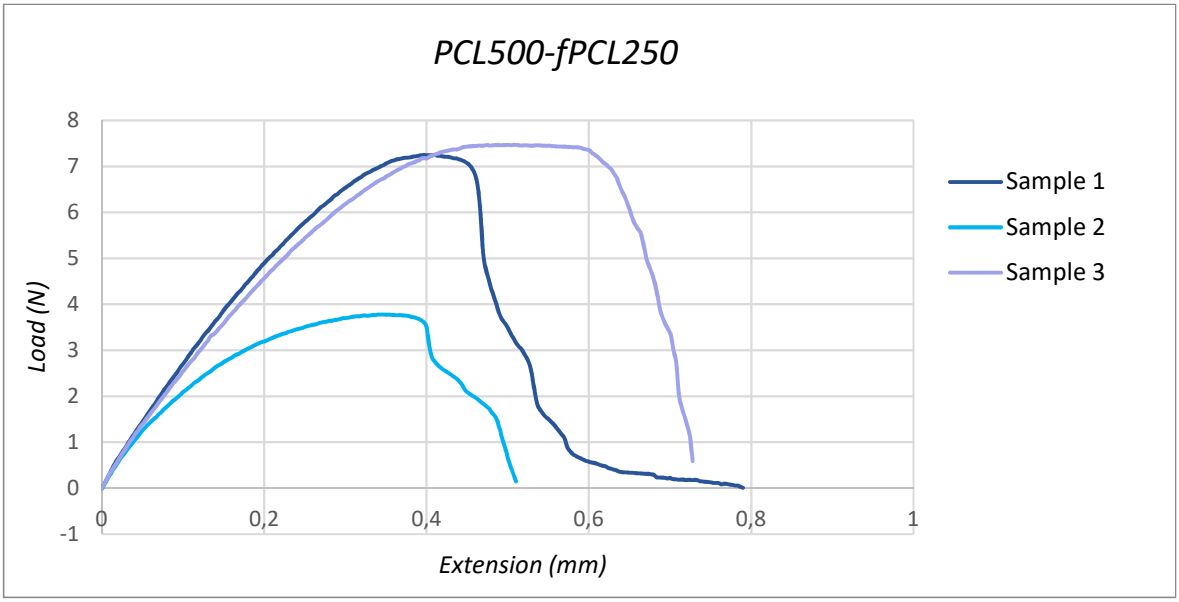

Figure 11.3 - *Load-extension diagrams relative to PCL500-fPCL250 samples.*

The values of extension at maximum load, maximum load, tensile stress at maximum load and Young's modulus that have been measured by the instrument are summarised in Table 11.1.

Table 11.1 *– The main mechanical properties of PCL500-fPCL250 samples, measured by the instrument.*

Samples	Extension at Maximum Load [mm]	Maximum Load [N]	Tensile stress at Maximum Load [MPa]	Modulus (Automatic Young's) [MPa]
1	0.40995	7.24935	2.89742	1096.53353
2	0.34682	3.77706	0.80776	578.07717
3	0.50757	7.46990	1.57719	569.95109

Figure 11.4 shows the load-extension curves relative to three samples of piezoelectric scaffolds without nanofibers (PCL500).

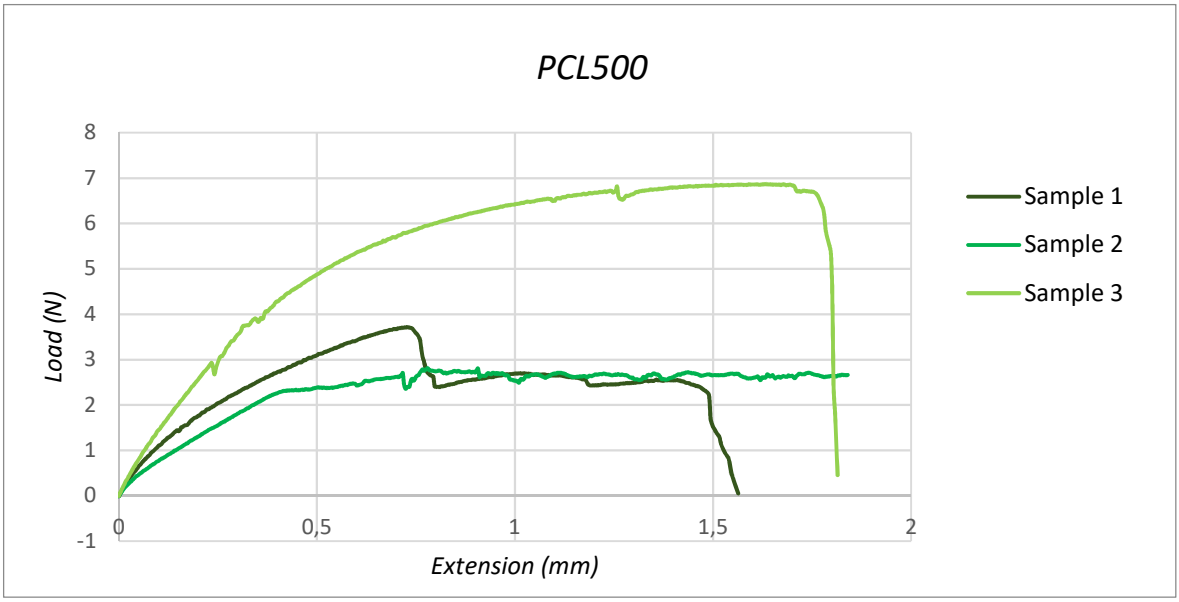

Figure 11.4 - *Load-extension diagrams relative to PCL500 samples.*

During the test of Sample 2, the sample slippage occurs and consequently the measured maximum load does not correspond to the breaking point.

The values of extension at maximum load, maximum load, tensile stress at maximum load and Young's modulus that have been measured by the instrument are summarised in Table 11.2.

Table 11.2 - *The main mechanical properties of PCL500 samples, measured by the instrument.*

Samples	Extension at Maximum Load [mm]	Maximum Load [N]	Tensile stress at Maximum Load [MPa]	Modulus (Automatic Young's) [MPa]
1	0.72696	3.71737	2.04251	664.22186
2	2.50334	2.81369	1.55195	430.34505
3	1.63097	6.86853	3.78849	771.43171

Figure 11.5 shows the load-extension curves relative to one sample of non-piezoelectric scaffolds without nanofibers (PCL0).

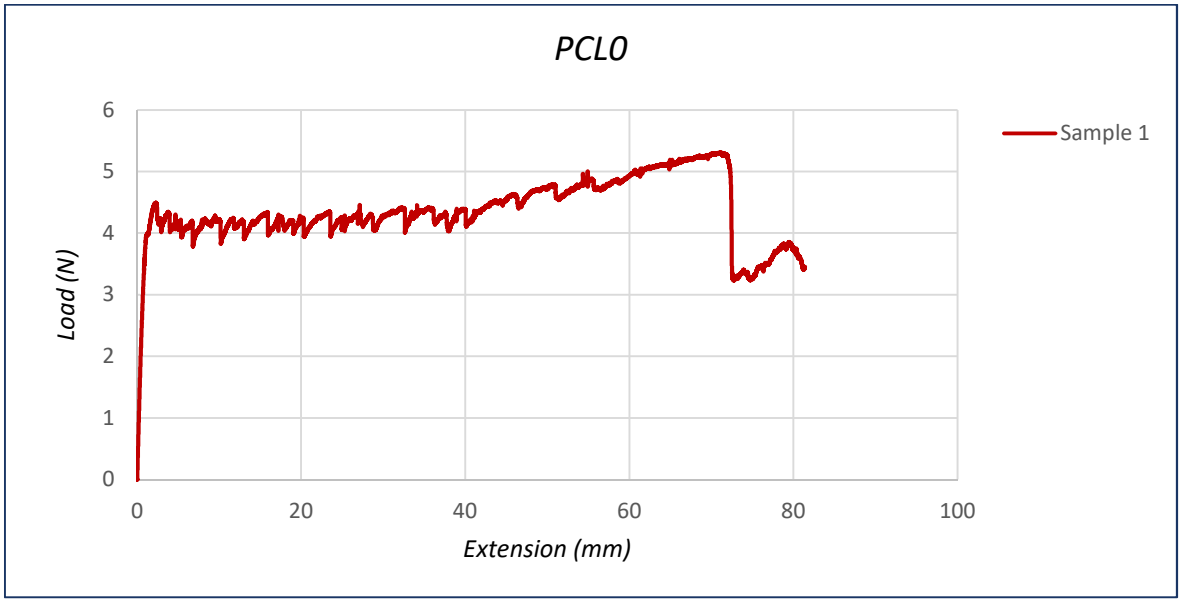

Figure 11.5 - *Load-extension diagrams relative to PCL0 sample.*

This test continued for 40 minutes and the specimen failed to break. The numerous variations of the load correspond to the elongation of each strand in the network of the scaffold.

The values of extension at maximum load, maximum load, tensile stress at maximum load and Young's modulus that have been measured by the instrument are summarised in Table 11.3.

Table 11.3 - *The main mechanical properties of PCL0 sample, measured by the instrument.*

Samples	Extension at Maximum Load [mm]	Maximum Load [N]	Tensile stress at Maximum Load [MPa]	Modulus (Automatic Young's) [MPa]
1	71.16308	5.31261	1.18437	109.86707

A preliminary analysis on the mechanical properties of the tested scaffolds suggests that the barium titanate nanoparticles weaken the structure. Indeed, the extension at maximum load of the non-piezoelectric scaffold is consistently higher than that of the piezoelectric construct. However, the fibers seem to increase the mechanical strength as demonstrated by the values of loads. An interesting aspect that could be majorly studied is the mechanical behaviour of PCL piezoelectric nanofibers that cover the scaffold. As shown in Figure 11.6, the breakage of the scaffold occurs while fibers remain intact.

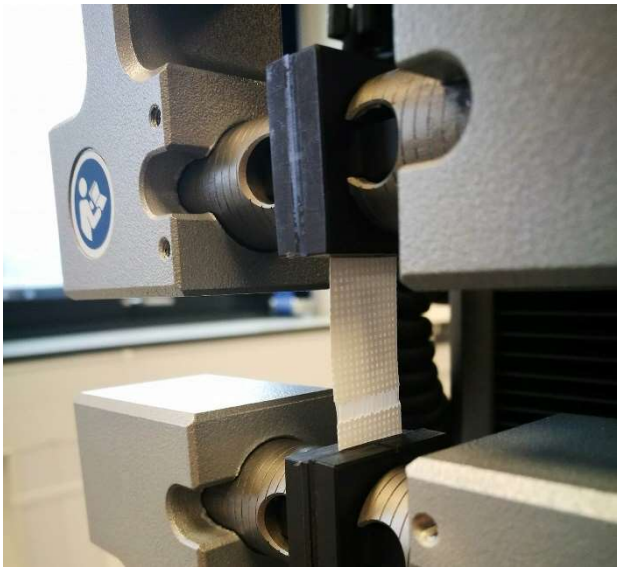

Figure 11.6 *– PCL500-fPCL250 scaffold during the tensile test.*

Although this experiment gives an idea about the mechanical behaviour of the fabricated scaffolds, further analyses are needed to optimise the test. Different specimen sizes could be tested to concentrate the efforts in the central part of the sample, thus avoiding the measure of grips mechanical strength.